Technische Universität München
Lehrstuhl für Elektrische Energiespeichertechnik
Prof. Dr.-Ing. Andreas Jossen

Role of active material composition and microstructure in lithium-ion battery cell safety

Dipl.-Ing. Jan Geder

Vollständiger Abdruck der von der Fakultät für Elektrotechnik und Informationstechnik der Technischen Universität München zur Erlangung des akademischen Grades eines

Doktor-Ingenieurs

genehmigten Dissertation.

Vorsitzender:	Prof. Dr.-Ing. Dr. h. c. Ralph Kennel
Prüfer der Dissertation:	
	1. Prof. Dr.-Ing. Andreas Jossen
	2. Prof. Dr. rer. nat. Jürgen Garche

Die Dissertation wurde am 18.01.2021 bei der Technischen Universität München eingereicht und durch die Fakultät für Elektrotechnik und Informationstechnik am 30.05.2021 angenommen.

Acknowledgements

My involvement in energy storage research would not have been possible without my supervisor, Professor Andreas Jossen, giving me the opportunity to start working on lithium-ion batteries. I am deeply grateful for his mentoring.

I would like to thank my co-supervisor Professor Jürgen Garche for numerous advice, fruitful discussions, and for helping me to think outside the box.

My first steps into work in electrochemical and energy storage laboratory were encouraged, mentored, and supervised by Professor Denis Y.W. Yu. His practical feedback has been immensely helpful for advancement of my research.

I was honoured to work in a great team of colleagues and friends at TUMCREATE Battery Laboratory in Singapore that enabled me through mutual support and team spirit in the group. My growth as a researcher would have been much less enjoyable without my co-workers: Sabine Arnold, Nora Martiny, Kamyar Makinejad, Raghavendra Arunachala, Andreas Hauser, and Lemuel Moraleja.

Research in present dissertation was supported by several students and interns who worked under my supervision. For their valuable contribution to this work, I am thankful to Wenbo Zhang, Ronny Genieser, Simon Pichlmaier, Gerald Jacob, Shishir Jairam, and Kia Min Phua.

Last but not least, I would like to thank all colleagues and staff at TUMCREATE in Singapore and TUM Institute for Electrical Energy Storage Technology in Munich for their support and collaboration.

This work was financially supported by the Singapore National Research Foundation under its Campus for Research Excellence and Technological Enterprise (CREATE) programme.

Abstract

Lithium-ion batteries are promising energy storage systems that enable more efficient utilization of renewable energy sources and facilitate reduction of fossil fuel consumption in transport. Their safety remains up to date one of key challenges for effective and sustainable deployment. Present dissertation addresses differences in electrode active materials' composition and microstructure, particularly their impact on thermal stability and safety of lithium-ion cell. These differences are caused by ageing processes in a cell or by choice of active material with particular properties.

Ageing-induced changes in thermal stability are investigated on both cell and electrode level. These changes are shown to have an ambivalent effect on cell safety as they simultaneously destabilize and passivate segments of the electrodes. Cell tests under thermal and mechanical abuse conditions show significantly changed behaviour in aged cells as a result.

Thermal stability of two cathode types, conventional lithium cobalt oxide and novel over-lithiated oxide, is investigated at different active material surface area. Particle size and resulting surface area play a key role in thermal stability of lithium cobalt oxide cathode. Increased surface area results in thermally less stable cathodes and changes the mechanism of their thermal decomposition reaction. Thermal stability of over-lithiated oxide cathodes is affected by a complex variety of factors besides the surface area, and changes significantly over modest number of cycles.

Factors contributing to electrodes' thermal (in)stability are reflected by parameters pertaining the thermodynamics and kinetics of electrodes' decomposition reaction. These are experimentally determined for each investigated material. Magnitude of each parameter's impact on cell-level thermal behaviour is demonstrated by a simple mathematical model.

Kurzfassung

Die Rolle der Zusammensetzung und Mikrostruktur des Aktivmaterials in der Sicherheit von Lithium-Ionen-Batteriezellen

Lithium-Ionen-Batterien sind vielversprechende Energiespeichersysteme, die eine wirksame Nutzung der erneuerbaren Energiequellen und geringeren Verbrauch der fossilen Brennstoffe im Verkehr ermöglichen. Deren Sicherheit ist bis heute eine der wichtigsten Herausforderungen für die effiziente und nachhaltige Anwendung. Die vorliegende Dissertation befasst sich mit den Unterschieden in Zusammensetzung und Mikrostruktur der Aktivmaterialien in den Elektroden, insbesondere ihre Auswirkung auf die thermische Stabilität und Sicherheit einer Lithium-Ionen-Zelle. Diese Unterschiede werden entweder durch Zellalterungsprozesse verursacht, oder sind die Folge der Auswahl eines Materials mit speziellen Eigenschaften.

Alterungsbedingte Änderungen der thermischen Stabilität werden auf Zellebene sowie auch auf Elektrodenebene untersucht. Diese Änderungen weisen eine ambivalente Auswirkung auf die Zellsicherheit auf, indem sie die Teile der Elektroden gleichzeitig destabilisieren und passivieren. Demzufolge zeigen die Zelltests unter thermischen und mechanischen Missbrauchsbedingungen deutlich verändertes Verhalten der gealterten Zellen.

Thermische Stabilität zweier Kathodenarten, herkömmliches Lithium-Kobalt-Oxid und neuartiges über-lithiierten Oxid, wird bei unterschiedlicher spezifischer Oberfläche des Aktivmaterials untersucht. Partikelgröße und resultierende spezifische Oberfläche spielen eine entscheidende Rolle für die thermische Stabilität der Lithium-Kobalt-Oxid-Kathode. Eine erhöhte spezifische Oberfläche führt zu thermisch labileren Kathoden und ändert den Reaktionsmechanismus ihrer thermischen Zersetzung. Die thermische Stabilität der über-lithiierten Oxid-Kathoden wird beeinflusst durch eine komplexe Anzahl von Faktoren, abgesehen von der spezifischen Oberfläche, und ändert sich schon nach wenigen Zyklen deutlich.

Faktoren, die zur thermischen (In)stabilität der Elektroden beitragen, spiegeln sich in den Parametern der Thermodynamik und Kinetik der Elektrodenzersetzung wieder. Die wurden für jeden untersuchten Aktivmaterial experimentell bestimmt. Der Auswirkungsgrad jedes Parameters auf das thermische Verhalten einer Zelle wird durch ein vereinfachtes mathematisches Modell demonstriert.

Contents

1 Introduction **1**

1.1 Relevance of electrochemical energy storage 2

1.1.1 Lithium-ion batteries 3

1.2 Motivation 5

1.2.1 Structure of the dissertation 5

2 Theoretical Principles **8**

2.1 State of the art lithium-ion technology 8

2.1.1 Safety of Li-ion batteries 10

2.1.2 Overview of commercial electrode materials 12

2.2 Cell lifetime and its impact on safety 14

2.3 Electrode active material particle size and its impact on cell properties 16

2.4 Overlithiated oxides as new cathode materials 17

2.5 Objectives 19

2.6 Hypotheses 20

3 Experimental Methods and Procedures **21**

3.1 Battery cell construction and disassembly 21

3.1.1 Active materials 21

3.1.1.1 As-received active materials 21

3.1.1.2 Sythesis of active materials 22

3.1.1.3 Ball milling of $LiCoO_2$ 23

3.1.1.4 Polyimide coating of LMO-NCM 24

3.1.2 Electrode preparation and battery cell assembly 24

3.1.3 Commercial cells and their cycle ageing 25

3.1.4 Active material sample preparation 26

3.2 Electrochemical characterisation 26

3.2.1 Charging and discharging cells 26

3.2.2 Electrochemical impedance spectroscopy (EIS) 27

3.2.3 Thermodynamic measurements 28

3.3 Thermal analysis 28

3.3.1 Reaction kinetics evaluation by thermal analysis 28

3.3.2 Evolved gases analysis by mass spectrometry (MS) 29

3.4 Accelerating rate calorimetry (ARC) . . . 30
3.4.1 Battery cell calorimetry . . . 31
3.4.2 ARC of electrode-electrolyte system . . . 32
3.5 Abuse testing of battery cells . . . 32
3.6 Material characterisation . . . 33
3.6.1 Spectroscopy and imaging methods . . . 33
3.6.2 Surface area determination . . . 33
3.6.3 Chemical delithiation of cathode active material . . . 34

4 Thermal Behaviour and Safety of Lithium-Ion Battery Cells 35
4.1 Influence of lifetime on cells' thermal and electrical properties . . . 35
4.2 Impact of ageing on safety and thermal stability . . . 40
4.2.1 Thermal stability of new and aged electrodes . . . 40
4.2.1.1 Anode . . . 40
4.2.1.2 Cathode . . . 43
4.2.2 Thermal stability and safety of cells . . . 45
4.2.2.1 Mechanical safety properties . . . 46

5 Microstructure and Thermal Stability of Electrodes 49
5.1 Layered oxide cathode particle size and thermal stability . . . 49
5.1.1 Material overview . . . 49
5.1.2 Thermal stability of $LiCoO_2$ cathodes . . . 50
5.1.3 Role of active material and additives in thermal decomposition . . . 53
5.1.4 Kinetics of $Li_{0.5}CoO_2$ decomposition . . . 57
5.2 Safety aspects of novel over-lithiated oxide (OLO) cathode materials . . . 59
5.2.1 General insight into thermal behaviour of over-lithiated cathode material 59
5.2.1.1 Analysis of decomposition products . . . 63
5.2.1.2 Thermal behaviour of OLO and long-term safety considerations 64
5.2.2 Polyimide coating of OLO as safety improvement strategy . . . 65
5.2.2.1 Comparison of decomposition products . . . 71
5.2.2.2 Kinetics and thermodynamics of decomposition reactions . . . 73
5.2.3 Particle size of OLO cathodes' active material and thermal stability . . 75
5.2.3.1 Properties of synthesized active materials . . . 75
5.2.3.2 Thermal analysis and mass spectrometry of dried cathodes from synthesized materials . . . 76
5.2.3.3 Calorimetry of cathode-electrolyte reaction . . . 81

6 Discussion on Applicability of Microstructural Findings on the Battery Cell Level 83
6.1 Simplified mathematical model for battery cell thermal runaway . . . 83
6.1.1 Model assumptions . . . 83
6.1.2 Model battery cell type, dimensions, and composition . . . 84

6.1.3 Model description . . . 85
6.1.3.1 Energy balance . . . 85
6.1.3.2 Reaction kinetics . . . 86
6.1.3.3 Model parameters and boundary conditions . . . 87
6.1.4 MatLab model and initial results . . . 88
6.2 Sensitivity analysis of thermodynamical and kinetic parameters . . . 89
6.2.1 State of no return as criterion . . . 89
6.2.2 Variation of parameters . . . 90
6.2.2.1 Anode reaction . . . 90
6.2.2.2 Entire model . . . 92

7 Summary **96**
7.1 Conclusions . . . 96
7.1.1 Ageing and safety . . . 96
7.1.2 Surface area and thermal stability of $LiCoO_2$ . . . 97
7.1.3 Overlithiated oxide materials and their safety . . . 97
7.1.4 Relevance of experimentally determined parameters . . . 98
7.1.5 Validation of hypotheses set in Section 2.6 . . . 98
7.2 Outlook . . . 100
7.2.1 Proposed work and improvements on active material investigations . . . 100
7.2.2 Towards better understanding of cell safety . . . 101

Acronyms, Abbreviations, Subscripts **102**

Index of Symbols **104**

List of Figures **106**

List of Tables **110**

Bibliography **111**

Appendices **122**
A.1 SEM images of electrodes from new and aged 18650 cells . . . 122
A.1.1 Anode . . . 122
A.1.2 Cathode . . . 123
A.2 XRD of decomposed NCM cathodes from new and aged 18650 cells . . . 124
A.3 MatLab model . . . 125
A.3.1 Main script . . . 125
A.3.2 Differential functions . . . 127

1 Introduction

Commodities, energy, and knowledge are the crucial categories fuelling economic and social development of the human civilization. They are interconnected and interdependent. In order to ensure abundant and sustainable availability of these categories, storage is as important as generation. Energy itself differs from the tangible commodities by several distinguishing physical properties, which makes its storage particularly complex. Also, many types of energy usually cannot be stored in the same form as it is intended to be used. Most conveniently, it is stored as chemical energy [1]. Currently, industries and consumers are heavily relying on the abundant amounts of chemical energy that had been stored in the earth's crust in form of fossil fuels. Energy from fossil fuels amounts to 81.2% of world's total annual energy consumption, it generates 67% of global electricity output, and powers virtually entire transport [2]. The reserves of coal, petroleum, and natural gas are nevertheless limited. In addition, exploitation, processing, and combustion of fossil fuels cause significant damage to the environment. This has caused ongoing efforts to minimize the usage of fossil fuels. Alternatives that could replace the fossil fuels are therefore sought for generation of electrical energy on one hand and propulsion of land vehicles on the other. Renewable sources of energy, such as sunlight, wind, water, biomass, and geothermal energy [3], are generally regarded as alternatives to fossil fuels in the long run. Utilization of these energy sources is currently hindered by several obstacles, among them low efficiencies, high capital costs, and unstable supply [4].

One of mentioned obstacles stands out by its insensitivity towards technological development: Supply stability of the renewable energy sources. Their occurrence and availability is subject to natural phenomena such as geography, climate, weather, and tidal cycles [5]. These are uncontrollable by human technical means and thus the supply stability is subject to fluctuations, which are only partially predictable. For the supply of electrical energy from renewable sources to be stable, storage of the generated energy is necessary. Apart from the case of biomass, which is in itself tangible material with stored chemical energy, the energy harnessed from renewable sources has to be stored during the periods of high supply and low demand. Stored energy has to be promptly convertible to the usable form of energy, e.g. mechanical, electrical, or thermal energy, in order to be utilized in the periods of high demand and low supply.

Energy can be stored in various manners. These include, but are not limited to following [6]:

- Chemical energy stored in tangible matter
- Potential energy convertible to mechanical energy, e.g. storage by pumping water to reservoirs at higher altitude
- Pressurized fluid energy convertible to mechanical energy, e.g. storage of compressed air in containers
- Specific cases of thermal energy storage [7]

Applicability of each storage concept highly depends on the dimension of the system, input/output requirements, and storage time [6].

1.1 Relevance of electrochemical energy storage

Electricity is the most common way of transporting and utilizing energy for general and retail use. Advantages of electricity include versatility of its utilization due to facile conversion to commonly used forms of energy (e.g. mechanical, thermal, light), and untroubled, cost-efficient transport over long distances in connection with ubiquity of electrical infrastructure worldwide. In addition, renewable electric energy generated from solar radiation and wind can be conveniently integrated to supply to existing power systems. It is therefore desirable to store energy in a way where it can be easily converted into electrical energy. Electrochemical energy storage systems possess the advantage of direct conversion between storable chemical energy and employable electric energy. Therefore, they do not require an intermediate conversion step involving thermal and/or mechanical energy. Such conversion avoids practical and theoretical limitations of Carnot cycle and thus yields higher efficiency. This carries further advantages in certain circumstances, since it also reduces the physical size and capital cost of the system.

Electrochemical energy storage is a special case of storing chemical energy in form of matter and is directly convertible to electrical energy. Therefor, electrochemical reactions are the underlying chemical transformations. An electrochemical reaction is always a redox reaction, meaning that certain involved atoms have their oxidation state changed. This is accompanied by the exchange of electrons which is either caused by externally supplied electrical current (power consumption by charging) or by generating the electric current (power is supplied by discharging). The former is generally related to endothermal and endergonic redox reactions and the latter to exothermal and exergonic reactions. If a certain electrochemical reaction is reversible, it can be utilized for storing the electrical energy in form of electrochemical energy. In such case, external electric current causes an endothermal, endergonic chemical reaction forming material with higher chemical potential. The exothermal and exergonic reaction in the opposite direction transforms the stored electrochemical energy to electricity.

Generally, electrochemical energy storage and conversion systems are divided to batteries, fuel cells and electrolysers, and electrochemical capacitors [8]. The latter, also known as supercapacitors, are storing energy at electrode/electrolyte interfaces. This means that in a supercapacitor, electrical energy is stored directly and is not converted in storable chemical energy via redox reactions, which is the case for fuel cells / electrolysers and batteries. Fuel cell is an electrochemical cell which can continuously convert the chemical energy of fuel and oxidant to electrical energy by a a process involving an essentially invariant electrode-electrolyte system [9]. Thus it is an open system which transforms the chemical energy of the externally fed fuel to electricity, whereby the involved electrodes and electrolyte do not react during the transformation. On the other hand, battery cell is a device that converts the chemical energy contained in its active materials directly into electric energy [10]. With a notable exception of metal-air batteries, it is typically a closed system, and its electrodes and/or electrolytes are active materials that participate in the underlying chemical reaction. They are the energy carriers whose chemical energy is converted to electrical energy.

Batteries can be primary (disposable) or secondary (rechargeable). The latter are characterized by reversibility of the underlying electrochemical reaction and can be repeatedly electrically recharged. Only the rechargeable batteries are relevant candidates for large-scale energy storage systems and power sources for vehicles. Various types of batteries are distinguished by their electrochemistry. Their technical suitability is judged by criteria of energy/power density, cyclic efficiency, lifetime, costs, safety, costs, and others. These properties are interconnected and often opposed to each other, causing the design of battery cell to become a trade-off between them.

1.1.1 Lithium-ion batteries

Lithium-ion batteries are a recently commercialized type of batteries. First scientific foundations were laid in 1980s and in 1990s the technology was commercialized by Sony Corporation. Advantages of Li-ion batteries include higher energy density and voltage, improved lifetime due to reduced capacity fade and negligible self-discharge, and absence of the so-called memory effect [11]. This has caused the market share of the Li-ion among other batteries to increase rapidly since the commercialization. Main application field of Li-ion batteries was portable electronics. They are however gaining importance as power sources for electric vehicles and as storage systems for electricity generated from renewables.

With all improvements up to date, Li-ion battery technology still possesses several shortcomings that need to be addressed at various levels of research, design, and engineering. Main challenges of Li-ion battery technology in context of powering land transport and energy storage for renewables are listed below and discussed in more detail in Chapter 2.

- Energy/power density: The ability to reversibly store up to 250 Wh of energy per kilogram or 500 kWh m^{-3} [8, 11] at the cell level makes Li-ion batteries superior to

other commercial battery technologies with regards to energy density. However, they can hardly compete with energy densities of fossil fuels, e.g. 12.5 kWh kg^{-1}/9.2 MWh m^{-3} for octane (gasoline) [12, p. 2-199]. Another concern is the rate at which energy can be stored in such system or the rate at which the system can provide energy. This is commonly referred to as power density.

- Costs: Despite rapid decline in batteries' prices through the recent years [13], the battery pack still represents a significant share in the total price of electric vehicles.
- Lifetime: Ageing of lithium-ion cells results in performance decrease due to capacity loss and increase of internal resistance [14].
- Safety: A typical Li-ion battery is a thermodynamically unstable system. It contains flammable electrolyte and electrodes whose potential may be outside the stability window of the electrolyte. This is in particular true for graphite anodes. Metastability of such electrochemical system is ensured by formation of layers on the surface of electrodes during the first charge. Nevertheless, flammability of the electrolyte poses permanent risk for battery safety.

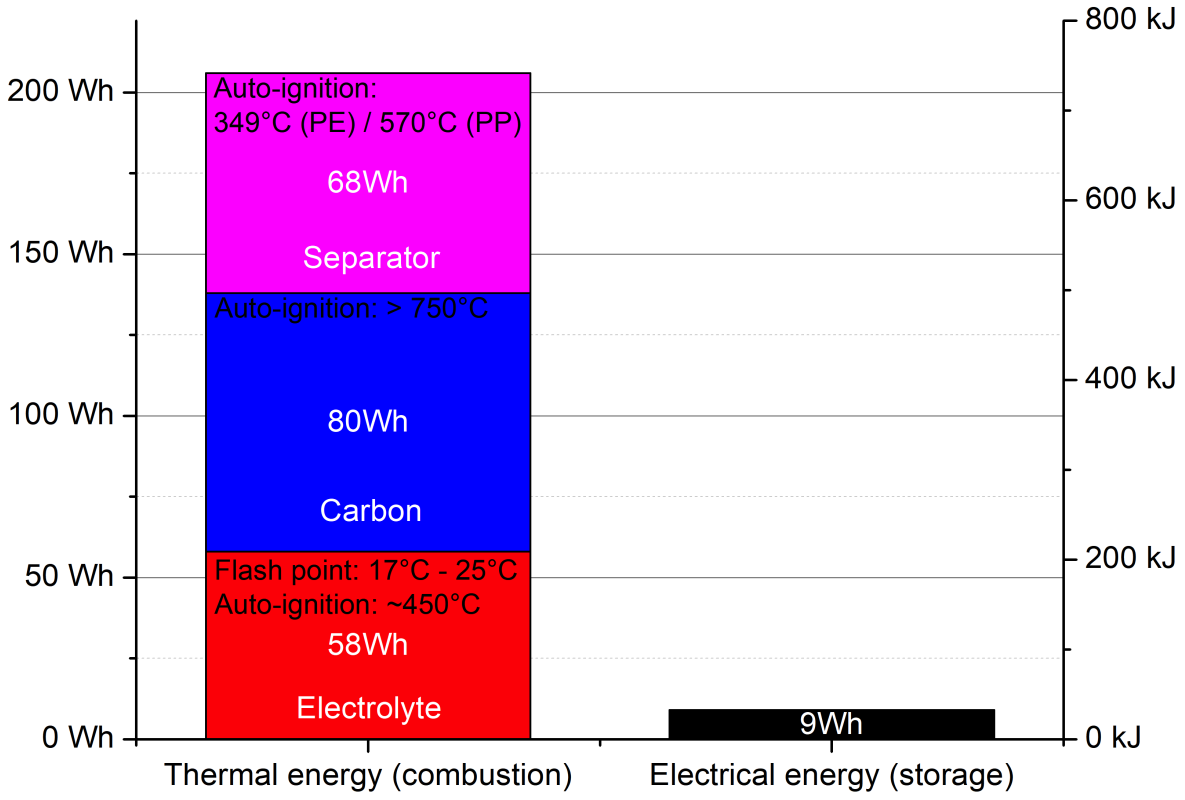

Figure 1.1: Comparison of energy storage capacity and combustion energy of a 2.5 Ah 18650 Li-ion cell. Estimation based on [15].

Figure 1.1 compares combustion energies of some cell components. Estimation is based on a cylindrical 18650-type cell with a nominal capacity of 2.5 Ah and nominal voltage of 3.6 V. Electrolyte in lithium-ion batteries poses an inherent risk of fire and explosion due to its high flammability and low flash point. Its combustion enthalpy alone exceeds the cell's energy storage capacity more than six times. Even without igniting, electrolyte can react exothermally with negative and positive electrodes under certain abusive conditions. Heat generated by these reactions may itself exceed the energy storage capacity of the battery cell [16]. Carbon anode and polyolefin separator are far less dangerous than electrolyte, however they too may ignite at elevated temperatures caused by an ongoing thermal runaway. The above mentioned metastability of the whole electrochemical system is sensitive to temperature, pressure, and electrical conditions within the cell, and can thus act as a trigger of uncontrollable thermal runaway in the cell.

1.2 Motivation

Besides the high costs hindering fast implementation, safety is the one of the main issues in the present-day Li-ion battery technology. Countless occurrences of Li-ion battery fire and explosions [17] are hindering the implementation of this technology for larger-scale energy storage, such as battery packs for electric vehicles. There are ongoing efforts to improve safety of Li-ion cells and battery systems without significantly compromising energy and power density. On the other hand, certain changes to Li-ion cell with purpose of enhancing energy and power performance may affect cell safety.

As mentioned previously and further elaborated in subsection 2.1.1, Li-ion battery cell is an inherently unstable system.

This work aims to deepen the understanding of safety-related phenomena in lithium-ion energy storage technology. Safety is influenced by various factors at several levels of scale: from structural stability of chemicals used as components of battery cells, to the reliability on the system level. Research in the present dissertation bridges the thermal stability issues on the battery cell level with microstructure and composition of electrode active materials.

Working concept of the research is shown in Figure 1.2. Structure is further described in the following section 1.2.1.

1.2.1 Structure of the dissertation

Essential electrochemical and technical foundations of lithium-ion batteries are described in Chapter 2, together with an overview of the state-of-the-art and elaboration of the main challenges related to safety of Li-ion batteries. The underlying problems are explained in terms of their practical implication on the battery cells and are subsequently related to physical and

chemical properties of materials built into battery cells. Based on this knowledge, research objectives are defined and hypotheses are set to provide an overall guidance for the present research work.

Chapter 3 is dealing with the experimental and mathematical methods used in the research. For each of the methods, a brief illustration of functioning principles is given along with the explanation of relevance for the particular purpose in the research. Experimental settings and conditions, as well as relevant evaluation criteria, are described in detail.

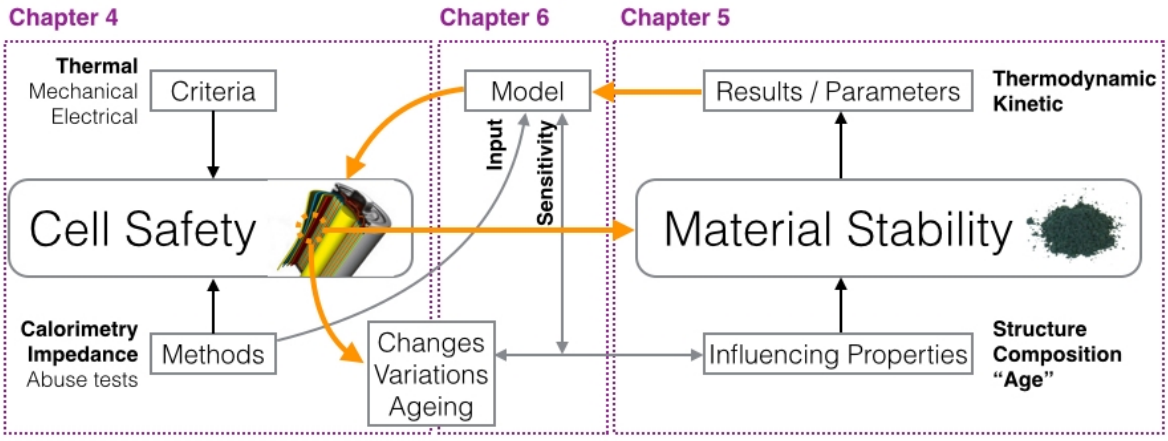

Figure 1.2: Scheme of the working concept for the research in the present thesis

Results are presented and discussed in three separate and interdependent Chapters. Chapter 4 is dealing with thermal behaviour of Li-ion cells. Processes leading to thermal runaway are elaborated in terms of energy balances and reactions. Impact of ageing phenomena is taken into account, whereby the changes in thermal behaviour are observed as consequences of ageing-induced structural changes in a cell. Finally, the implemented calorimetric methods are evaluated for their suitability for investigating Li-ion cells. Shortcomings of the conventional ARC are defined and improvements are proposed, both for experimental set-ups as well as for result interpretation. Chapter 5 brings the focus to the material scale. Influence of the particle size / surface area of the active material on the thermal stability thereof is investigated for a commonly used cathode active material lithium cobalt oxide ($LiCoO_2$). Following this, the safety-related considerations for implementation of a next-generation lithium-rich manganese-based cathode active material are addressed on the compositional and microstructural level. Exact elemental composition is taken into account together with the particle size and crystal structure considerations. Polyimide coating of active material surface is considered for mitigation of both ageing and safety issues. Finally, Chapter 6 connects the material related findings on electrode level with their actual application in battery cells. This is done with strong focus on safety behaviour of the cells. A simple mathematical model for cell thermal runaway is implemented to elaborate the contribution of individual material-influenced stability phenomena to thermal behaviour of a customary cylindrical battery cell.

Chapter 7 summarizes the research done and points out the important conclusions. Each of the initial hypotheses is re-evaluated versus the results obtained. Later, initial objectives are assessed to elucidate the potential applicability of the present research for the improvements of state-of-the-art Li-ion technology. In addition, further research is proposed that should lead to compositional and structural improvement of active materials from the viewpoint of safety. Further improvements for the characterization and measurement methodology, as well as for approaches to evaluation of results, are also suggested in the Outlook section.

2 Theoretical Principles

2.1 State of the art lithium-ion technology

Lithium-ion (Li-ion) electrochemical systems are based on utilising the smallest cation, lithium ion, as the charge carrier between positive and negative electrode. Contrary to primary and secondary lithium batteries, Li-ion battery does not contain lithium metal under normal operating conditions. This greatly reduces the risk of lithium dendrite formation causing internal short circuit. A wide range of active materials are available to accommodate lithium ion in either electrodes. Contemporary Li-ion batteries were commercialised by SONY in early 1990s employing hard carbon and layered lithium cobalt oxide ($LiCoO_2$, LCO) as anode and cathode, respectively. Up to date, most lithium-ion batteries sold worldwide still contain carbon-based anode and lithium transition metal oxide with layered structure as cathode.

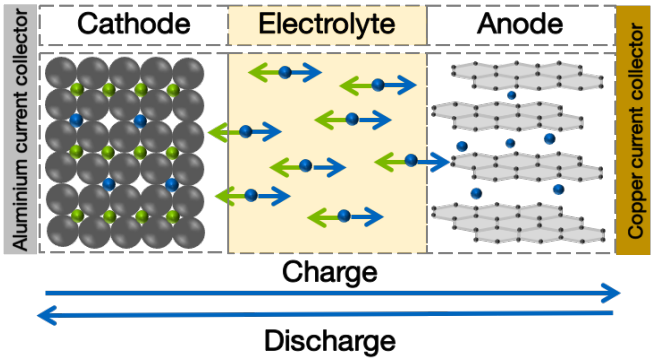

Figure 2.1: Microscopical representation of a segment in a typical Li-ion cell

Scheme of the Li-ion cells' functional principle is shown on Figure 2.1. Cathode and anode, containing respective active materials and additives such as conductive carbon and polymer binder, are coated on aluminium and copper foil. Electrodes are separated by polyolefine separator, and the whole stack is soaked in electrolyte. The latter is typically lithium hexafluorophosphate $LiPF_6$ dissolved in organic carbonates' blend, which may include dimethyl carbonate (DMC), diethyl carbonate (DEC), ethylene carbonate (EC) and other components. Alternative electrolyte conductive salts, such as lithium bis(oxalato)borate $LiBC_4O_8$ (LiBOB) are being researched and tested as they are promising improved performance at elevated temperatures and lower toxicity due to absence of fluorine [18].

In such configuration, cathode is the source of lithium ions, and the cell is assembled in a fully discharged state. During charge, lithium ions are de-intercalated from layered oxide structure of cathode material, as described by equation (2.1). This is compensated by oxidation of transition metal ion [M] in the same structure.

$$\mathrm{Li[M]O_2} \rightleftharpoons \mathrm{Li_{1-x}[M]O_2} + x\mathrm{Li^+} + xe^- \tag{2.1}$$

Lithium ion is inserted between the carbon layers of graphite anode, as shown by equation (2.2)

$$\mathrm{C_6} + x\mathrm{Li^+} + xe^- \rightleftharpoons \mathrm{C_6Li_x} \tag{2.2}$$

Large difference between the electrochemical potentials of above listed reactions requires use of non-aqueous electrolyte. Reaction (2.1) has a potential of up to 4.2 V versus $\mathrm{Li|Li^+}$ redox couple at high values of x (charged state). At the same time, potential of reaction (2.2) drops close to zero vs. $\mathrm{Li|Li^+}$ at high values of x. This results in cell voltage above 4 V at fully charged state and has two important consequences on cell design and operation:

1. At low potentials of negative electrode, an inherent risk of lithium metal plating is present. Lithium deposition on carbon particles' surface occurs in form of dendrites, which may penetrate the separator and cause short circuit [19]. Therefore, anode has to be over-dimensioned versus cathode in terms of lithium storage capacity and it has to overlap cathode physically by a certain margin [20, 21].

2. An electrolyte with a wide electrochemical stability window is required. Usage of aqueous electrolytes is thus excluded, as water would decompose to oxygen and hydrogen at given voltage. This is the reason for introduction of above mentioned organic carbonate electrolytes.

Implementation of non-aqueous electrolyte makes higher cell voltage viable. However, lithium - transition metal cathode and carbon-based anode are not entirely within electrolyte's stability window; cathode operates at its upper limit, while anode operates outside of it [22]. Low negative electrode potential poses certain challenges to implemented organic electrolytes despite their improved electrochemical stability. Reason for this is reactivity of electrolyte solvents, as well as conducting salt anions, with Li-intercalated carbon [23]. The state of so-called kinetic stability is achieved on anode surface through formation of the solid-electrolyte interphase (SEI). During the electrolyte filling process and the first charge of newly assembled Li-ion cell, lithium ions and organic carbonate solvent molecules react on the surface of carbon anode to form a surface film of mainly organic, but also inorganic lithium compounds. SEI thus prevents further reduction of electrolyte on anode surface while conducting $\mathrm{Li^+}$ ions and plays therefore a critical role in ensuring stability and safety of Li-ion cells.

2.1.1 Safety of Li-ion batteries

The above stated consequences of Li-ion electrochemical systems' high cell-level potential affect first and foremost the stability and safety of Li-ion batteries. Energy potential of electrolyte and other components' flammability has been discussed in section 1.1.1. However, flammable electrolyte enclosed in the cell does not tend to ignite by itself. According to commonly accepted fire safety conventions, there are three preconditions for occurrence of fire and/or explosion [24]:

- Fuel
- Oxidant
- Trigger

These components form the so-called "fire triangle". Fuel, which is in given case the flammable electrolyte, reacts exothermally with an oxidant. This has to be triggered by delivering sufficient energy to fuel-oxidant interface in order to start the reaction.

Oxygen present in the atmosphere may act as the oxidant. Such reaction between electrolyte and atmospheric oxygen would require rupturing of cell casing. On the other hand, gaseous O_2 may be generated inside the cells from other components, specifically the cathode. Above mentioned $LiCoO_2$ may thermally decompose at charged state according to following equation [25, 26]:

$$\mathrm{Li_{1-x}CoO_2} \rightarrow (1-x)\mathrm{LiCoO_2} + \frac{x}{3}\mathrm{Co_3O_4} + \frac{x}{3}\mathrm{O_2} \tag{2.3}$$

This reaction occurs at temperature above 200°C [26] and introduces pure gaseous oxygen at elevated pressure and temperature to surrounding electrolyte. Oxygen-yielding thermal decomposition is common to all lithium - transition metal cathode materials with layered crystal structure (see section 2.1.2).

During operation, storage, and handling of Li-ion cells, several potential triggers may occur [27, p. 10]. In general, it is necessary for a cell to reach certain elevated temperature in order to trigger the chain of phenomena, commonly known as thermal runaway. Temperature increase in a cell can be related to following causes:

- External heat source
- Electric current (entropic heat generation and/or Joule heating)
- Short circuit (internal or external)
- Unwanted reactions caused by:

  Errors in design or manufacturing

  Operation outside acceptable range of temperature and/or voltage

Various reactions accompanying thermal runaway occur at different temperatures. These are also dependent on materials' structure and composition. Thermally most sensitive component in a Li-ion cell is the solid-electrolyte interphase at carbon-based anode.

In a typical Li-ion cell, following sequence of exothermal reactions occurs as cell temperature increases [28]:

1. SEI decomposition: Molecules of SEI begin to decompose at temperatures below 100°C, given the sufficient exposure time [29]. The reaction reaches its peak at around 100°C [30].
2. Reactions of intercalated Li with electrolyte: Following the removal of protective SEI layer, electrolyte reacts with lithium. This occurs at temperatures near 120°C [31]. These reactions may lead to formation of flammable gases.
3. Electrolyte decomposition: Carbonate-based electrolyte solutions decompose above 180°C [32]. This processes can be catalysed by certain transition metal ions present in the cathode [33].
4. Cathode active material decomposition: As described by Equation (2.3) above, charged lithium - transition metal active materials decompose at elevated temperatures above 200°C. The reaction yield gaseous oxygen, which may exothermally react with the remaining electrolyte and the negative electrode material, e.g. graphite [33].

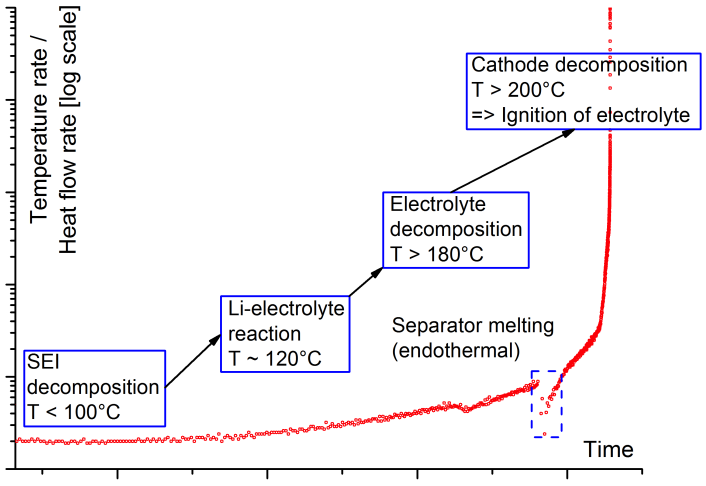

Figure 2.2: Typical thermal runaway profile of a lithium-ion cell with carbon-based anode and layered lithium - transition metal cathode.

Course of thermal runaway is graphically presented in Figure 2.2. An increasing trend of temperature rate and heat flow is observed as above listed reactions follow each other. At certain point along this course, heating rate exceeds the dissipation of generated heat away from the cell (either by convection or active cooling measures). This is regarded as point of no return, and leads to fire or explosion of the cell.

Some reactions occuring in a cell at elevated temperatures are nevertheless endothermal. An example of heat-consuming reaction is melting of polyolefine separators, represented in Figure 2.2 as a dip in heating rate. On one hand, melting of polyethylene (above 120°C) initially prevents flow of ions between electrodes. However, during complete meltdown of separator at higher temperatures (melting of polypropylene above 160°C), internal short circuit is unavoidable and further increases the heating rate of cell.

2.1.2 Overview of commercial electrode materials

The very first commercial Li-ion cells from early 1990s had energy density of 200 $Wh\ l^{-1}$ / 80 $Wh\ kg^{-1}$. Until present day, several new active materials have been proposed and implemented as electrodes, leading in combination with improved electrode and cell design to cell-level energy densities above 600 $Wh\ l^{-1}$. Targeted development of specific cell types for various purposes is possible by combining different active materials, electrolytes, additives, and by adjusting other cell design factors.

Anodes in contemporary Li-ion cells are overwhelmingly carbon-based, consisting of either graphite, hard carbon, or mesocarbon microbeads (MCMB). Carbon materials are characterized by their satisfactory specific capacity of approximately 350 $mAh\ g^{-1}$ and relatively low price. Nevertheless, they exhibit consequential drawbacks affecting the performance and safety of Li-ion cells:

- At high SOC, higher currents, and/or at low temperatures, lithium ions can be reduced at negative electrode surface. They are deposited as metalic lithium in form of sharp dendrites that cause internal short circuit in a cell [19]. Application of Li-ion cells, particularly their charging, is therefore critically limited at temperatures below 0°C.
- Low electrochemical potential of C_6Li_xanode is advantageous for cell-level energy density, however it presents two important challenges:

  Low-priced and lightweight metals such as aluminium cannot be utilized as current collectors at low potential, since they would oxidize. Use of heavy and expensive copper is therefore required.

  Low potential poses a danger of electrolyte decomposition and formation of flammable gasses. This is compensated by boundary layers (SEI) described in Section 2.1.1

Currently, the only commercially viable alternative to carbon-based anodes is lithium titanate (LTO, $Li_4Ti_5O_{12}$). LTO with its spinel structure is characterized by its plateau voltage of 1.56 V [34]. This facilitates implementation of light-weight and cheaper aluminium as current collector. Furthermore, higher potential enables stable operation within the electrolytes' stability window. Therefore, no SEI formation or lithium plating occur on anode surface. Cells employing LTO anodes exhibit high power density due to superior mobility of Li^+ ions in spinel structure and applicability at temperatures as low as -30°C [35]. On the other

hand, increased anode potential leads to lower cell voltage, and specific capacity of LTO (175 $mAh\ g^{-1}$) corresponds to roughly half of the graphite's capacity [36]. This results in a significant decrease of cell-level energy density.

New anode candidates are investigated to overcome disadvantages of the aforementioned materials, and enable development of cells with higher energy density. Two most notable examples are briefly described below:

- Silicon anode can theoretically yield specific capacity higher than 4000 $mAh\ g^{-1}$. Its practical application is limited by extreme volume changes during lithium ion intercalation, leading to fast capacity fade [37]. Various approaches of mitigating this phenomenon are underway, mainly involving silicon-carbon composite anodes [38].
- Lithium metal anode was employed in the first rechargeable lithium batteries, developed in 1970s, with transition metal dichalcogenides as cathodes [39]. Safety issues related to metallic lithium prevented greater deployment of such systems [27]. Due to its high energy density, lithium metal is currently considered as likely next-generation anode in solid-state lithium batteries [40, p. 79].

Cathodes in commercially available Li-ion cells are classified by crystal structure of active materials [39]. Most common groups of cathode active materials are:

- Lithium transition metal oxides, layered structure
- Lithium transition metal oxides, spinel structure
- Lithium transition metal phosphates, olivine structure

Layered oxides have emerged as modifications and/or improvements of originally implemented LCO. LCO has remained the cathode material of choice for consumer electronics batteries due to its good balance between capacity (140 $mAh\ g^{-1}$), safety and ease of processing [41]. Cobalt in $LiCoO_2$ can be partially substituted by other transition metals in order to improve certain properties [42]. Typically, nickel and aluminium or nickel and manganese are substituents of choice, leading to two types of cathode materials:

- Lithium nickel cobalt aluminium oxide (NCA, $LiNi_{0.8}Co_{0.15}Al_{0.05}O_2$): Partial substitution of Co through Ni increases capacity ($\sim$ 200 $mAh\ g^{-1}$) and reduces price, but slightly decreases power density. Addition of non-transition metal aluminium (1.4% by weight) serves the purpose of structure stabilisation [43].
- Lithium nickel cobalt manganese oxide (NCM, $LiNi_xCo_yMn_{1-x-y}O_2$): Combination of three transition metals (Ni, Co, Mn) allows slight adaptations of active material properties by adjusting the ratios of transition metals (x,y). Most commonly, stoichiometric NCM (x,$y = \frac{1}{3}$) [44] is used in commercial cells. This material is characterized by 0.1 V lower potential, which slightly decreases energy density compared to LCO. Thermal stability is improved due to higher onset temperature of decomposition reaction. In order

to improve capacity and reduce raw material cost of NCM, manufacturers are aiming to increase nickel content [45]. Materials with transition metal ratios Ni:Co:Mn of 5:3:2, 6:2:2, and 8:1:1 [46] have been proposed and implemented to that end. The increase of Ni content however leads to reduced thermal stability [47].

Spinel lithium manganese oxide (LMO-s, $LiMn_2O_4$) is a cathode material of choice for high power applications, such as power tools. Due to its spinel structure, which enables diffusion of Li^+ ions in three dimensions, it can withstand higher currents and thus contribute to cells' power density [48]. Disadvantages of LMO-s are lower capacity ($\sim 120\ mAh\ g^{-1}$) and poor lifetime.

Olivine lithium iron phosphate (LFP, $LiFePO_4$) is regarded as safe alternative to oxide-based materials. During its thermal decomposition reaction or overcharge, no gaseous oxygen is formed [49]. Its low potential of 3.3 V reduces the energy density of LFP-based cells, but also prevents electrolyte decomposition. Due to comparatively lower cost of raw material, LFP is mainly a technology of choice for stationary, non-portable energy storage, though it is also finding its application in lower-cost electric vehicles.

2.2 Cell lifetime and its impact on safety

Cell ageing is caused by numerous processes that are highly interdependent, making these phenomena extremely difficult to study experimentally [50]. Ageing mechanisms are different at anode and cathode, including the electrolyte interaction with either electrodes. Practical consequences of ageing are capacity loss and increase in cell impedance, which leads to power fade. There are two causes of cell ageing [14]:

- Calendar ageing corresponds to degradation during storage, with no current flow through the battery cell. It is strongly influenced by ambient temperature and state of charge (SOC) of the stored cell [51].
- Cycle ageing is the result of active material degradation coming from side reactions and phase transformations during lithium insertion [51]. It is influenced by temperature and cycling parameters, such as current, voltage, and depth of discharge (DOD).

Most significant ageing phenomena are elaborately listed and described in literature [14, 50, 51]. Figure 2.3 shows where in the cell do crucial ageing processes take place. They include, but are not limited to, following:

- Loss of cycleable Li^+ ions, typically caused by:

  Growth of boundary layers at interfaces (e.g. SEI)

  Lithium metal plating

- Active material particle cracking

- Phase changes in active material and structural disordering
- Contact loss of active material due to binder decomposition
- Corrosion of current collectors
- Solvent reaction causing gas evolution

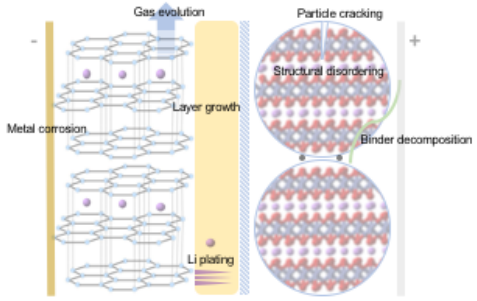

Figure 2.3: Schematic representation of ageing phenomena in a lithium-ion cell. Components not to scale

Impact of general ageing process on thermal stability and safety is assumed to be ambivalent. Individual processes listed above may either worsen or increase thermal stability. They may also have no significant effect. As a final consequence, decrease in energy storage capacity may reduce certain risks, e.g. in case of short circuits, as there is less energy available to be transformed into heat. This does not warrant that causes leading to capacity decline will not have other detrimental influences on thermal stability. For example, lithium metal plating reduces cell capacity while presenting inherent risk of internal short circuit and exothermal reactions. On the other hand, increase of cell impedance results in higher heat generation rate during operation, which increases the risk of overheating leading to thermal runaway.

Table 2.1 classifies various ageing phenomena based on their possible impact on thermal stability and safety. The contents of this table shall be understood as an effort to hypothesize general impact of individual phenomena on stability of a cell.

Safety of aged cells in comparison to fresh ones is dependent on ageing conditions. Particularly in case of cycle ageing, lower ambient temperatures have been proven detrimental for safety as they cause lithium metal deposition on anode surface [52, 53, 54]. Wu et al. [55] compared thermal stability of electrodes from fresh and cycle aged LCO/graphite cells by means of DSC. While the onset temperature of decomposition does not change as consequence of ageing, both anode and cathode exhibit significantly higher enthalpy of decomposition reaction. This means increased heat release and thus an accelerated thermal runaway.

On the other hand, in case of calendar ageing, especially at elevated temperature, findings cited in literature are rather ambiguous. Roth and Doughty [56] compared thermal stability of fresh and temperature-aged cells, and their electrodes (NCA and carbon). They have demonstrated higher onset temperature of thermal runaway for aged cells, particularly for cells aged at higher temperature. This change in behaviour is related to improved stability of

Table 2.1: Hypothetical evaluation of ageing effects with regards to their presumed impact on thermal stability

Destabilizing effects	**Passivating effects**
Impedance increase: Higher heat generation rate	**Capacity decline**: Less energy available for sudden release
Layer formation and growth: Layers such as SEI are thermally unstable, may decompose at temperature as low as 80°C	**Layer formation and growth**: Reduced occurence of side reactions
Gas evolution: Increased pressure affects mechanical stability of cell; gasses are often flammable	**Structural disordering**: Change in crystal structure may yield a thermally more stable phase, e.g. when layered structure is transformed to spinel
Li plating: Cause of internal short circuit [52]	**Loss of cycleable Li^+**: Similar to capacity decline; anode will be more stable with less Li^+ intercalated

aged anodes, while the difference in stability between fresh and aged cathodes is less significant. In contrast to this, Röder et al. [57] reported reduced thermal stability (in terms of lower onset temperature) for aged cells (LMO-s/NCM and carbon). The difference is shown to be caused by changes on anode side, presumably due to ageing-induced growth of SEI layer. It is notable to mention that cells in above cited studies do not employ same type of carbon as anode. Therefore, it is reasonable to assume that impact of ageing on safety is not independent from type of active material.

2.3 Electrode active material particle size and its impact on cell properties

One of the crucial properties of lithium-ion cells, power density, strongly depends on diffusion of lithium ions within solid-state active material. Diffusivity depends not only on electrode materials' crystal structure as discussed in section 2.1.2, but also on active material particle size. Moreover, shortening of ionic difussion path would result in reduction of particle size and thus enhance rate capability and power density on cell level. On the other hand, increased surface area resulting from reduced particle size facilitates side reactions that cause higher irreversible capacity losses, as well as faster ageing of cells [58]. Previous studies investigating nano-sized $LiCoO_2$ as potential cathode for high-power cells suggest that the optimal particle size in terms of rate capability exists in submicron range [59, 60].

Increased rate of diverse surface reactions due to higher surface area furthermore poses safety risks to cell. In cases where boundary layers are formed on electrode-electrolyte interphase, the amount of meta-stable compounds is thereby increased. It has been demonstrated for lithiated graphite of various particle size that heat generation during thermal decomposition

with electrolyte tightly correlates to surface area [61]. Furthermore, onset temperature of thermal decomposition is lower for graphite anodes with smaller particle size.

On cathode side, faster rate of oxygen release according to equation (2.3) (page 10) can be assumed for smaller particles of $Li_{1-x}CoO_2$. Correlation between thermal stability of cathode-electrolyte system and active material particle size has been proven previously [62]:

- Onset temperature for cathode-electrolyte reaction is lower for smaller $LiCoO_2$ particles
- Heating rate of the reacting system increases faster and is overall higher in case of smaller particles.

Above cited research by Jiang and Dahn deals with cathode-electrolyte system and does not investigate decomposition of dry $LiCoO_2$ cathodes. In such system, main source of exothermal heat is the reaction between $Li_{1-x}CoO_2$ or therefrom released O_2 (see equation (2.3)) and electrolyte. Impact of particle size / surface area on decomposition of LCO cathode itself is investigated in the scope of present dissertation.

2.4 Overlithiated oxides as new cathode materials

Even since commercialization of lithium-ion technology, new alternative cathode materials are being investigated to improve cell properties, particularly energy and power density. One group of proposed new materials are lithium-rich transition metal oxides with layered-layered structure [63]. They are commonly referred to as over-lithiated oxides (hereinafter: OLO). General formula of these materials is $xLiMnO_3 \cdot (1\text{-}x)Li[M]O_2$, where [M] stands for transition metals, most commonly Ni, Co, or Mn (therefore also known as LMO-NCM). Main advantages of these materials are high discharge capacity ($> 200\ mAh\ g^{-1}$) due to higher Li/[M] ratio [64] and lower cost due to lower cobalt content.

Structurally, OLO are similar to classical layered lithium - transition metal oxides cathode materials. Their XRD patterns correspond to layered R-3m structure with additional superstructral peaks [65]. On the other hand, cation ordering is similar to Li_2MnO_3, where lithium is also present in the transition metal layers. Structure of OLO material is shown on Figure 2.4.

OLO materials are distinguished from conventional cathodes by characteristic first cycle charge profile. During the first charge, lithium ions are extracted separately from LMO and NCM components. Figure 2.5 shows typical first cycle voltage profile. During the first charge plateau below 4.4 V, the NCM component is de-lithiated, just as in case of other layered oxides (LCO, NCM, NCA). Above 4.4 V, another plateau is formed as a consequence of LMO component (Li_2MnO_3) activation [63]. Since the manganese retains its 4+ oxidation state during charging, lithium extraction must therefore be compensated by oxygen oxidation, resulting in either gas release or formation of peroxide-like ionic environment [64]. In the course

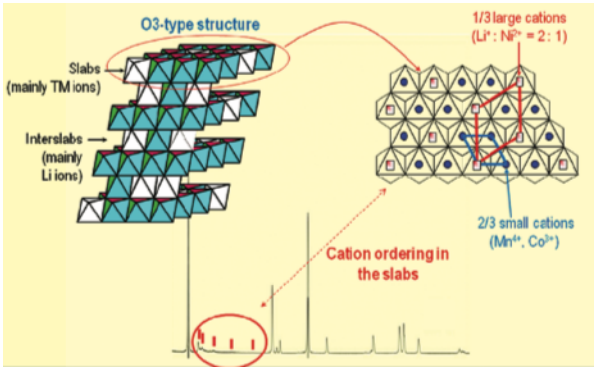

Figure 2.4: Crystal structure of lithium-rich cathode materials. Image copied from [66].

of first discharge, lithiation of the NCM component results in reduction of Co and Ni ions. This is followed by lithiation of LMO component at lower potentials. Second and subsequent charge steps are therefore different from first charge, since lithium is extracted first from the LMO and then from the NCM component [67].

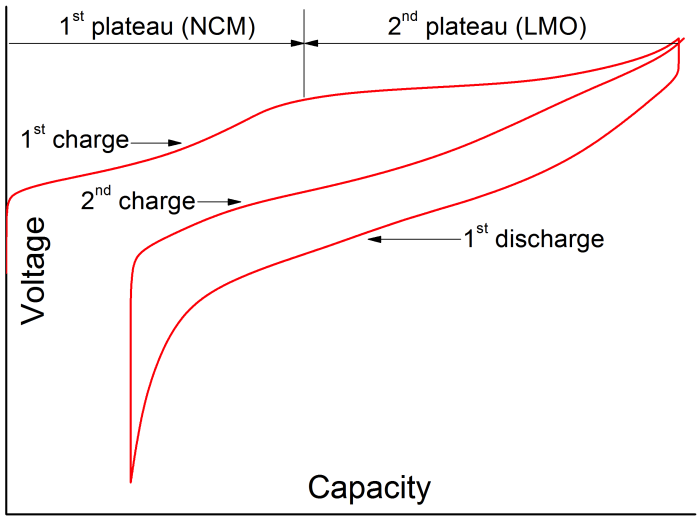

Figure 2.5: Characteristic first cycle voltage profile of an OLO cathode vs. $Li|Li^+$

Experiments utilizing differential electrochemical mass spectrometry (DEMS) have proven the O_2 gas emission during first charge [68]. It has been demonstrated that O_2 is released from particles' surface at the earlier phase of second plateau during first charge and structural oxygen oxidation occurs in the bulk at final stage of first charge [69, 70]. In addition to this, it is possible to impact the distribution of both LMO and NCM phases between bulk and surface of the active material particle by choosing the corresponding lithium source reagent (Li_2CO_3 or LiOH) during the synthesis [71]. By doing so, one may obtain stoichiometrically identical active materials with modified cycling behaviour due to different activation process on the surface and in bulk of the particles.

Involvement of oxygen in redox processes pertaining charging and discharging of a battery cell

raises concern about thermal stability of such cathode material and safety of OLO-based cell technology [72]. Released O_2 in the activation cycle per se poses a danger of fire in contact with flammable electrolyte and anode material at elevated temperature, it may however be properly removed during formation stage of manufacturing process. On the other hand, presence of ${O_2}^{2-}$ ions in crystal structure may lead to reduced thermal stability of material in charged state, as well as to increased O_2 formation during thermal decomposition at elevated temperature [73].

2.5 Objectives

Research in present dissertation investigates relations between active material microstructure and composition on safety of cells on two levels:

- In terms of cell lifetime
- In terms of certain cell design aspects

First, commercially available cells are aged under controlled conditions. Impact of ageing-induced changes within the cell (material structure, formation of side products) on thermal behaviour, stability, and safety is characterised on cell and material level separately. Table 2.2 gives an overview of experiments, which are described in detail in Chapter 3.

Table 2.2: Overview of experiments on aged and new cells

	Non-destructive characterisation	**Thermal and safety tests**
Cell	Impedance measurements Thermodynamics assessments Calorimetry (cycling)	Calorimetry (thermal runaway) Abuse testing
Material	Microscopy Crystal structure (XRD)	Thermal analysis Calorimetry

Non-destructive characterisation methods are used to evaluate crucial cell and material properties, and their changes over lifetime. Thermal and safety tests determine behaviour of cells and active materials under conditions of thermal runaway. The goal is to elaborate following:

1. How did ageing affect cell properties
2. Which changes are traceable to respective electrodes and their active materials
3. How do above mentioned property changes correlate with safety-related properties
4. Which thermal and safety-related phenomena is caused by changes in material structure
5. By what degree are safety and thermal stability improved or diminished by above mentioned changes

Second, material microstructure and its impact on safety are investigated from the point of

electrode design, with focus on cathodes. Active materials of commercially obtainable $LiCoO_2$, and overlithiated layered-layered material are prepared in different particle sizes. Cathodes from these active materials are characterized and tested by same techniques listed in the last row of Table 2.2.

Finally, a simple zero-dimensional cell-level mathematical model of thermal runaway is devised to investigate possible consequences of microstructure-related changes in materials' thermal stability on cell safety.

2.6 Hypotheses

1. Impact of ageing on cell safety is both stabilizing and de-stabilizing in terms of cells' thermal stability (cf. Table 2.1 on page 16). Both effects are overlapping and may be affected by ageing conditions.
2. Particle size and surface area of active materials play crucial role in balancing performance and safety of a given electrochemical Li-ion system. Optimum can be find in respect of both aspects and system can be optimized within given boundary conditions. Generally, smaller particles can boost rate capability and to some extent also energy density. By further reducing the size, problems such as irreversible capacity loss occur [74]. This has been investigated already and compromise size in terms of performance seems to exist in submicron size for $LiCoO_2$ system [59]. Similar shall be found for a given active material in terms of safety as well.
3. Over-lithiated layered-layered oxide cathode materials posses an additional safety issue due to oxide oxidation during charge. This process follows different reaction mechanism at particles' surface and in bulk material [69]. Variations in surface area / particle size and structural composition of active materials therefore have an impact on thermal stability. Mechanisms of surface area influences are different and more complex than in case of layered transition metal oxides such as LCO.
4. Stability level of lithium-ion battery materials and cells, which are by their nature meta-stable systems, is reflected by kinetic and thermodynamic contribution to apparent instabilities. Scope of these contributions is strongly dependent on active material structure and composition, and can be assessed by proper methods.

3 Experimental Methods and Procedures

3.1 Battery cell construction and disassembly

In order to investigate safety-related phenomena in Li-ion cells, both commercially available as well as self-made lab-scale cells have been used for research purpose. As described in Section 2.1, Li-ion cells consist of cathode, anode, separator, and electrolyte solution. Auxiliary components include current collectors, tabs, and housing. When the behavior of either cathode or anode needs to be insulated from the influences of the presence of the other electrode and their consequent interactions, it is common to use pure metallic lithium in stoichiometric excess as the counter electrode. This type of cell, comprised of investigated electrode on one side and metallic lithium on the other, is hereinafter referred to as **half cell**. Due to its low redox potential, lithium metal always acts as an anode in the half cell, even if the investigated electrode on the other side acts as a negative electrode in an actual Li-ion system (e.g. graphite electrode). A cell containing genuine Li-ion electrodes on both side is hereinafter called **full cell**. This designation consequentially applies also to all commercial cells used in this work.

3.1.1 Active materials

Several types of active materials have been used in the present research. By their origin, they can be divided into three groups:

- As-received active materials
- Synthesized active materials
- Structure- and surface-modified active materials

  Ball-milled active materials

  Polyimide coated Li-rich cathode materials

3.1.1.1 As-received active materials

A total of six active material powders were received by manufacturers. They were used in two ways: for preparation of electrodes in as-received state and as starting material for further structural modifications (ball milling and coating). Following materials were obtained for use

in the present research:

- Layered oxides (commercial, cathode grade) by ENAX (Japan)

  lithium cobalt oxide, $LiCoO_2$ (LCOar)

  lithium nickel cobalt manganese oxide, $Li[Ni_{1/3}Co_{1/3}Mn_{1/3}]O_2$ (NCM)

- Overlithiated layered-layered oxide (LMO-NCM) by Samsung SDI (Korea)

  $0.4Li_2MnO_3{-}0.6Li[Ni_{1/3}Co_{1/3}Mn_{1/3}]O_2$ (OLOar)

  $Ni_{0.2}Co_{0.2}Mn_{0.6}(OH)_2$ (precursor for synthesis of an active material with same molecular formula as above)

3.1.1.2 Sythesis of active materials

Two cathode active materials have been synthesized from precursors: $LiCoO_2$ and $0.4Li_2MnO_3$-$0.6Li[Ni_{1/3}Co_{1/3}Mn_{1/3}]O_2$ (overlithiated oxide, OLO).

The purpose of syntheses is to control and vary the particle size and surface area of active material powders. This is done by controling the temperature in the final synthesis step, i.e. calcination. $LiCoO_2$ was synthesized from commercially available chemicals following sol-gel method. OLO was prepared from precursor with formula unit $Ni_{0.2}Co_{0.2}Mn_{0.6}(OH)_2$, delivered by Samsung SDI, and $LiOH \cdot H_2O$ or Li_2CO_3 as lithium source.

Table 3.1: Input materials for sol-gel synthesis of $LiCoO_2$

Material	**Type**	**Mass**	**Amount**
$LiCH_3COO \cdot 2\,H_2O$	99.999% trace metal basis, Sigma-Aldrich	2.244 g	22 mmol
$Co(CH_3COO)_2 \cdot 4\,H_2O$	99.999% trace metal basis, Sigma-Aldrich	5.0 g	20 mmol
P123	average MW 1900 g mol^{-1}, Sigma-Aldrich	2.67 g	1.41 mmol

$LiCoO_2$ by sol-gel method

Hydrated lithium- and cobalt acetate (see Table 3.1) were dissolved in 200 ml ethanol. Surfactant P123[1] was added to solution. A 10 mol% excess of Li vs. Co is supposed to compensate lithium losses during annealing. Resulting solution was heated for two hours at 50°C, followed by slow evaporation of solvent at 70°C to form dried gel precursor.

Thermal annealing of precursors from sol-gel synthesis route was conducted in CARBOLITE ceramic furnace at atmospheric conditions. Precursors were heated from room temperature to annealing temperature at a rate of 5 K min^{-1} and kept at annealing temperature for several hours. Annealing temperature was varied between 600°C and 800°C. Dwelling time was varied between 2 h and 8 h. Final products were grounded in mortar to obtain active material.

[1] poly(ethylene oxide)-block-poly(propylene oxide)-block-poly(ethylene oxide)

Synthesis of $0.4Li_2MnO_3$-$0.6Li[Ni_{1/3}Co_{1/3}Mn_{1/3}]O_2$ from precursor
Precursor and lithium source were first homogenized in FRITSCH Pulverisette planetary ball mill. Tungsten carbide milling bowls were filled with following:

- 18 g of tungsten carbide milling balls (d = 5 mm)
- 1000 mg of $Ni_{0.2}Co_{0.2}Mn_{0.6}(OH)_2$ precursor
- 3% stoichiometric excess of lithium source, either one of the following (see section 2.4 and reference [71] for reason of using two different Li sources):

  594.8 mg Li_2CO_3 (ACS reagent $\geqslant$ 99.0%, Sigma-Aldrich)

  675.0 mg $LiOH \cdot H_2O$ (ACS $\geqslant$ 98.0%, Alfa Aesar)
- 5 ml ethanol (denaturated, 95% with 5% methanol) as liquid medium

The mixture was milled at 500 rpm for a total time of 12 h, consisting of 30 min milling intervals followed by 15 min pause intervals. Liquid product of milling was dried at 120°C and vacuum of 50 mbar for 12 h. Dried flakes were grinded in coffee mill to obtain powder. This was pressed into a 20 mm pellet. The pellet was first heated to 550°C for 5 h under atmospheric conditions in a ceramic box furnace (Nabertherm). Following the thermal treatment, the pellet was again grounded, only to be pressed into another pellet. This pellet was thermally annealed in the same furnace. Annealing started by increasing the temperature at a rate of 1 K min^{-1} until the annealing temperature (800°C, 900°C, or 1000°C) is reached. The pellet was held for 10 h at chosen annealing temperature and then allowed to slowly cool down in the furnace. The annealed pellet was grounded to provide active material powder.

3.1.1.3 Ball milling of $LiCoO_2$

One way to obtain $LiCoO_2$ with different particle size and surface area is ball milling of the pristine, as-received $LiCoO_2$ mentioned in 3.1.1.1. Batches of the active material were milled in FRITSCH Pulverisette planetary ball mill [67]. In each batch, 2 g of $LiCoO_2$ was milled together with 15 ml acetone as liquid medium. Milling was carried out in 15 min intervals, separated by 15 min pauses. Cummulative net milling time was limited to 7 h in order to avoid material degradation and decrease in lithium diffusion due to excessive milling [75]. Wet milled material was dried at 70°C and 50 mbar vacuum. Dried flakes were briefly grinded in coffee mill to obtain powder which is used as active material in cathode preparation (see Section 3.1.2).

Table 3.2 shows overview of milling condictions and resulting surface area (see section 3.6.2 for details on measurement method) of $LiCoO_2$.

Table 3.2: Milling parameters and resulting surface area of milled $LiCoO_2$

Time / h	**Rotational speed / min^{-1}**	**Milling balls**	**Balls/LCO weight ratio**	**Surface area / $m^2\ s^{-1}$**
0 (reference)	-	-	-	0.4
1	500	Stainless steel (5 mm)	15:1	4.6
2				14.4
3				16.0
5				18.3
7	750	Tungsten carbide (5 mm)	30:1	42.4

3.1.1.4 Polyimide coating of LMO-NCM

Commercially available polyimide resin binder (Dreambond 100 by Industrial Summit Technology Corporation) was used as polyimide oligomer precursor. This was diluted with N-methyl-2-pyrrolidone (NMP; ACS reagent $\geqslant$ 99.9%, Sigma-Aldrich) to produce a solution. The weight fraction of Dreambond in solution was 1%. Powder (OLOar) was dispersed into the solution in a weight ratio 20:1 versus the Dreambond resin. The suspension was treated by ultra-sonication for 2 hours to achieve uniform dispersion of LMO-NCM powder in the polyimide-NMP solution. Afterwards, the dispersion is filtered and vacuum dried to remove the solvent, obtaining the polyimide resin coated powder. Coated powder was annealed in a two-step thermal treatment: 300°C for 2 hours, followed by 550°C for 2 hours, both under argon atmosphere. This facilitates the imidization of polyimide resins on the surface and thus creates the coating.

3.1.2 Electrode preparation and battery cell assembly

Slurries for electrode coating were prepared by mixing 80% (by weight) active material, 10% conducting agent acetylene black (AB; 50% compressed 99.9% metals basis, Alfa Aesar), and 10% binder polyvinylidene difluoride (PVDF; HSV900, Kynar) as 6% solution in N-Methyl-2-pyrrolidone (NMP; ACS reagent $\geqslant$ 99.9%, Sigma-Aldrich). Mixture was homogenized in mortar and its consistency was adjusted by further addition of NMP. Homogenized slurry was then coated by doctor blade method on 15 μm aluminium foil. Coated foils were first dried on hotplate at 80°C for 3 h and then pressed between two aluminium sheets in a roll press with a gap of 100 μm. Rectangular electrodes (20 mm by 30 mm) were cut from the foil and fixed to aluminium tabs.

Electrodes' average coating weight was approximately 30 mg at 50 μm thickness, which implies 24 mg active material to be present in one electrode. This results in 3.4 mAh half-cell capacity or 0.57 $mAh\ cm^{-2}$ area-specific capacity for LCO-based electrodes; or a first-cycle discharge capacity of about 6.1 mAh or 1 $mAh\ cm^{-2}$ in case of OLO active material.

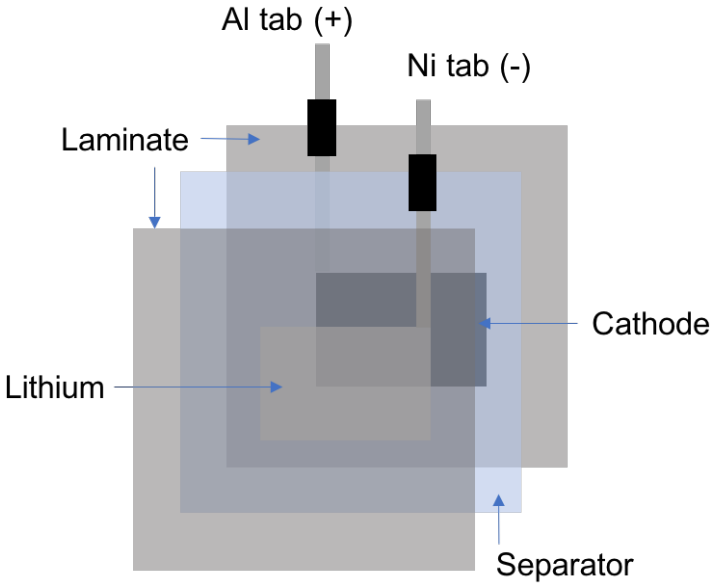

Figure 3.1: Scheme of a self-made pouch cell

Table 3.3: Overview of electrolytes used in self-made pouch cells

Electrode active material	**Electrolyte**	**Origin**
LMO-NCM	1 M $LiPF_6$ in FEC/DEC (1:1 by vol.)	Solvionic
$LiCoO_2$	1 M $LiPF_6$ in EC/DEC (1:1 by vol.)	DANVEC

Electrodes were dried in a glass tube oven (Büchi) for 12 h, under vacuum at 110°C to remove any traces of water before being transferred to argon-filled glovebox. Aluminium laminate sheets (60 mm by 60 mm, for pouch cell housing) and polypropylene/polyethylene/polypropylene separator (60 mm by 50 mm, Cellgard 2320) were dried overnight under vacuum at 50°C and transferred to glovebox. In glovebox, cells were prepared by stacking laminate sheet, electrode, separator, lithium counter-electrode, and another laminate sheet (see Figure 3.1). The stack was then sealed one three edges. Electrolyte was pipeted to the cells through the remaining open edge. Electrolytes used are listed in Table 3.3. By dosing the electrolyte in excess of at least 5 μl electrolyte per 1 mg electrode coating, it was ensured that ionic conductivity in cell is not limited by electrolyte. Electrolyte filled cells were vacuumed for short time to minimize amount of gas bubbles inside. Afterwards, the remaining open edge was sealed.

3.1.3 Commercial cells and their cycle ageing

Commercially available cells were used in experiments investigating relationship between cell lifetime and safety (see Chapter 4). For this purpose, cylindrical Panasonic CGR18650CH cells were used, with NCM and graphite as active materials in cathode and anode, respectively.

They are labeled as high-power cells, with nominal voltage of 3.6 V, nominal capacity of 2.15 Ah, typical capacity of 2.25 Ah, and maximum discharge current of 10 A (4.65C). With a typical weight of 44 g, their nominal energy density equals 176 $Wh\ kg^{-1}$. Voltage range of operation is between 3.0 V and 4.2 V.

To investigate considerations laid out in section 2.2, commercial cells were cycle aged under controlled temperature of 25°C. Fifteen cells were divided into five batches, with 3 cells per batch. First batch was kept at 60% SOC and 25°C without being cycled and served as a reference. Other four batches were cycled at same temperature with difference charge currents in terms of the C-rate: 0.2 C (Batch A), 0.5 C (Batch B), 1 C (Batch C) and 2 C (Batch D). BaSyTec CTS battery tester was used therefor. During cycling, cells were charged at respective currents up to 4.2 V and held at 4.2 V until the charge current dropped below 0.11 A. Cells were discharged at a rate of 1 C (2.15 A) until the voltage reached 3 V. Between each charge and discharge, 30 minutes pause occured. Cycling lasted until the remaining capacity was halved, but not longer than 6 months.

3.1.4 Active material sample preparation

Self-made half-cells (Section 3.1.2) were disassembled in argon-filled glovebox. Aluminium laminate was cut open with scisors. Cathode was removed and thoroughly washed with dimethyl carbonate (DMC) and dried under vacuum ($p \leqslant 50\ mbar$) in a glass tube oven (Büchi) for 12 h.

In order to characterise the active materials in aged and new 18650 cells, cells were opened at fully charged state in a glovebox. Pipecutter was used to cut through the slit in the housing near the positive pole. The latter was thus removed and remaining steel housing was peeled off the jelly roll. Jelly roll was unrolled and electrodes were separated. Both anode and cathode were scratched off the current collector and divided into two batches each. One batch was thouroughly washed with DMC and dried under vacuum ($p \leqslant 50\ mbar$) in a glass tube oven (Büchi) for 12 h. Other batch was sealed into sample container (for ARC and TGA/DSC) without prior washing, i.e. soaked in electrolyte.

3.2 Electrochemical characterisation

3.2.1 Charging and discharging cells

Both self-made and commercial 18650 cells were cycled with BaSyTec CTS battery tester. Cylindrical 18650 cells are connected via Kelvin probes (4-point measurement). Charging and discharging occurred inside a chamber at controlled temperature of 25°C. Cells were cycle aged as described in Section 3.1.3.

Pouch cells are connected by crocodile clips. Cells with LCO cathodes were charged with a current of 13.69 mA per gram active material (equivalent to a C-rate of 0.1) to a voltage of 4.2 V. Constant voltage charging at 4.2 V was continued until the current dropped to 10% of initial value. Afterwards, discharge with same current to a voltage of 3.0 V followed. Finally, the cells were charged again to cumulative capacity of 136.9 mAh g^{-1}, which is equivalent to cathode composition of $Li_{0.5}CoO_2$.
LMO-NCM half cells were cycled between 2.0 and 4.8 V with a current of 25 mA per gram active material (roughly corresponding to $0.1C$), without a constant voltage charge phase.

3.2.2 Electrochemical impedance spectroscopy (EIS)

EIS measurements were conducted on new and aged 18650 cells in order to observe changes in cell impedances. Measurements were carried out at various states of charge between 10 kHz to 5 mHz at 10 frequency points per decade. Measured impedance spectra were fitted to equivalent circuit model shown on Figure 3.2. The model contains the three relevant resistances:

- Ohmic resistance R_{ohm}
- Solid-electrolyte interphase (SEI) resistance R_{SEI}
- Charge transfer resistance R_{ct}

Additionally, the diagram contains two constant phase elements representing double-layer capacitance, Warburg impedance representing diffusion in a porous electrode, and a series inductance.

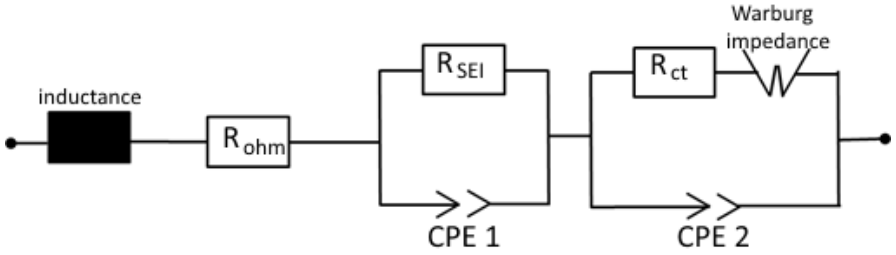

Figure 3.2: Diagram of the equivalent circuit model for fitting of EIS data [76]

Fitting of the impedance spectra was done by a MatLab script whose input was a set of discretionary defined initial parameters corresponding to aforementioned circuit elements. The script utilises the *fminseach* function, based on Nedler-Mead simplex algorithm [77]. This method enables fitting of parameters by iterative minimisation of least squares for each point in the impedance spectra.

3.2.3 Thermodynamic measurements

Changes in specific entropy (ΔS) of cell's underlying electrochemical reaction are measured at different SOC levels for new and aged 18650 cells. Temperature dependence of cell's open circuit voltage (U_{OCV}) can be used to measure entropy, as described by equation (3.1) [78]:

$$\Delta S = zF\frac{\partial U_{OCV}}{\partial T} \tag{3.1}$$

New and aged cells at a fully charged state underwent temperature cycle at 15°C, 25°C, 30°C, and 40°C. At each temperature step, the cells were kept in relaxation state for 90 min to obtain voltage equilibrium. At the end of the relaxation state, OCV of the cells was measured. After the completion of temperature cycle, the cells were discharged by increments of 10% SOC. At the end of each step discharge, the temperature cycle was repeated. The tests continued until the entropic heat coefficient was calculated at 11 points from 100% to 0% SOC [79].

3.3 Thermal analysis

Thermal analysis is a set of methods where changes in certain physical property of a sample under imposed temperature alteration are analysed as a function of time or temperature [80]. In scope of present research, two measurements are conducted simultaneously:

- Thermogravimetric analysis (TGA): Sample mass is measured as function of temperature
- Differential scanning calorimetry (DSC): Heat flow between sample and reference is measured as function of temperature

Samples were prepared in a glovebox. For one measurement, approximately 35 mg of electrode powder was sealed into a 100 μl aluminum crucible. Cathodes were washed and dried before sealing, while anodes were soaked in their cell's own electrolyte. Analyses were conducted in a MettlerToledo STARe TGA/DSC1 thermal analyzer. Crucible lid was pierced by sampling robot just before it was placed into chamber. All analyses were conducted in argon atmosphere with a flow of 50 ml min^{-1}. At starting temperature of 25°C, the chamber was purged with argon flow for 30 minutes. This was followed by a linear ramp with a temperature rate of 5 K min^{-1} until 600°C is reached.

3.3.1 Reaction kinetics evaluation by thermal analysis

Kinetics of a decomposition reaction, more particularly activation energy, can be determined from thermal analysis data. There are multiple approaches to evaluate reaction kinetics from thermal analysis data [81]. Decomposition of complex systems such as electrodes of lithium-ion batteries often consists of several parallel and subsequent chemical reactions (see 2.1.1).

It is difficult to accurately describe the reaction mechanism of the decomposition as a whole, therefore a method independent of reaction model is needed. In present research, Friedman-Ozawa method [82, 83] is used to evaluate kinetics of decomposition reactions. It is based on assumption that the reaction rate, defined as first-order derivative of conversion α over time, equals at any time to a product of temperature-dependent factor $k(T)$ and conversion-dependent factor $f(\alpha)$ (the reaction model).

$$\frac{d\alpha}{dt} = k(T) \cdot f(\alpha) \tag{3.2}$$

In case of linear temperature ramp during thermal analysis, temperature equals the product of time and temperature rate β. Temperature-dependent factor $k(T)$ is assumed to follow Arrhenius equation. Thus, the equation (3.2) can be rearranged to:

$$\beta \cdot \frac{d\alpha}{dT} = k_0 \exp\left(-\frac{E_a}{R_m \cdot T}\right) \cdot f(\alpha) \tag{3.3}$$

In logarithmic form, one obtains a linear relationship between the logarithm of conversion rate and the inverse of temperature, with activation energy E_a as the factor.

$$\ln \beta \frac{d\alpha}{dT} = -\frac{E_a}{R_m}\frac{1}{T} + \ln\left(k_0 f(\alpha)\right) \tag{3.4}$$

TGA of an equal sample was done at various temperature rates (5, 10, 15, 20 K min^{-1}). Ratio between remaining mass at given time to initial mass is taken as a measure of conversion. At any fixed value of conversion, the apparent activation energy can be calculated by means of linear regression according to equation (3.4) [83, 84].

3.3.2 Evolved gases analysis by mass spectrometry (MS)

During the thermal analysis measurements, gaseous substances are emitted from sample either by evaporation or thermal decomposition. The chamber of thermal analyser is connected to a quadruple mass spectrometer (Pfeiffer Thermostar GSD3200) via thin quartz capillary. All evolved gases during the measurement are carried by argon flow and a fraction of them enters the capillary. Mass spectrometer is set to detect frequency of certain ionic fragments. Gases that are emitted during electrode decomposition, such as O_2, CO_2, HF, are of particular interest. Spectrometer is operated in multiple ion detection (MID) mode, monitoring ten mass-to-charge (m/z) ratios: 12, 14, 16, 18, 19, 20, 28, 32, 40, and 44. Dwell time for each fragment was set to 100 ms.

Normalisation of the ionic currents has to be done in order to make MS results mutually comparable [85]. There are several methods available [86]. In present research, each ionic current is divided by the sum of all ionic currents in the given dataset. In addition, the resulting signal is further normalized to sample mass.

3.4 Accelerating rate calorimetry (ARC)

Accelerating Rate Calorimetry (ARC) is an adiabatic calorimetric method commonly used for observing temperature profiles of exothermal reactions. Scheme of the experimental setup and functioning principle are shown on Figure 3.3.

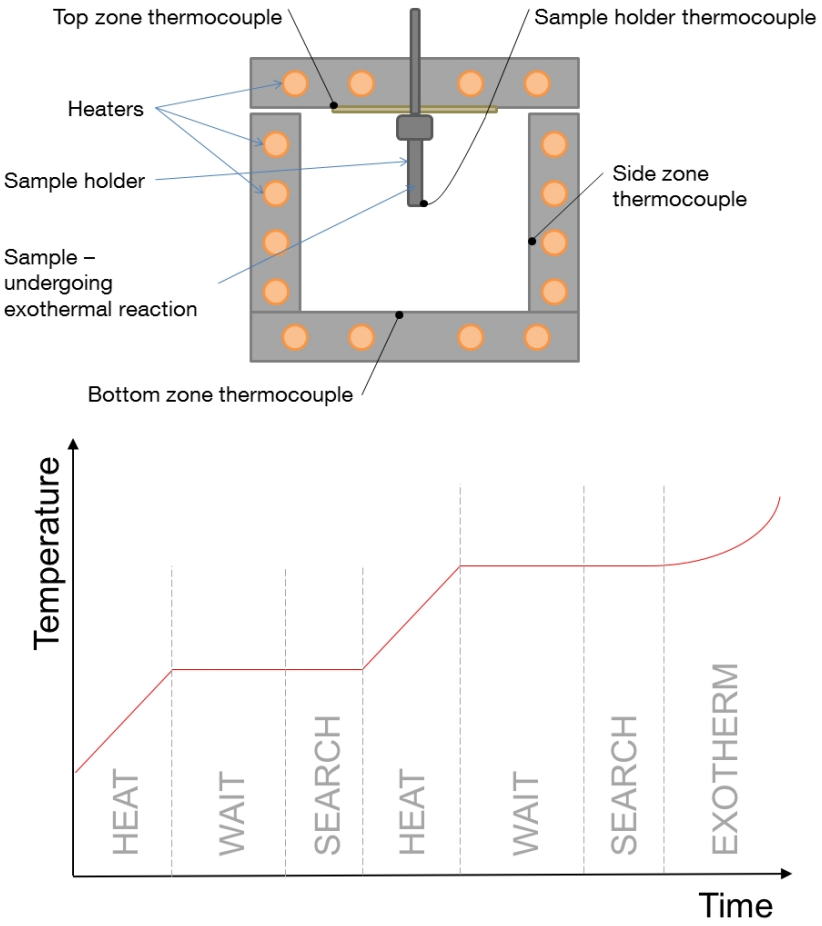

Figure 3.3: Scheme of the ARC experimental setup (above), illustration of heat-wait-search (HWS) analysis (below)

The investigated sample is contained inside the calorimeter. Heaters in the calorimeter walls react to any temperature increase by heating the whole system in order to adapt its temperature to the sample temperature. Procedure is known as quasi-adiabatic tracking and ensures that there is no heat transfer between the sample and its environment, thus mimicking the adiabatic conditions. This imitates the worst-case scenario in case of thermal runaway, where no heat is dissipated from the sample.

The original ARC analysis method involves inducing and tracking a thermal runaway, which is known as Heat-Wait-Search (HWS). In the first phase ("heat"), the calorimeter is heating and the sample and itself to the starting temperature. In the next phase ("wait"), temperature

of sample and calorimeter are sustained to reach a thermal equilibrium within the system. This is followed by "search" phase, where temperature of sample is monitored to detect any self-heating as a result of an exothermal reaction. If self-heating is detected, the calorimeter tracks temperature increase in the sample by correspondingly adapting its own temperature. In absence of self-heating, the calorimeter incrementally increases temperature to next step and repeats the HWS procedure.

Result of ARC measurement is a thermal profile (temperature over time of experiment). Rate of temperature increase, i.e. first derivative of temperature over time, is referred to as self-heating rate (SHR).

3.4.1 Battery cell calorimetry

Battery cells were tested in ARC in two different situations:

- HWS analysis of a fully charged cell (destructive test resulting in thermal runaway)
- Charging and discharging the cell (non-destructive test)

First test is quantitative observation of thermal runaway. HWS method induces thermal runaway by step-wise heating of the cell. Results reveal onset temperature of thermal runaway and the thermal profile thereof. Fully charged cell is contained in a hollow thin-walled steel cylinder. Thermocouple is attached to sample container from outside, as shown on Figure 3.3.

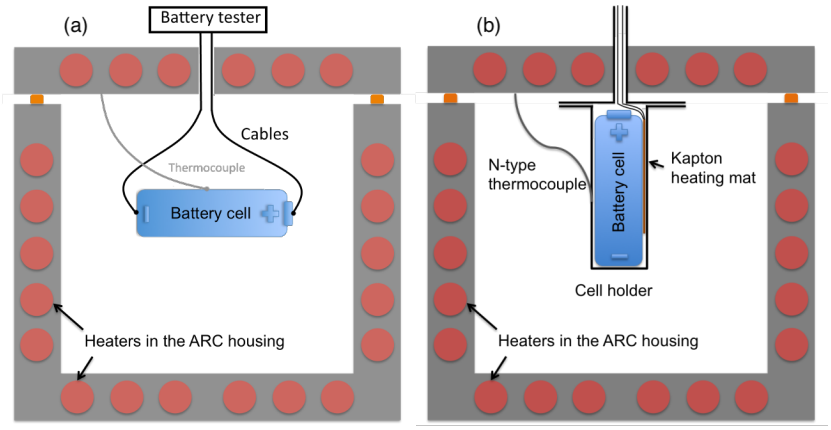

Figure 3.4: Schematic representation of ARC test setups for (a) charging/discharging the cell and (b) heat capacity determination

Second test determines heat resulting from charging and/or discharging the cell. Test setup is shown on Figure 3.4(a). Cables are soldered on the poles of the cell which is hanging inside the calorimeter, connected to BaSyTec CTS cycler outside. The system is first heated to 27°C and undergoes the "wait" phase to reach thermal equilibrium. During the "search" phase, charge or discharge is triggered by the cycler. Calorimeter tracks the resulting temperature

increase. Heat flow emitted by the cell can be calculated using the equation (3.5).

$$\dot{Q} = m\ c_p\ \frac{dT}{dt} \tag{3.5}$$

Heat capacity of the cell has to be determined in order to calculate heat flow from self-heating rate. Setup for heat capacity determination is same as setup for HWS analysis. Additionally, a resistive Kapton heating mat is wedged between cell and wall of sample container on the opposite side of thermocouple position, as shown on Figure 3.4(b). Calorimeter is first heated to 27°C. During search phase, DC current with a power of 0.2 W (5 V, 40 mA) is delivered to heating mat. Calorimeter starts tracking the temperature in response to its increase. Test is limited to 60°C. Assuming a 100% efficiency of the heating mat, one can calculate cell heat capacity according to equation (3.6).

$$P = \dot{Q} = (m_{cell}\ c_{p(cell)} + m_{container}\ c_{p(container)})\ \frac{dT}{dt} \tag{3.6}$$

Heat capacity of the sample container is determined in a separate measurement using an aluminium cylinder with known heat capacity in place of a cell.

3.4.2 ARC of electrode-electrolyte system

Electrolyte-soaked electrodes were tested in ARC to observe their behavior in conditions of thermal runaway. Electrodes from disassembled fully charged 18650 cells were immediately scratched off their current collector foils and transferred to a thin-walled titanium tube sample container with a diameter of 6.35 mm (0.25 inch) and a length of 5 cm (anode) or 3 cm (cathode). Total sample mass was 0.8 mg. Container was sealed with a Swagelok fitting and mounted into calorimeter as shown on Figure 3.3.

Electrodes from laboratory-made cells were washed and dried first. Powdered sample (100 mg) was then transferred to titanium tube with an addition of 50 μl of corresponding electrolyte. Container was sealed as described in above paragraph.

3.5 Abuse testing of battery cells

New and aged 18650 battery cells underwent blunt nail indentation test. Cells were mounted in a cell holder below an INSTRON 5966 Dual Column tabletop testing system, as shown on Figure 3.5. A blunt nail is driven into the cell at a constant displacement rate of 1 mm s^{-1}. During the measurement, cell voltage, cell surface and nail temperature, as well as force are recorded.

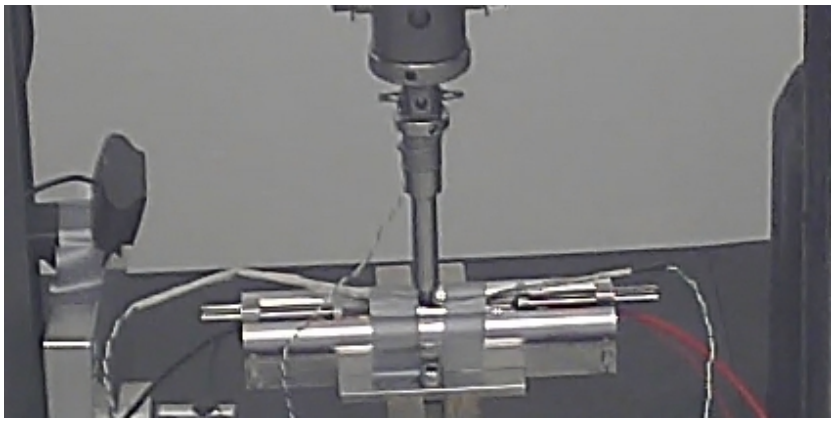

Figure 3.5: Experimental setup for blunt nail indentation test

3.6 Material characterisation

3.6.1 Spectroscopy and imaging methods

X-ray diffraction (XRD) spectroscopy
Crystal structure of active materials was characterised by Rigaku SmartLab XRD in the range of $15° < \theta < 70°$ with Cu-Kα radiation (U = 45 kV, I = 100 mA).

Raman spectroscopy
Raman spectra of $LiCoO_2$ were taken in order to validate crystal structure. Measurements were made by Renishaw Raman Spectroscopy PM1000 with a He-Ne laser (λ = 633 nm) and X50 objective. Scanning area was 3.14 μm^2 and beam power 1 mW.

Electron microscopy
Various electrode powders were analysed by field emission scanning electron microscope (FE-SEM), FEI Inspect F50.
To characterise polyimide coating of LMO-NCM (OLOar) particles, Tecnai X-TWIN transmission electron microscope (TEM) was used. The microscope utilises a 200 keV field emission electron gun and has a resolution of 0.14 nm. Probe current equals 0.4 nA.

3.6.2 Surface area determination

Surface area a_s of cathode powders used for self-made cells was determined by multi-point Brunauer-Emmett-Teller (BET) isotherm measurement. Analysis was carried out by Autosorb iQ-MP gas sorption analyser. Pure nitrogen was used as adsorbing gas. Sample powders (approximately 2 g) were measured in tubular cells with a diameter of 9 mm. Before the analysis, powders were dried at 150°C for 4 hours.

3.6.3 Chemical delithiation of cathode active material

In order to separately observe decomposition reactions of charged active material (free of additives), $Li_{0.5}CoO_2$ was prepared by de-intercalating the Li^+ ions from the crystal structure chemically. Reaction occurs according to equation (3.7) (x = 0.5 in given case).

$$LiCoO_2 \; + \; \frac{x}{2}K_2S_2O_8 \; \rightarrow \; Li_{1-x}CoO_2 \; + \; \frac{x}{2}K_2SO_4 \; + \; \frac{x}{2}Li_2SO_4 \tag{3.7}$$

$LiCoO_2$ powder was dispersed in stoichiometric amount of 0.15 M aqueous solution of potassium persulfate ($K_2S_2O_8 \geqslant 99\%$ by Sigma-Aldrich). Suspension was kept under constant stirring at 55°C for 72 h. Afterwards, liquid phase was removed by filtration. Solid remaining was thoroughly washed with de-ionised water at 55°C and dried under vacuum for 72 h.

4 Thermal Behaviour and Safety of Lithium-Ion Battery Cells

4.1 Influence of lifetime on cells' thermal and electrical properties

Cyclic ageing outcome of NCM-graphite cells (Panasonic CGR18650CH) is summarised in Table 4.1.

Table 4.1: Cycle ageing results of 18650 cells ($U_{disch} = \frac{E_{disch}}{C_{disch}}$)

Batch	I_{ch}	N_{cyc}	C_{disch}	$\bar{C}_{disch}$	E_{disch}	$\bar{E}_{disch}$	$\bar{U}_{disch}$
Ref.	n/a	0	2.19 Ah 2.28 Ah 2.28 Ah	2.25 Ah (100%)	7.86 Wh 8.23 Wh 8.25 Wh	8.12 Wh (100%)	3.61 V
A	0.2 C	700	1.83 Ah 1.98 Ah 2.04 Ah	1.95 Ah (86.7%)	6.60 Wh 7.15 Wh 7.25 Wh	7.00 Wh (86.2%)	3.59 V
B	0.5 C	1000	1.20 Ah 1.23 Ah 1.29 Ah	1.24 Ah (55.1%)	4.15 Wh 4.25 Wh 4.53 Wh	4.31 Wh (53.1%)	3.48 V
C	1 C	600	0.96 Ah 1.21 Ah 1.34 Ah	1.17 Ah (52.0%)	3.34 Wh 4.23 Wh 4.76 Wh	4.11 Wh (50.6%)	3.51 V
D	2 C	300	1.04 Ah 1.07 Ah 1.19 Ah	1.10 Ah (48.9%)	3.72 Wh 3.74 Wh 4.18 Wh	3.88 Wh (47.8%)	3.53 V

Batch A did not meet the end-of-life (EOL) criteria within the cycling period, limited to six months. Batches B, C, D have their available capacities nearly halved. Remaining discharge energies are reduced even further, indicating the increase of cell resistance or voltage fade as consequence of ageing.

For batches B, C, and D, one can observe exponential decline of cycle number (before capacity and/or energy are nearly halved) with increasing charge current. Above reported outcome of cell ageing enables comparison of following:

- Fresh non-aged cells (reference)
- Mildly aged cell with SOH 86%

- Three batches of severly aged cells (SOH $\sim$ 50%) with different number of cycles and charge currents during ageing

Figures 4.1 and 4.2 compare SEM images of new and aged cells' electrodes. Batch C is representative of aged electrodes and no quantifiable differences are seen between various aged batches. All available SEM images are shown in Appendix A.1. There are notable amounts of deposited material on aged anode's particles, likely related to SEI growth. Comparison of fresh and aged cathodes reveals further differences:

- At lower magnification, significant changes in homogeneity of cathode is observed.
- In more detailed view at high (50000x) magnification, several micro-cracks are observed in active material particles.

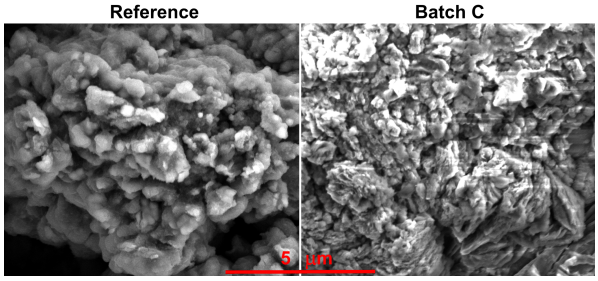

Figure 4.1: SEM images of anode from reference and aged (Batch C) cell (30000x magnified)

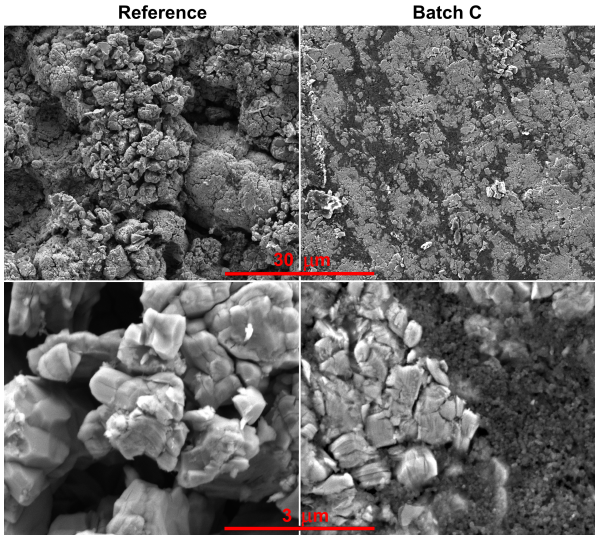

Figure 4.2: SEM images of cathode from reference and aged (Batch C) cell (magnification above: 5000x, below: 50000x)

Resistances resulting from EIS measurements are shown on Figure 4.3. Highest increase of all resistances is consistently observed in batch B, followed by batches C and D. This implies that for equal decline in state of health, number of cycles plays a more critical role than charge current. Results show that all impedances from proposed equivalent circuit (see Figure 3.2) increase in similar trend from one batch to another. Most significant is the increase in charge

transfer resistance R_{ct}. This is related to ageing-induced surface changes on active material particle surfaces and seemingly contributes more to overall impedance rise than SEI growth or increase in ohmic resistance due to changes in electronically conductive components of the cell.

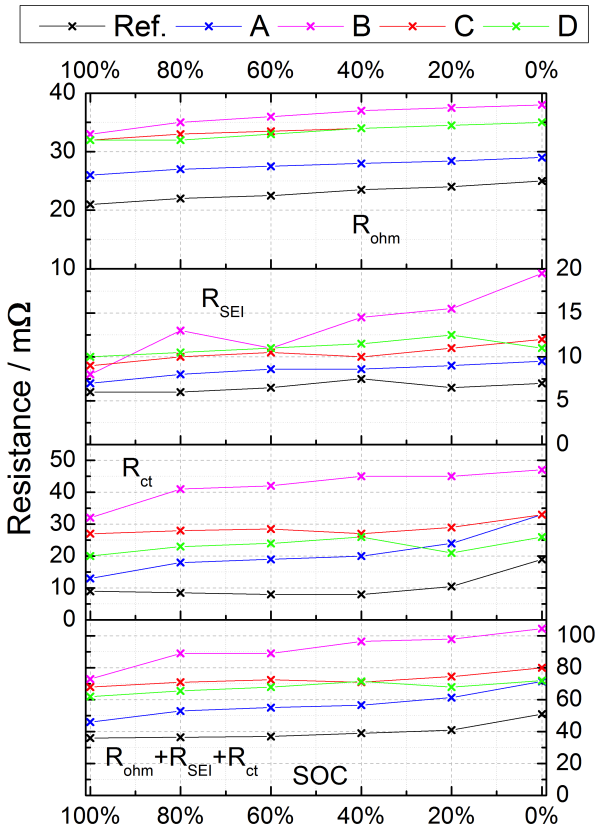

Figure 4.3: Impedances of cells at various SOC, as measured by EIS [79]

Figure 4.4 shows specific entropy change of cells' underlying electrochemical reaction. Comparing heavily aged batches B, C, D to reference non-aged cell and mildly aged batch A reveals following:

- Decrease in entropy at lower SOC is caused by irreversible loss of cyclable lithium [87], causing higher values of x in $Li_{1-x}Ni_kCo_lMn_mO_2$.This allows more disordered crystal structure of NCM in discharged state of the cell.
- Disappearance of $\Delta S > 0$ region between 60% and 30% SOC.

Both phenomena point at ageing-induced imbalance between anode and cathode [87].

Cell resistance and entropy are decisive factors impacting thermal behaviour during charge and discharge. Heat flow emitted by cell can be divided into two contributions:
Reversible heat flow caused by electrochemical reaction is a function of current and entropy. Depending on current direction and entropy sign (+/-), it can be exothermal (cell emits heat)

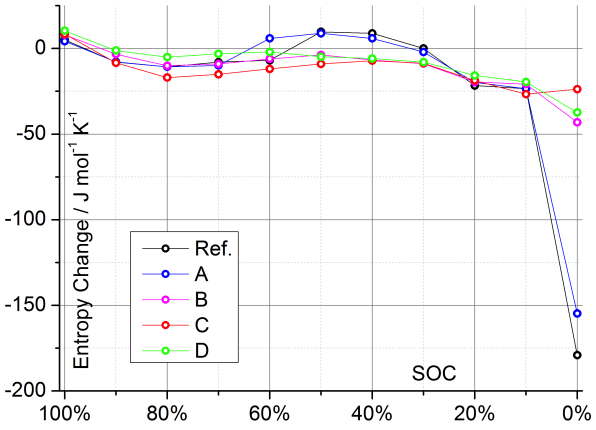

Figure 4.4: Calculated change of entropy for new and aged 18650 cells [79]

or endothermal (cell absorbs heat):

$$\frac{dQ_{rev}}{dt} = \frac{I}{z \cdot F} \cdot T \cdot \Delta S \tag{4.1}$$

Irreversible heat flow is a consequence of resistive Joule heating. It is approximately proportional to square of current and is always exothermal:

$$\frac{dQ_{irrev}}{dt} = R_{total} \cdot I^2 \tag{4.2}$$

Thermal behaviour of cells during discharge is shown on Figure 4.5. Heat flow magnitude for cells of various batches is in good agreement with impedance data from Figure 4.3. Irreversible heat is the dominant cause of cell heating, particularly for severely aged cells of batches B, C, and D. Negative reaction entropy in the region $30\% < \mathrm{SOC} < 60\%$ is the cause of a slight decline in heat generation rate for reference and batch A cells in the same range, while no such phenomenon is observable in batches B, C, and D. Cell of batch B, which exhibits highest heat generation rate due to high impedance, reaches 60°C at the end of discharge. This is usually the highest permissible temperature for storage and operation of Li-ion batteries. It has to be noted at this point that the given high-power 18650 is rated for discharge currents of up to 10 A (4.65C), while the test has been conducted at 2.15 A (1C), albeit at adiabatic conditions.

It shall be recalled that the calculation of reversible heat generation is based on an estimation. The method of determining the entropic heat coefficient is based on several simplifying assumptions and bears a significant experimental error. It is particularly challenging to accurately determine the coefficient at low voltages due to long relaxation times [79]. Therefore, the profiles of reference cells and less aged cells at low SOC imply reversible heat generation higher than the total heat generation, which is physically impossible.

Changes in thermal behaviour also impact the energy efficiency of the cell. Overall efficiency of energy storage by lithium-ion battery can be defined as ratio of electric work yielded during

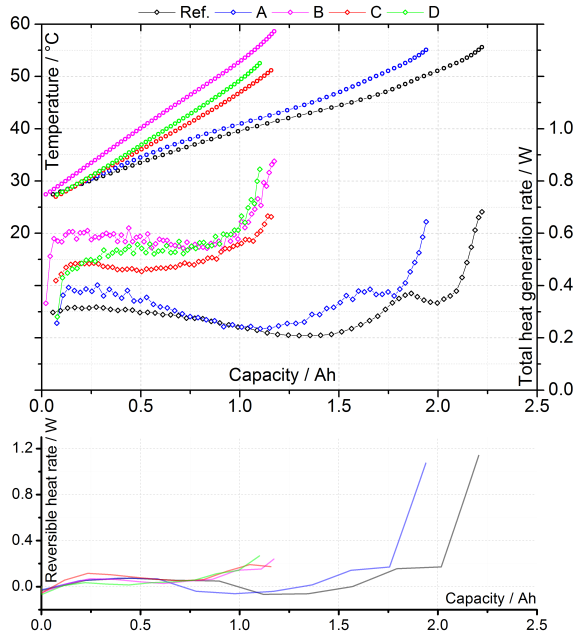

Figure 4.5: Temperature increase and total heat flow as function of discharge capacity during discharge at adiabatic conditions (ARC). The reversible heat flow below is estimative calculation based on equations (3.1) and (4.1) [79]

discharge to electric energy consumed by charge:

$$\eta = \frac{W_{disch}}{E_{ch}} \tag{4.3}$$

For consideration of discharge process only, half-cycle discharge efficiency is defined as ratio of electric work yielded to total energy released, which is sum of work and heat:

$$\eta_{disch} = \frac{W}{E} = \frac{W}{W + Q} \tag{4.4}$$

Figure 4.6 shows total amount of heat released from cells of different batches and respective discharge efficiencies. While the reversible heat emission of heavily aged cells from batches B, C, and D decreases (mainly due to absence of entropy decline at lower SOC, cf. Figure 4.4), total heat emission per unit of discharge capacity/energy is increased greatly by irreversible heat generation. Due to reduction in discharge efficiency at 1C from 96.36% (reference) to 92.69% (batch B), the amount of heat generated per unit of electric work yielded more than doubles. Effect is even more prominent at higher currents, because of square relation between Joule heating and current. This poses a considerable risk for cell safety related to increase of cell temperature, which may lead to thermal runaway. Temperature-induced thermal runaway is discussed in next section.

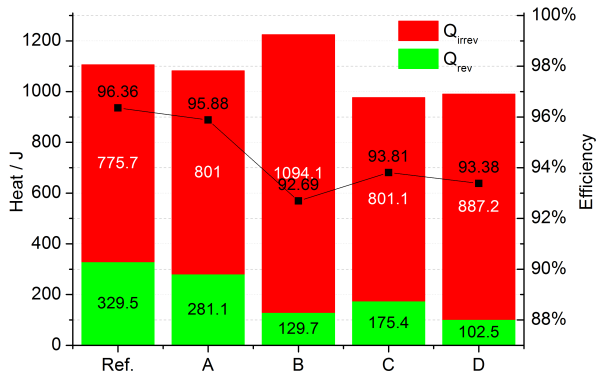

Figure 4.6: Cumulative heat released by cells during adiabatic discharge and discharge efficiency. Share of reversible heat is an estimative calculation based on equations (3.1) and (4.1) [79]

4.2 Impact of ageing on safety and thermal stability

4.2.1 Thermal stability of new and aged electrodes

4.2.1.1 Anode

ARC and DSC results of anode-electrolyte reaction are presented in the Figure 4.7. Heat-induced thermal runaway of Li-ion cells begins with decomposition of the metastable SEI layer on anode surface, and continues with reaction between intercalated lithium and graphite, followed by reaction of lithium with fluorinated binder (PVDF) [28].

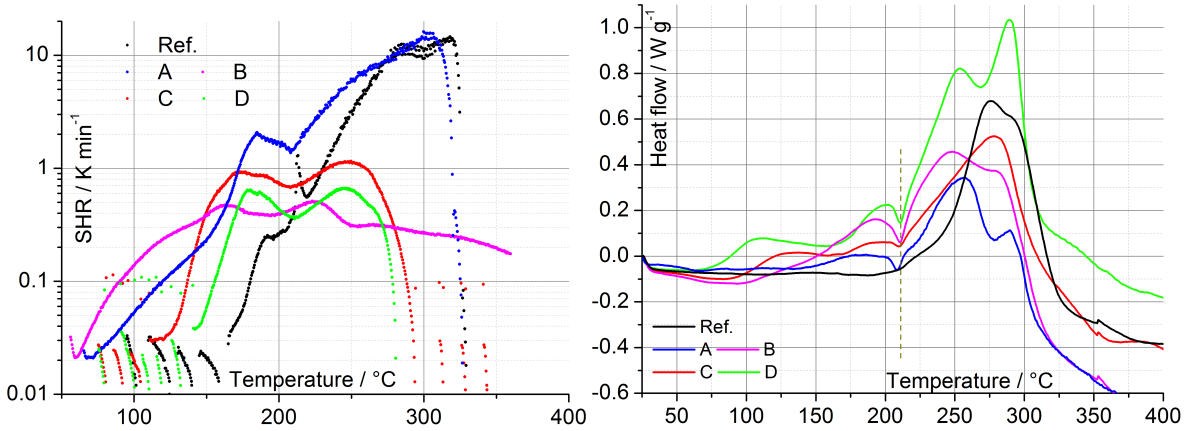

Figure 4.7: ARC thermal runaway profiles of electrolyte-soaked anodes (left). DSC curves of electrolyte-soaked anodes (right, $\beta = 10$ K min^{-1})

Initial exothermal reactions can be observed for anodes of reference cells, and cells C and D, as series of exotherms with decelerating self-heating rates (Figure 4.7, left). It should be noted that after the heating rate drops below 0.01 $K\ min^{-1}$, the calorimeter will react by re-entering the heat-wait-search procedure as described in section 3.4. For aged anodes in batches A and

B, a declining self-heating rate is observed initially as well, but it does not decrease below 0.01 $K\ min^{-1}$ so the exotherm is not terminated. A self-sustaining exothermal reaction is followed immediately and heating rate continues to increase. While ageing in general lowers the onset temperature of SEI decomposition, it is notable that stability of anodes with higher cycle number (batches A and B) is reduced further compared to those with lower cycle number at higher current.

All exotherms are characterised by two separate peaks between 150°C and 300°C. These are related to above mentioned reaction of intercalated lithium with electrolyte and binder. For reference and batch A cells (SOH 100% and 86.77%), second peak is higher, presumably due to more lithium available (smaller loss of cyclable lithium compared to cells at SOH $\sim$ 50%). On the other hand, initial reaction is increasing faster at lower temperature for aged anodes with higher cycle number. By observing the (arbitrary) threshold of $SHR = 0.1\ K\ min^{-1}$, one notes that exothermal profile of anodes with higher cycle number consistently cross this threshold at lower temperature. This is caused by growth of SEI, where total cyclic ageing time, and thus the number of cycles, plays more significant role than the magnitude of cycling current. Thus, the anode reaction is triggered earlier in more aged anodes (in terms of cycle number). On the other hand, fresh and mildly aged anodes have considerably higher potential of heat release. High current aged anode with lower cycle number exhibit the onset of self-sustaining reaction lower than fresh anodes, but higher than those undergoing more cycles. Two important conclusions can be drawn from ARC results:

1. High number of cycles $\Rightarrow$ Larger growth of SEI $\Rightarrow$ Lower onset of long-term self-sustaining decomposition reaction
2. Higher remaining capacity (SOH) $\Rightarrow$ More intercalated Li available $\Rightarrow$ Higher cumulative heat release potential

It is notable that thermally less stable SEI is not necessarily reflected by increased SEI impedance (cf. R_{SEI} for batches A and B in Figure 4.3) in case of the aged cells. All aged cells exhibit an increased R_{SEI} compared to reference cell, however it appears that resistivity / conductivity of the ageing-enlarged SEI does not correlate to its thermal stability.

Figure 4.7 (right) shows DSC curves of same anodes. There are two important differences between ARC and DSC analysis in given case:

1. ARC is an adiabatic method, where an exothermal reaction is induced thermally by step-wise heating. In exotherm mode, all heat is provided to system by the sample. In DSC, heat is introduced externally by temperature ramp (β = 10 K min^{-1} in given case). Onsets of reactions therefore appear at higher temperatures.
2. In present research, DSC is conducted simultaneously with TGA, therefore a hole is poked in the sample pan to let any gaseous substance evolved leave. On the other hand, ARC sample holders are hermetically closed so that no substance escapes. This

is verified by weighing the filled sample holder before and after the experiment.

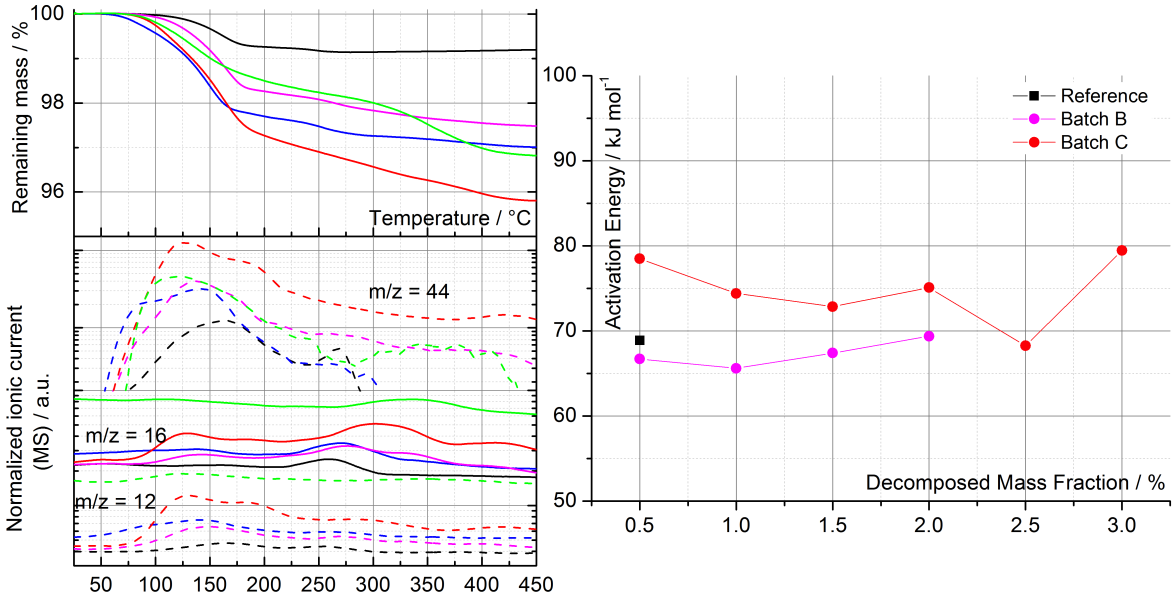

Figure 4.8: TGA of electrolyte-soaked anodes and MS of evolved gases (left, $\beta = 5$ K min^{-1}). Arrhenius activation energy of anode decomposition reaction (see section 3.3.1)

Reference anode exhibits no exothermal reaction below 200°C. It is likely that the weak heat evolution caused by SEI decomposition is compensated by (endothermal) evaporation of formed products and the electrolyte solvent. Aged cells do show exothermal behaviour below 200°C:

- Baseline curve is raised for anodes from cells C and D at 90°C and 80°C, respectively. This indicates an increase in heat capacity [88].
- First peak is observed at 186°C for batch A, 192°C for batch B, and 200°C for batches C and D. Sequence is in good agreement with ARC results.

Above 210°C (dotted line), an exothermal process of higher magnitude occurs. This large double peak is a result of reaction of intercalated lithium with electrolyte, and later with the binder [61]. Figure 4.8 shows TGA of anodes and mass spectra of evolved gases, as well as calculated Arrhenius activation energy from TGA curves. Fastest mass decline due to decomposition and evaporation is detected below 180°C. Analysis of evolved gases thereby indicates release of CO_2. Intensity of m/z=44 peak is higher for aged anodes, particularly from batch C, which also sees largest mass loss in total.

Mechanisms of anode-electrolyte reactions at elevated temperatures have been extensively discussed in literature. Exothermal reaction of SEI begins around 100°C when $LiPF_6$-based electrolytes are used [30]. Two distinct phenomena are believed to be part of SEI reaction between 100°C and 200°C, both occurring as a consequence of SEI thermal breakdown.

Secondary SEI formation: When due to SEI breakdown Li-intercalated graphite is exposed to electrolyte, the latter will be reduced in reaction with lithium. A fresh secondary SEI layer is thereby formed [89], passivating the surface again [90]. Given sufficient exposure, this process occurs at temperatures as low as 60°C and results in consumption of cyclable lithium that happens to be intercalated in graphite [91].

Decomposition of SEI to stable inorganic compounds: Molecules forming the SEI itself decompose into a various range of products [23]. Research by Richard and Dahn [30] suggest formation of Li_2CO_3 as main product of SEI decomposition. A layer of inorganic, non-conductive Li_2CO_3 would thus have been formed on surface of graphite particles. This layer would not act as SEI in usual sense, it would nevertheless passivate the surface, on which a fresh meta-stable SEI can be formed. For decomposition of lithiated organic molecules in SEI, following reaction is proposed:

$$(CH_2OCO_2Li)_2 \rightarrow Li_2CO_3 + C_2H_4 + CO_2 + \frac{1}{2}O_2 \tag{4.5}$$

SEI molecules may also react with intercalated lithium:

$$2Li + (CH_2OCO_2Li)_2 \rightarrow 2Li_2CO_3 + C_2H_4 \tag{4.6}$$

It is reasonable to assume that formation of meta-stable Li-organic compounds occurs at lower temperatures, while at higher temperatures, formation of Li_2CO_3 may be thermodynamically favoured. In addition, Yamaki et al. [92] have shown on the example of natural graphite that exothermal reaction detected by DSC at around 140°C is related to formation of primary SEI on graphite surface that has been covered by PVDF binder. This phenomenon is however observed in DSC analyses of freshly prepared anodes after three cycles. Upon ageing, PVDF is swelled by electrolyte and SEI is formed on these covered surfaces as well. Anodes investigated in present work do not exhibit aforementioned behaviour, since even the reference cell anode shows no peak attributable to primary SEI formation. It is reasonable to assume that PVDF was fully soaked by the time when cells were opened.

4.2.1.2 Cathode

Figure 4.9 shows ARC profiles (left) of electrolyte-soaked cathodes and DSC curves (right) of washed and dried cathodes. Figure 4.10 shows TGA curves and MS for evolved gases of washed, dried cathodes (left) and calculated Arrhenius activation energy from TGA curves (right).

During the adiabatic decomposition of cathode-electrolyte system (ARC), no significant increases in SHR are detected below 200°C. This temperature also corresponds to decomposition onset of most dried cathodes (except batch D) during DSC analysis. Between 200°C and 300°C, only cathodes from fresh (reference) and mildly aged (Batch A) cell show peaks above

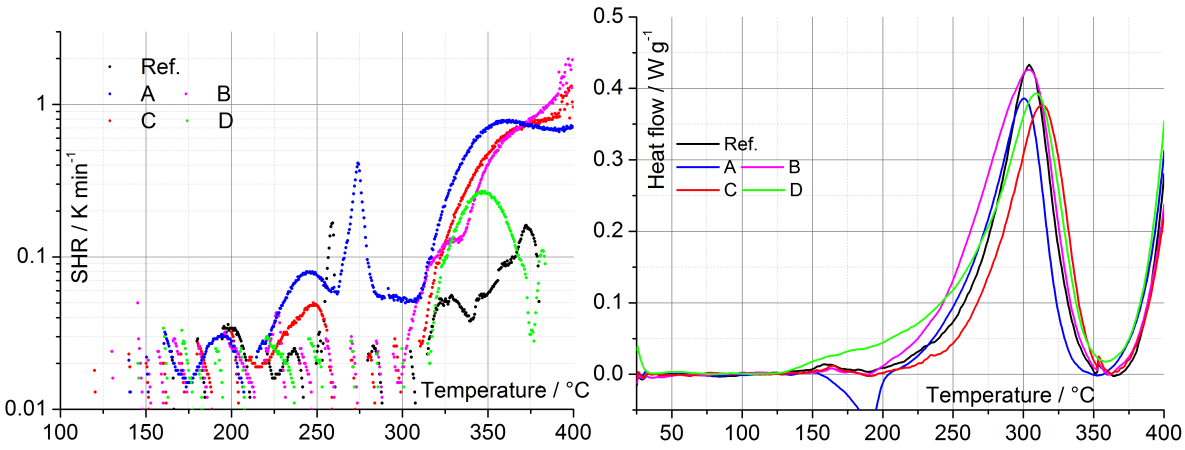

Figure 4.9: ARC thermal runaway profiles of electrolyte-soaked cathodes (left). DSC curves of washed and dried cathodes (right, $\beta = 10$ K min^{-1})

0.1 $K\ min^{-1}$. Heating rate is steeply increased in all cathodes above 300°C. This is likely a consequence of reaction between released O_2 - decomposition of dried cathode peaks at 300°C - and electrolyte. Increased total pressure and partial pressure of O_2 allow the reaction to occur below autoignition temperature of electrolyte ($\sim$ 450°C). Possible catalytic effect of transition metals on cathode surface cannot be excluded either.

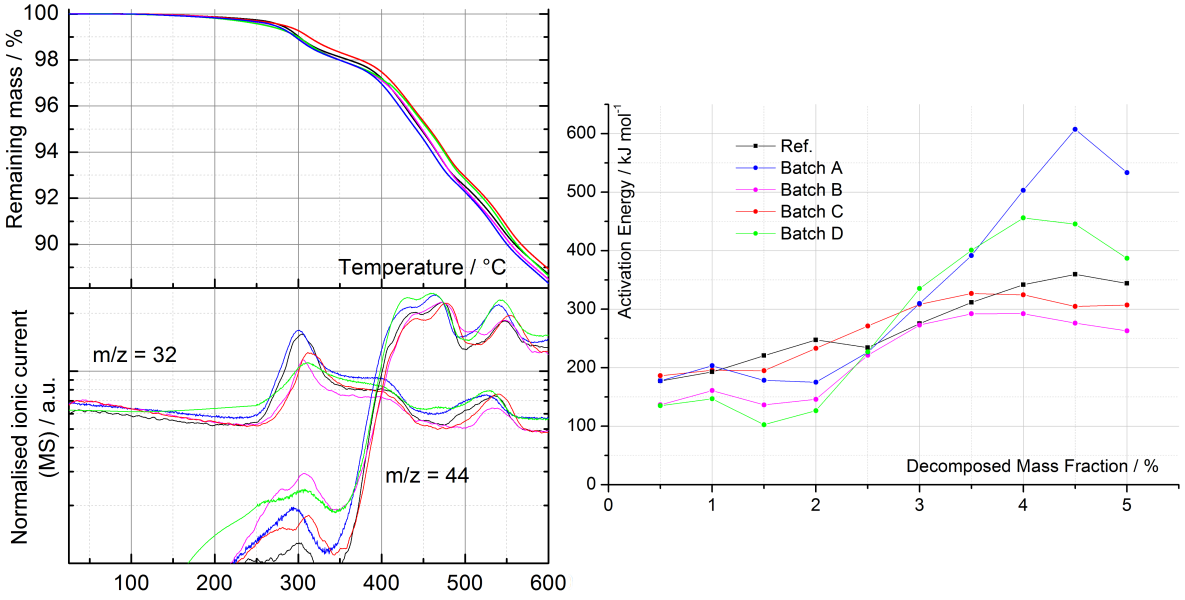

Figure 4.10: TGA of washed and dried cathodes and MS of evolved gases (left, $\beta = 5\ K\ min^{-1}$). Arrhenius activation energy of cathode decomposition reaction (see section 3.3.1)

TGA curves of dried cathode decomposition appear to be tightly overlapping, with exception of batch C, which exhibits slightly less steep profile during NCM decomposition between 250°C and 350°C. Batch D cathode stands out by early gradual increase in DSC heat flow above 150°C. Similar phenomenon is observed by mass spectra of the same cathodes, with O_2

and CO_2 emission peaks increasing above 150°C. Two stages of cathode thermal reaction are evident from Figure 4.10. Below 350°C, decomposition of active material occurs, resulting in significant emission of O_2. This corresponds to mass loss up to 2%. Above 350°C, reactions between active material and additives, as well as binder decomposition, take place. This reactions yield higher amounts of CO_2, while O_2-related signal decreases.

In case of fresh (reference) cathode, almost no CO_2 emission is observed by MS in the first stage of reaction. This is not the case for cathodes from aged cells. Especially cathodes from severly aged batches B, C, and D exhibit lower intensity of O_2-related signal (m/z=32). On the other hand, these cathodes yield higher CO_2-related signals (m/z=44) in the first stage of reaction. This is particularly evident for cathodes from batches B and D. Initial decomposition of these two cathodes is characterised by comparatively lower Arrhenius activation energies (Figure 4.10, right). There seems to be a parallel or competitive reaction in the aged cathodes below 350°C. It is the calculated activation energies that underline the argument in favour of parallel or competitive reactions. Namely, if CO_2 was formed by a consecutive oxidation/combustion of additives with gaseous O_2 from active material decomposition, the activation energy of overall process below 350°C would not be reduced: NCM decomposition would remain the rate limiting step in terms of chemical kinetics. No differences are found in crystal structure between different batches of decomposed cathodes (see Appendix A.2).

4.2.2 Thermal stability and safety of cells

Figure 4.11 shows ARC exotherm profiles of fully-charged cells. Aged cells exhibit considerably reduced thermal stability. Onset of a self-sustaining and accelerating exothermal reaction in aged cells is found at 75°C. On the other hand, two weak reactions with decreasing rate are observed, starting at 90°C and 100°C, in case of a reference fresh cell. Reference cell is suddenly cooled by about 10 K once it reaches 135°C, most likely due to melting of polyethylene in the separator. Cells from batches A and B undergo a similar phenomenon at slightly higher temperature ($\sim$ 150°C).

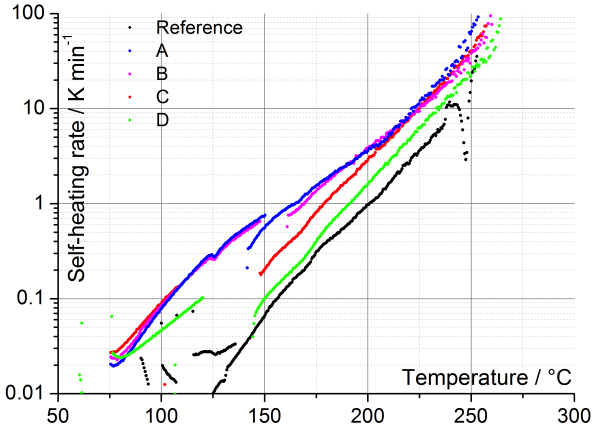

Figure 4.11: Thermal runaway profiles of fully charged cells in ARC

Notably, the initial rate of SHR increase for the cell of batch D is more gradual compared to other aged cells. This coincides with the lowest number of cycles among aged cells, and thereby quantitatively less SEI molecules that decompose exothermally. Cells from batches C and D quit self heating at 108°C and 120°C, respectively. This cannot be explained by melting of the separator. It is more likely caused by a different side reaction, or simply by the end of SEI decomposition.

As stated previously in this chapter, the calorimeter re-enters the HWS mode after the SHR drops below 0.01 $K\ min^{-1}$. Afterwards, self-heating is resumed in all cells and the separator's second melting stage (polypropylene at 160°C $\sim$ 170°C) does not abort the self-heating processes. Above 160°C, the cells' SHR at a given temperature is increasing with the number of cycles (Ref. $\rightarrow$ D $\rightarrow$ C $\rightarrow$ A and B). This is consistent with the trend observed from anodes' ARC in Figure 4.7, where the anodes with higher cycle number increase their SHR at consistently lower temperatures. Anodes' thermal behaviour therefore predominantly determines thermal stability of the entire cell. This finding is in line with the results of Inoue et al. [93], who have compared roles of individual electrodes in thermal runaway of NCM|graphite and NCA|graphite cells. Namely, NCM thermally decomposes at higher temperature compared to NCA. This means that oxidation of solvents and the anode by the released oxygen occurs later in the process, and therefore exothermal processes in the anode (as discussed in section 4.2.1.1) control the overall thermal behavior.

While the present work conveniently refers to entire phenomenon of cell's self-heating as "thermal runaway", some technical sources divide the process into three distinct stages. A review by Doughty and Roth [94] (Fig. 3 at p. 38) graphically distinguishes between onset, acceleration, and runaway phases. Among the cells presented in Figure 4.11, only the fresh cell follows such pattern. Highly cycled cells of batches A and B appear to exhibit SHR exponentially increasing with temperature in a continuous manner. This is attributed to previously discussed ageing phenomena of SEI growth and implies that aged cells enter terminal phase of runaway soon after the onset.

4.2.2.1 Mechanical safety properties

Figure 4.12 shows imposed load, cell voltage, and temperature during blunt nail indentation test as described in section 3.5. Aged cells exhibit a higher modulus (i.e. slope in the load vs. displacement plot), which indicates that these cells are stiffer than fresh cell. Impact of cycle ageing on electrodes' and separator's mechanical properties was investigated thoroughly by Wu et al. [95] on an example of NCM|graphite pouch cell (40 Ah). They executed both compression and indentation experiments. During compression, a lower modulus was reported for aged anodes and cathodes. A higher modulus for aged cells shown here in Figure 4.12 therefore implies an increase in internal pressure, caused by material expansion or gas formation during ageing. Modulus for the cell of batch D is nevertheless slightly lower

compared to B and C. This somehow co-relates with lower slope of SHR increase for batch D cell (cf. Figure 4.11 in the previous section), and may indicate that comparatively lower number of cycles contribute to less pressure build-up.

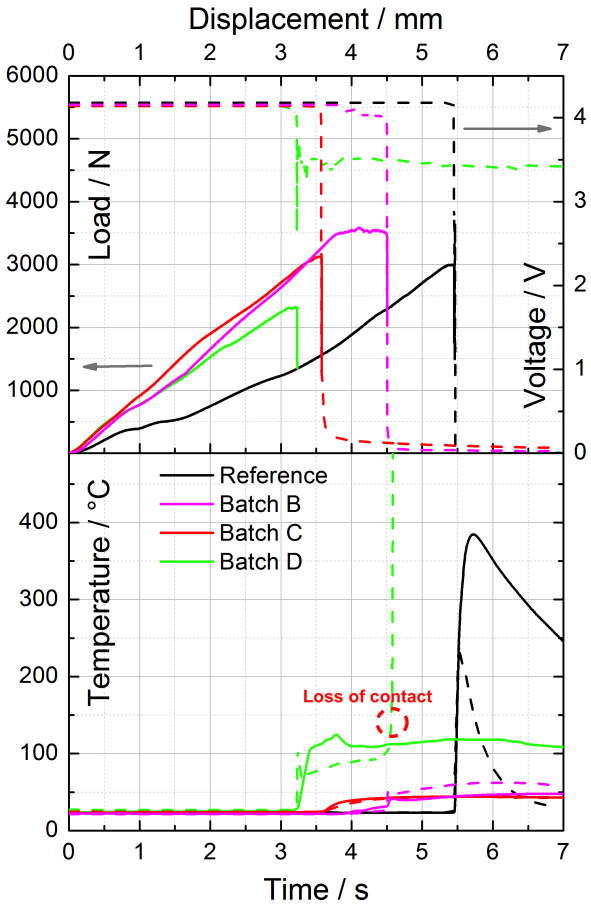

Figure 4.12: Results of blunt nail indentation test. In lower graph, full line represents nail temperature, and dashed line cell surface temperature.

Reference cell withstands a load of 3000 N and its thermal runaway is induced at largest displacement compared to other cells (5.5 mm is equivalent to 30% of cell's diameter). Nevertheless, thermal profile of the same cell shows sharpest increase in temperature. This is in line with results of cathode TGA-MS (Figure 4.10). Higher amounts of oxygen released from charged cathode active material, accompanied by less CO_2 formed by side reactions, creates a more explosive mixture of reactants, since the partial pressure of oxygen inside the cell in the moment of short circuit is higher compared to aged cells.

Cell from batch B reaches the highest load at 3500 N. Upon reaching this maximum, it remains constant for another millimetre of extra displacement while voltage drops slightly. Batch C cell withstands a load similar to that of the reference cell (3000 N), however at 2 mm lesser displacement. Cells from batches B and C share a similarly high modulus, as well as a notably mild temperature increase following the cell breakdown. On the other hand, cell from batch D (300 cycles) only withstands a load of approximately 2300 N and exhibits slightly lower

modulus than other aged cells. Notably, this cell also shows lower voltage drop than other cells. The voltage is stabilised at approximately 3.5 V for the remaining of the indentation experiment. Temperature rises above 100°C and remains constant, indicating a self-sustaining chemical reaction. Due to shortage of aged cells, the experiment could not be repeated on batch D cell to reproduce the results. It is therefore not possible to rule out that reported uncommon behaviour of cell under test occurred by chance.

5 Microstructure and Thermal Stability of Electrodes

5.1 Layered oxide cathode particle size and thermal stability

5.1.1 Material overview

Table 5.1: Overview of available $LiCoO_2$ materials.

Sample	**Type**	a_s/m^2g^{-1}	**Sample**	**Type**	a_s/m^2g^{-1}
LCOar	as-received	0.4	LCOm1	milled (500 rpm, 1 h)	4.6
LCOs1	sol-gel (800°C, 4 h)	0.47	LCOm2	milled (500 rpm, 2 h)	14.4
LCOs2	sol-gel (800°C, 2 h)	0.75	LCOm3	milled (500 rpm, 3 h)	16.0
LCOs3	sol-gel (700°C, 4 h)	1.15	LCOm5	milled (500 rpm, 5 h)	18.3
LCOs4	sol-gel (600°C, 8 h)	2.33	LCOm7	milled (750 rpm, 7 h)	42.4

Table 5.1 shows overview of as-received, ball milled, and synthesised $LiCoO_2$ samples. Only commercial LCO received from ENAX (LCOar) was used to produce milled samples reported here. Milling results in wider range of surface area. Achieving smaller particle size / higher surface area via synthesis path is hardly feasible due to phase purity issues. Namely, at lower temperatures and shorter dwelling time of annealing process, thermodynamic conditions favour formation of spinel structured (Fd-3m) LCO with inferior electrochemical activity.

Figure 5.1 shows selected SEM images of milled $LiCoO_2$ materials listed in the right-hand side of Table 5.1. Particles obtained by ball milling are irregularly shaped and considerably smaller. Size distribution is visibly inhomogeneous with some nano-sized particles. Based on this observations, it is not possible to completely exclude certain level of surface damage caused by ball milling. While the particles of milled batches still consist of layered R-3m phase, surface damage is manifested by considerable irreversible capacity in first cycle [67].

Figure 5.2 shows SEM images and Raman spectra of sol-gel synthesized $LiCoO_2$. Powders consist of particles similar to as-received LCO by shape. Primary sub-micron particles form agglomerates measuring few micrometres. Raman spectra indicate presence of spinel (Fd-3m) crystal structure in samples annealed at the lower temperature of 600°C. Nevertheless, layered R-3m phase is still dominant in LCOs4 sample, while being the only structure present in other synthesized samples. Two Raman bands, assigned to modes A_{1g} (597 cm^{-1}) and E_g (478 cm^{-1}),

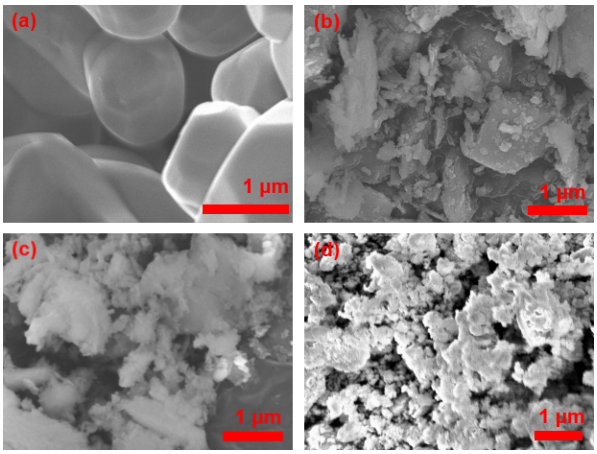

Figure 5.1: As-received (a) and subsequently milled $LiCoO_2$ (b - LCOm3, c - LCOm5, d - LCOm7 [67]

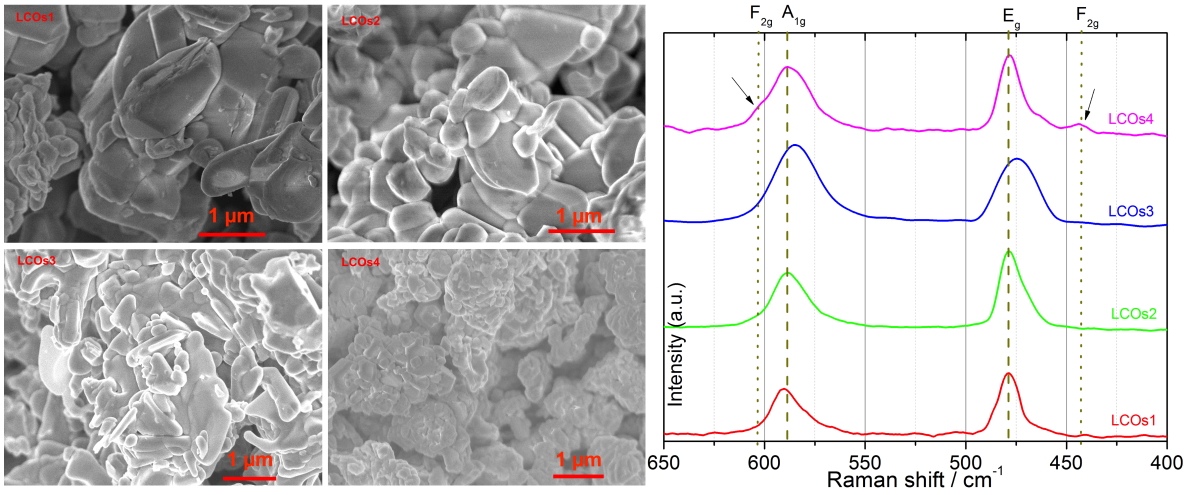

Figure 5.2: Sol-gel synthesized $LiCoO_2$: SEM images (left) and Raman spectra (right, [98])

indicate layered structure [96]. Two bands assigned to mode F_{2g}, indicating presence of spinel Fd-3m [97], are observable in LCOs4 sample at shift values of 605 and 449 cm^{-1}.

5.1.2 Thermal stability of $LiCoO_2$ cathodes

All investigated samples were charged to cumulative capacity of 136.9 mAh g^{-1} in second cycle, which is equivalent to $Li_{0.5}CoO_2$. Figure 5.3 shows TGA curves for decomposition under inert (Ar) atmosphere. Two phenomena are clearly observable:

- Cathodes with higher surface area active materials are thermally less stable, as the onset of decomposition reaction is lowered.
- With increasing surface area, mass loss due to thermal decomposition increases significantly.

For as-received LCO and synthesised LCO annealed at 800°C, mass loss at 400°C is about 5%, which is consistent with theoretical mass loss according to equation (5.1) [25, 26], considering 80% mass fraction of active material in cathode.

$$Li_{1-x}CoO_2 \rightarrow (1-x)LiCoO_2 + \frac{x}{3}Co_3O_4 + \frac{x}{3}O_2 \tag{5.1}$$

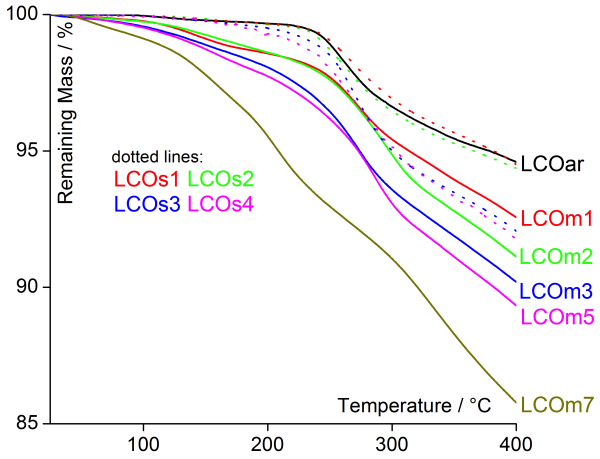

Figure 5.3: TGA profiles of $Li_{0.5}CoO_2$ charged electrodes under heating rate of 5 K min^{-1}

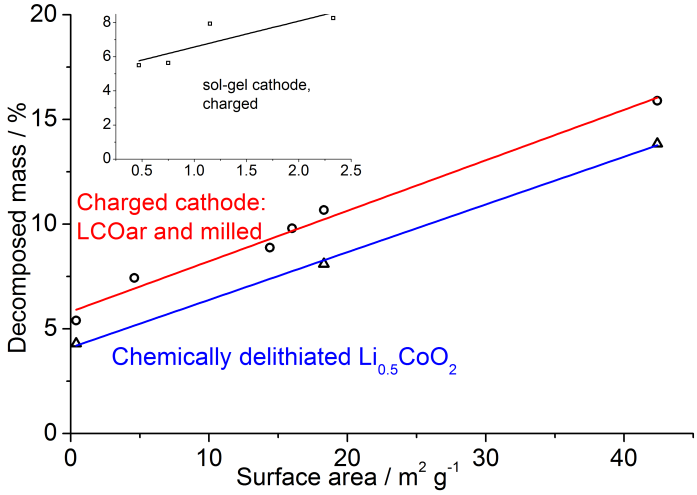

Figure 5.4: Decomposed mass fraction at 400°C for charged cathodes and chemically de-lithiated $Li_{0.5}CoO_2$ [67]

Figure 5.4 shows relation between decomposed mass and active material surface area for milled samples. As-received LCOar and its milled derivatives exhibit almost perfect linear relation between mass loss at 400°C and surface area of LCO for both electrochemically charged cathodes and $Li_{0.5}CoO_2$ prepared by chemical de-lithiation (See section 3.6.3). This implies that the cause of increasing mass loss lies in active material decomposition reaction

Table 5.2: First peak area of DSC curves for synthesised LCO from Figure 5.5, $[J\ g^{-1}]$

LCOs1	LCOs2	LCOs3	LCOs4
89	100	136	109

mechanism. The role of LCO and additives in decomposition of charged cathodes is further elaborated in section 5.1.3. In case of synthesized LCO, rising trend is observed as well, yet the data shows considerably less agreement with the linear model. Decomposed mass fraction is seemingly more correlated with annealing temperature of active material than with its surface area. This variable is missing in the milled LCO, since all batches were prepared by milling the same as-received LCO powder.

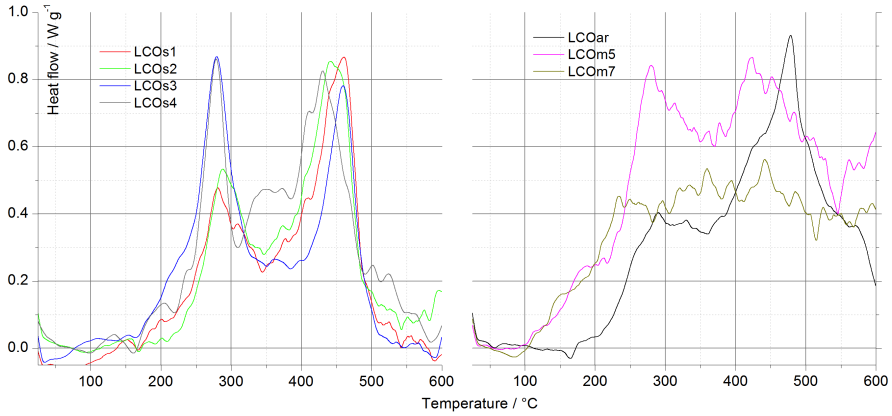

Figure 5.5: DSC curves of $Li_{0.5}CoO_2$ charged electrodes under heating rate of 10 K min^{-1}

Figure 5.5 shows DSC curves of charged LCO electrodes. First peak between 250°C and 300°C, which coincides with $Li_{0.5}CoO_2$ decomposition, is higher and larger by area for synthesized samples with smaller particles / higher surface area. Second peak above 400°C, related to decomposition of additives and their side reactions with decomposed active material, is in the same range of magnitude for all synthesized samples. Integrals of the first peaks are summarised in Table 5.2. Spinel phase containing LCOs4 exhibits another peak between the two major DSC peaks and a smaller first peak area compared to LCOs3, which can be attributed to higher thermal stability of spinel Fd-3m phase compare to layered R-3m structure. Milled materials show an early increase of exothermal DSC heat flow due to early onset of decomposition reactions, and less prominent peaks. The latter can be explained by slower mass loss during decomposition, which can also be observed as less steep, more gradual rate of mass loss in TGA curves in Figure 5.3. As-received LCO has lowest surface area of all samples and exhibits less prominent peak compared to synthesised materials.

Figure 5.6 shows MS signal for O_2 (m/z=32) and CO_2 (m/z=44) in the evolved gases during the TGA analysis. Signal intensity of detected O_2 decreases with increasing surface area for both synthesised and milled samples. On the other hand, initial peak of ionic current at m/z=44 (CO_2) is higher for smaller particles. There are three possible causes for these

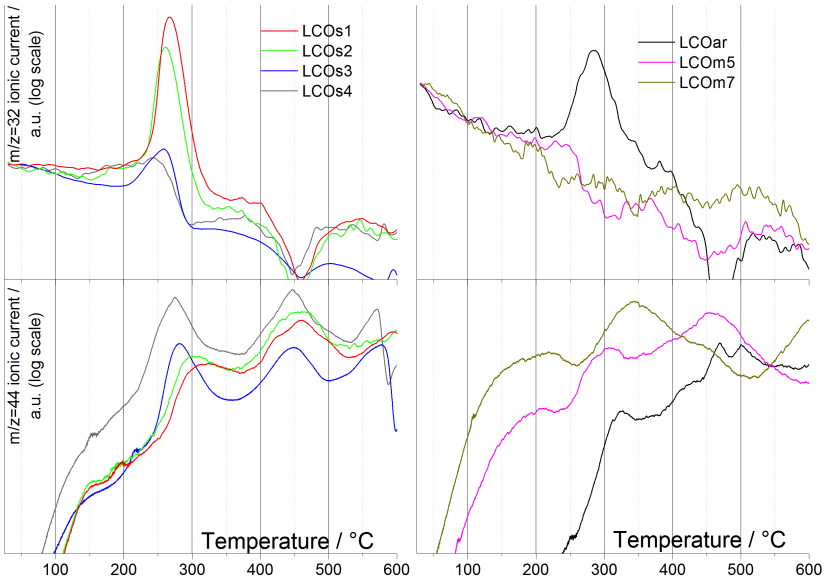

Figure 5.6: Evolved gases analysis (MS) during TGA of charged LCO cathodes

phenomena:

- Higher surface area catalyses side reactions between oxygen (either released as O_2 or structural O^{2-}) and additives, thus forming more CO_2
- Different reaction mechanism of decomposition on particle surface compared to bulk: more O_2 may be formed in bulk, also due to above mentioned side reactions on surface
- Due to earlier onset of reaction, particularly in milled samples, and subsequently slower decomposition at lower temperatures (less steep mass decline observed in TGA), O_2 generation rate is slower, and MS signal is overshadowed by baseline.

5.1.3 Role of active material and additives in thermal decomposition

To understand engagement of active material itself and both additives in decomposition reaction, TGA analyses were conducted on selected chemically de-lithiated materials to isolate the effect of additives. Figure 5.7 (left) compares TGA curves of chemically de-lithiated LCO itself (as-received and milled samples), with individual additives, and charged cathodes. All curves are normalised to mass of active material for comparability. Results of the component-segregated TGA analyses are summarised in Table 5.3. As-received chemically delithiated sample (LCOar, 0.4 m^2 g^{-1}) shows a total mass loss of 4.30% at 600°C, which is below the theoretical value according to equation (5.1). Mixing with acetylene black increases overall mass loss beyond 500°C. Mixing with PVDF shows a mass drop at 470°C, which corresponds to the decomposition temperature of PVDF. When the surface area is increased to 18.3 m^2 g^{-1} (LCOm5) and 42.4 m^2 g^{-1} (LCOm7), the corresponding mass losses for the chemically de-lithiated powder without additives are 8.10% and 13.84%, respectively. This is higher than

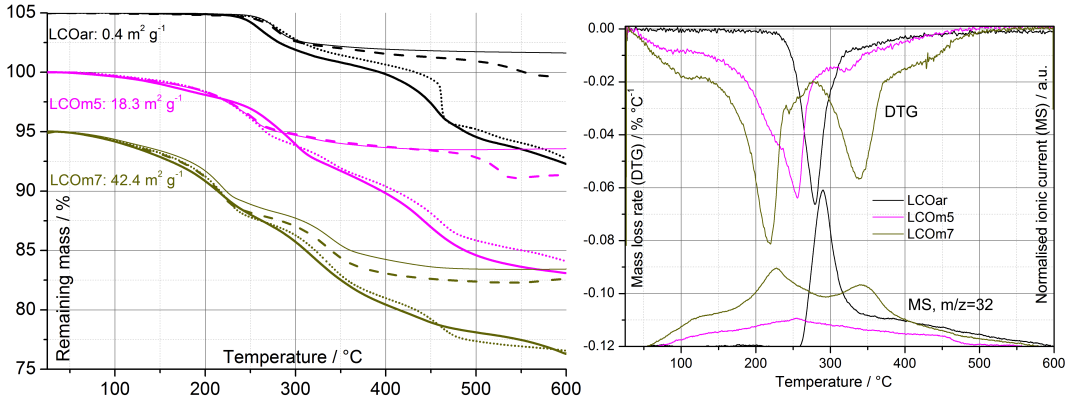

Figure 5.7: Left: TGA curves of chemically de-lithiated $Li_{0.5}CoO_2$: alone (thin lines), with acetylene black (dashed lines), with PVDF (dotted lines). Thick lines represent charged cathodes [67]. Right: First-order derivative (DTG) of TGA curves for pure $Li_{0.5}CoO_2$, and MS signal (m/z=32) related to same analysis

the theoretical maximum of 5.45 according to equation (5.1). Presence of acetylene black adds 2.90, 3.09 and 2.56 percentage points to mass loss for LCOar, LCOm5, and LCOm7, respectively. Presence of PVDF adds 11.97, 11.69 and 6.72 percentage points to mass loss for LCOar, LCOm5, and LCOm7, respectively.

Table 5.3: Mass losses (normalised to mass of LCO in respective samples) at 600°C [67]

Sample	Pure $Li_{0.5}CoO_2$	$Li_{0.5}CoO_2$ & acetylene black (8:1)	$Li_{0.5}CoO_2$ & PVDF (8:1)	Charged cathode (8:1:1)
LCOar	4.30%	7.20%	16.27%	15.9%
LCOm5	8.10%	11.19%	19.79%	21.14%
LCOm7	13.84%	16.4%	23.12%	23.39%

While amount of additives reacted in side reactions seems to vary among the LCO samples with different surface area no clear trend can be seen from the three observed samples. Higher surface area does not affect final conversion of side reactions between decomposing active material and additives. Amount of reacted/decomposed additives is more likely to depend on availability of O_2 in the temperature range of decomposition/combustion. The major part of the difference in mass loss between cathodes with different surface area comes from the active material itself. Mass loss of pure $Li_{0.5}CoO_2$ is almost doubled with increasing surface area by milling from 0.4 to 18.3 m^2 g^{-1} and more than tripled when surface area of LCO is increased to 42.4 m^2 g^{-1}. For chemically delithiated LCOm7 with highest surface area, two stages of mass loss can be observed, one before 250 C and one after. This is not the case for other two chemically delithiated samples.

Total amount of TGA weight loss from the cathode therefore comes from three contributions:

- mass loss from active material
- mass loss from carbon
- mass loss from binder.

The latter two contributions are not significantly affected by active material surface area. The most significant difference between various LiCoO2 samples comes from the active material. Right plot in Figure 5.7 shows first-order derivative of TGA curves for pure $Li_{0.5}CoO_2$, also known as differential thermogravimetry (DTG) curves, and evolved gas MS signal for peak m/z=32, assigned to O_2. Rate of mass loss, expressed by DTG curves, is increasing gradually with temperature for milled samples with high surface area. On the other hand, LCOar exhibits a swift rate increase above 240°C. Consequentially, oxygen generation rate also increases gradually and over a wider temperature range for milled samples compared to LCOar. Mass spectrometry results suggest a higher cumulative O_2 emission from high surface milled samples LCOm5 and LCOm7. Establishing any quantitative relationship between mass loss and MS is not practicable for one reason. Despite purging the TGA-DSC chamber with argon gas prior to analysis, there are residues of atmospheric gases (N_2, O_2) present. This causes the baseline signal for these gases to be slightly higher. Small increases of O_2 concentration are therefore not detected. Since the milled samples decompose and emit oxygen at slower rate (on average) and over a wider temperature range, more of the emitted O_2 goes undetected as compared to as-received sample. The latter decomposes in a relatively narrow temperature window.

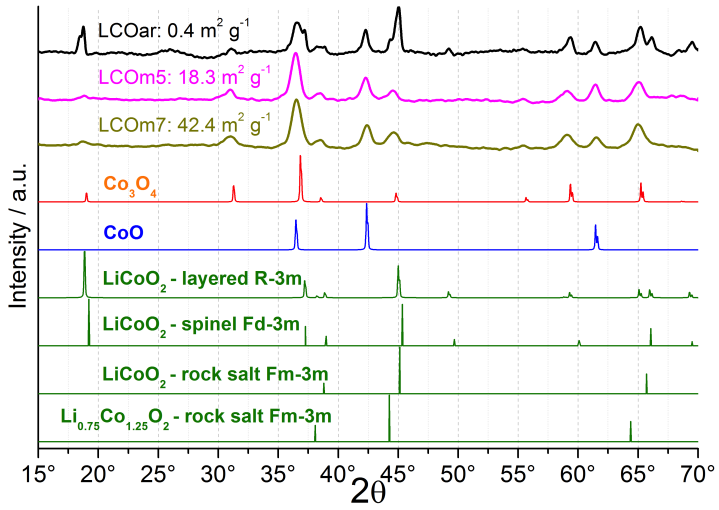

Figure 5.8: XRD spectra of decomposed cathodes (heated up to 600°C) compared to standards for $LiCoO_2$ (layered, spinel and rock salt), Co_3O_4 and CoO. Absence of R-3m $LiCoO_2$-related peaks is obvious for the two cathodes with higher surface area.

Above discussed findings imply a different decomposition reaction taking place for LCO with different surface area. In order to elucidate the reasons behind these phenomena, XRD

spectrum of cathode decomposition products after TGA was taken for the samples LCOar, LCOm5, and LCOm7. Figure 5.8 shows the XRD spectra for the decomposed cathodes (after being heated to 600°C in TGA). The as-received $Li_{0.5}CoO_2$ electrode after annealing shows peaks related to layered R-3m $LiCoO_2$, Co_3O_4 and CoO. This suggests a decomposition reaction according to equation (5.1). Peaks related to CoO indicate additional reduction of Co ions in presence of carbon, according to equation (5.2) below:

$$Co_3O_4 \; + \; \frac{1}{2}C \; \rightarrow \; 3CoO \; + \; \frac{1}{2}CO_2 \tag{5.2}$$

On the other hand, milled high-surface LCO electrodes do not decompose under the same mechanism. In particular, the peaks characteristic for layered (R-3m) LCO have very low intensity or are entirely absent. The tallest peak related to layered LCO around 19°(003) is almost completely absent, which indicates change in crystal structure. This suggests the formation of the Li-Co-O system with rock salt (Fm-3m) structure. In rock salt structure, Li and Co atoms are occupying the cation sites randomly [99]. Formation of rock salt structured $Li_yCo_{2-y}O_2$ ($0 \leqslant y \leqslant 1$) can explain the absence of (003) peak in the XRD spectra of high surface area cathodes after decomposition. Peaks of rock salt $Li_yCo_{2-y}O_2$ overlap with peaks of CoO, which also crystallizes in Fm-3m space group. Furthermore, changed ratio between atoms in rock salt Li-Co-O system explains partly the increased mass loss at decomposition. Assumed that rock salt $Li_yCo_{2-y}O_2$ with y = 0.8 completely replaced layered $LiCoO_2$ as decomposition product according to equation (5.1), the reaction equation changes to:

$$Li_{0.5}CoO_2 \; \rightarrow \; \frac{5}{8}Li_{0.8}Co_{1.2}O_2 \; + \; \frac{1}{12}Co_3O_4 \; + \; \frac{5}{24}O_2 \tag{5.3}$$

Theoretical mass loss according to equation (5.3) exceeds 7% (assuming decomposition of pure de-lithiated active material only). In case that CoO is also formed during decomposition, the mass loss can be even higher, up to 8.4%. Results of mass spectrometry (Figure 5.7, right) confirm the hypothesis of mass decrease due to increased oxygen emission. Assuming lower values of y in $Li_yCo_{2-y}O_2$ would further increase the theoretical mass loss. Nevertheless, presence of Co_3O_4 in XRD pattern of decomposition products ($2\theta = 31°$) implies that there is a stoichiometric limit at y = 0.66. Formation of Fm-3m $Li_yCo_{2-y}O_2$ with $y < 0.66$ would necessarily result in absence of Co_3O_4.

Linear relationship between surface area and mass loss (Figure 5.4) implies that there may be two different reactions occurring in the bulk and at the surface of LCO, where the surface reaction contributes to higher mass loss. If the surface of smaller particles is not stable, it releases more O_2 and the rock salt structure becomes a stable phase with oxygen deficiency on the surface. This may intuitively run against the findings for decomposition of cathodes with sol-gel synthesised LCO (upper left plot in Figure 5.6). Cathodes with sol-gel synthesised LCO seemingly emit less oxygen with increasing surface area. There are however 3 possible explanations for this apparent inconsistency:

1. Side reactions with additives: In case of cathode decomposition, lower emission of O_2 is observed for milled LCO active material as well (Figure 5.6, right). Given the excess of acetylene black and PVDF, considerable amounts of oxygen can be consumed to react. This is confirmed by increased first CO_2 peak (m/z=44) for LCOs3 and LCOs4 and by faster mass decrease for the same in the range from 250°C to 300°C (Figure 5.3).
2. Synthesised materials appear in lower range of surface area a_s. Their particle size is in the same order of magnitude as LCOar. It is possible that the proposed change in reaction mechanism takes place only for particles below certain size and formation of Fm-3m rock salt phase is not favoured for larger, more stable particles.
3. In case of LCOs4, annealed at 600°C, spinel phase $LiCoO_2$ is present, with different thermal properties.

Formation of rock salt phase may as well be related to structural/surface defects caused by ball milling. It was shown by Obrovac et al. [100] that during mechanochemical synthesis of LCO, rock salt phase is formed during prolonged milling. This should be, however, not the case in present work, since the presence of rock salt phase is not observed in any of the $LiCoO_2$ samples after milling [67]. Nevertheless, milling induced defects are not completely to exclude.

5.1.4 Kinetics of $Li_{0.5}CoO_2$ decomposition

Figure 5.9 shows apparent activation energy (E_a) as function of decomposed mass fraction (overall conversion) for selected cathodes. Calculation method is described in section 3.3.1. For sol-gel samples, initial activation energy of decomposition decreases with increasing active material particle size. Separately, the same is true for as-received LCO and its milled derivatives.

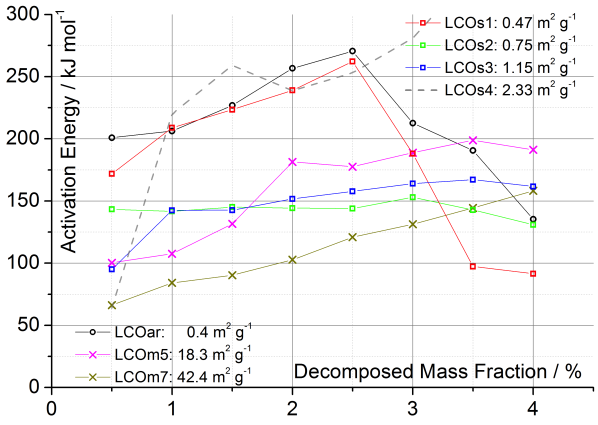

Figure 5.9: Calculated Arrhenius activation energy at different values of conversion for decomposition of charged LCO cathodes

As-received LCOar and synthesised LCOs1 with a_s in the same range, also show similar values of activation energy over the course of decomposition. Generally, activation energy decreases faster with growing surface area for synthesised LCO, compared to milled samples. For instance, LCOs3 (1.15 m^2 g^{-1}) and LCOm5 (18.3 m^2 g^{-1}) show same apparent activation energy at 0.5% total decomposed mass. Notably, cathodes with spinel structure containing LCOs4 (grey dashed line) exhibit steeply increasing E_a over the course of composition. This is likely related to spinel structure being thermally more stable in de-lithiated state [101].

The activation energy in most samples rises with conversion, which is attributed to lower concentration of active reactant, parts of which are converted to some type of lithium cobalt oxide, Co_3O_4 and O_2. Also, rising trend of activation energy versus conversion indicates occurrence of competitive reactions [84]. This can be related either to reaction (5.2) or to combustion and decomposition of additives. For LCOar and LCOs1 with the lowest surface area of 0.4 m^2 g^{-1}, activation energy reaches its maximum after approximately 2.5% of total mass is decomposed. This can be indicating the point where side reactions, such as oxidation or decomposition of additives, take over the dominant role in cathode decomposition reaction. High surface area (18.3 and 42.4 m^2 g^{-1}) milled LCO cathodes do not reach this turning point in the observed interval of conversion (up to 4% decomposed mass), since more of the active material decomposes before the side reactions become dominant. Synthesised LCO cathodes with slightly higher surface area (LCOs2, LCOs3) also do not exhibit prominent maximums.

It has to be emphasized that samples reach the same percentage of residual mass at different temperatures. In proposed the kinetic model (Arrhenius equation), E_a is however not temperature dependent. Low initial (at 0.5%) values of E_a are primarily observed in cathodes that exhibit slow mass decline in initial stage of decomposition, prior to main increase in mass decline rate (cf. Figure 5.3). This behaviour is observed in milled cathodes at temperatures as low as 50°C - 150°C, and in synthesised LCOs3 and LCOs4 at around 200°C. Where the reaction is reaching the arbitrary points at which E_a is calculated at slower rate, the decomposition process is thermodynamically controlled. Increase in temperature results in faster acceleration of the reaction in this case, hence lower apparent activation energy. In cathodes with larger particles and lower surface area, decomposition onset temperature is higher, and the rate increases immediately. This circumstances strongly favour formation of thermodynamically more stable product. Reaction kinetics - how fast can thermodynamically more stable products be formed? - becomes limiting factor. Temperature increase results in a less significant acceleration of reaction rate, which is reflected by higher activation energy.

Apparently lower kinetic barrier of decomposition reaction is in line with the hypothesis of rock salt formation (section 5.1.3). Rock salt $Li_yCo_{2-y}O_2$ is reported to be thermodynamically stable only for $0 \leqslant y \leqslant 0.4$ when synthesised by thermal annealing [102]. Higher values of y would yield a layered R-3m structure. If there are in fact different decomposition reactions occurring in bulk and on surface, and the latter tends to be less stable, the activation energy of the overall reaction of cathode decomposition is expected to be lower. In addition to the

hypothesis of different decomposition reactions in bulk and at surface (as elaborated in section 5.1.3), this explains how even at higher values of y (y > 0.66 as suggested previously), rock salt $Li_yCo_{2-y}O_2$ can be formed.

5.2 Safety aspects of novel over-lithiated oxide (OLO) cathode materials

5.2.1 General insight into thermal behaviour of over-lithiated cathode material

Overlithiated cathode material $0.4Li_2MnO_3{-}0.6Li[Ni_{1/3}Co_{1/3}Mn_{1/3}]O_2$ (labeled as OLOar, see section 3.1.1.1) was obtained from Samsung SDI and serves as starting platform for investigating thermal stability of this class of active materials. Figure 5.10 shows typical first cycle charge-discharge profile and second cycle charge profile. SEM images on the right side of the same image show microstructure of OLOar ($a_s = 3.42\ m^2g^{-1}$).

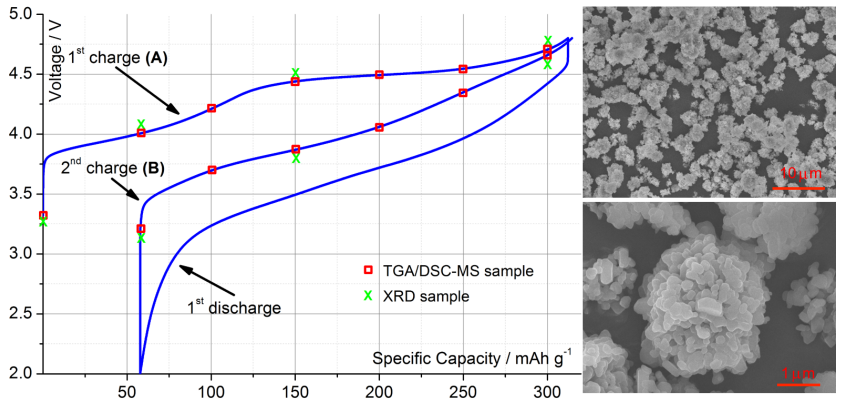

Figure 5.10: Left: Cycling profile of OLOar cathode vs. $Li|Li^+$ ($I = 25\ mA\ g^{-1}$). Squares and crosses indicate points at which washed and dried cathodes were analysed. Right: SEM images of OLOar under different magnifications.

Two distinct regions are observed in the first charge profile of OLO cathode:

- First region below CCV of 4.4 V corresponds to charge capacity of approximately 150 mAh per gram active material. This is equivalent to removal of 0.5 Li^+ per formula unit and is attributed to Li extraction from NCM component.
- Flat plateau at 4.5 V is attributed to activation of the LMO component.

First charge capacity equals 310 $mAh\ g^{-1}$. Subsequently, 255 $mAh\ g^{-1}$ are discharged, with an irreversible capacity of 55 $mAh\ g^{-1}$. Notably, electrodes with the same cumulative capacity (same amount of Li in the material) during the first and second charges have vastly different electrode potentials. This is due to the difference in the structure of the LMO-NCM material before and after LMO activation. Consider samples (1) and (2) at a cumulative capacity of 150 $mAh\ g^{-1}$ during the first charge and second charge (0.5 Li per formula unit removed),

as indicated in Figure 5.10. The potentials for the electrodes are 4.37 V and 3.28 V vs. Li|Li$^+$, respectively. Sample (1) has undergone first charging with Li removal only from the NCM component in the structure. Oxidation states of Ni, Co and Mn are 4+. Sample (2) has undergone LMO activation during first charge. Most of the charge/discharge capacity originates from oxidation state change of Mn below a potential of 3.8 V, and Ni and Co above 3.8 V. Sample (2) is therefore expected to have oxidation states of Ni and Co of close to 2+ and 3+, with a mixed oxidation state of Mn between 3+ and 4+. A comparison between the first and second cycles can therefore provide information on how the stability of cathodes is affected by the mechanism of LMO activation and the oxidation states of the transition metals in the material.

Figure 5.11 shows TGA (left) and DSC (right) curves of washed and dried OLO cathodes decomposition. Curves are shifted for clarity purpose. The pure OLOar powder does not

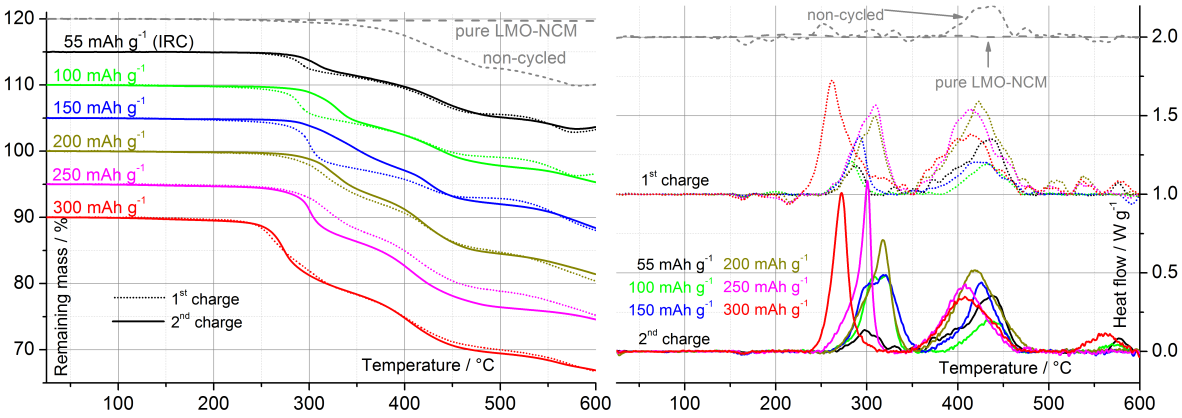

Figure 5.11: TGA (left) and DSC (right) curves of OLOar cathodes [72], $\beta = 5\ K\ min^{-1}$

decompose below 600°C. The blank electrode containing binder and carbon black decomposes above 350°C due to the decomposition of the PVDF binder and the reduction of active material in the presence of carbon. The charged electrodes show mass loss below 350°C, which is attributed to the reduced stability of the Li-deficient active material. As expected, total mass loss increases with state of charge and the degree of Li removal, indicating large amount of decomposition for material with lower Li content. For cathodes charged in the first cycle (dotted lines), decomposition onset temperature is found in a rather narrow range between 276°C and 296°C until 250 $mAh\ g^{-1}$, and decreases to 238°C at 300 $mAh\ g^{-1}$. The onset temperature is typically an indication of how stable is the material structure. Based on the charging mechanism of over-lithiated oxides, a change in material structure after the activation of the LMO component above 153.7 $mAh\ g^{-1}$ would be expected. However, the decrease in thermal stability (in terms of earlier decomposition onset) is only seen after 250 $mAh\ g^{-1}$, which is 100 $mAh\ g^{-1}$ above expected value. This is nevertheless in line with findings of Koga et al. [69, 70], who suggest the release of O_2 from the surface of particles takes place at the beginning of LMO activation, and the oxidation of oxygen from the bulk at higher charge capacity. The decrease in onset temperature at a later part of charging is

probably due to the formation of unstable oxidized oxygen in the material.

In corresponding DSC curves of the same cathodes during decomposition, the first exothermal peak is related to active material decomposition, and the second peak is related to decomposition of the binder and reduction of the active material by carbon black. The enthalpy (heat generated) of the active material decomposition is thus determined from the first peak. During the first charge cycle, enthalpy increases with increasing state of charge (see Table 5.4), which is reasonable because as more Li is extracted from the material, the energy released from cathode is expected to increase during the thermal test.

Table 5.4: Summarised TGA and DSC key data for decomposition of OLOar-based cathodes

Charge capacity / $mAh\ g^{-1}$	Onset temperature (TGA)		Enthalpy (DSC, 1st peak)	
	1st charge	2nd charge	1st charge	2nd charge
55	276°C	287°C	52 Jg^{-1}	52 Jg^{-1}
100	277°C	301°C	61 Jg^{-1}	220 Jg^{-1}
150	291°C	301°C	108 Jg^{-1}	274 Jg^{-1}
200	296°C	301°C	194 Jg^{-1}	264 Jg^{-1}
250	292°C	290°C	264 Jg^{-1}	252 Jg^{-1}
300	238°C	248°C	334 Jg^{-1}	259 Jg^{-1}

Thermal behaviour of cathodes charged in the second cycle differs significantly from those charged in first cycle. By comparing cathodes with equal amount of lithium per formula unit (same cumulative capacity or SOC), one observes higher onset temperature for decomposition of cathodes, charged in second cycle, below 200 $mAh\ g^{-1}$. The active material is thermally more stable after the second charge, despite equal amount of intercalated lithium. The reason for this is difference in oxidation states of the transition metals: These are higher for Ni and Co during the first charge compared to second charge after the LMO activation. Ni^{4+} and Co^{4+} are less stable at elevated temperatures and decompose easily. This is commonly known for ordinary layered (R-3m) structure cathode materials as well. After the cumulative capacity in second charge exceeds 200 $mAh\ g^{-1}$, the decomposition onset temperature is lowered. As discussed above, at the later part of second charge cycle, more of Ni and Co are oxidised to 4+ state, effectively lowering thermal stability of the material.

DSC curves of cathodes charged up to 200 $mAh\ g^{-1}$ in second cycle exhibit larger peaks compared to first cycle. This indicates higher enthalpy of decomposition, despite better thermal stability manifested by higher onset temperature. Structurally, there are two explanations for this phenomenon.

- During LMO activation (second plateau of first cycle charge curve), oxygen in the structure is oxidised. Part of it is released as O_2 from the surface in the initial phase of activation [68], and part of it is oxidised during structure densification in the later stage [69, 70]. This unstable oxygen is likely contributing the main share of heat release.

- During the first charge, oxidation state of Mn remains 4+, which is a stable form of manganese. Thus, no exothermal reactions involving Mn are expected in the initial phase of cathode decomposition. On the other hand, during the first discharge, some of the Mn is reduced to oxidation state 3+. Therefore, for cathodes charged in the second cycle, some heat is generated from the Mn^{3+} during thermal decomposition.

Figure 5.12 shows MS profiles for peaks m/z=32 and m/z=44, assigned to O_2 and CO_2, during thermal decomposition. Onset temperature of O_2 emission roughly corresponds to TGA decomposition onset. Quantitatively, more O_2 is seen to be emitted from cathodes at higher SOC, which is expected. In case of CO_2, the difference appears to be smaller.

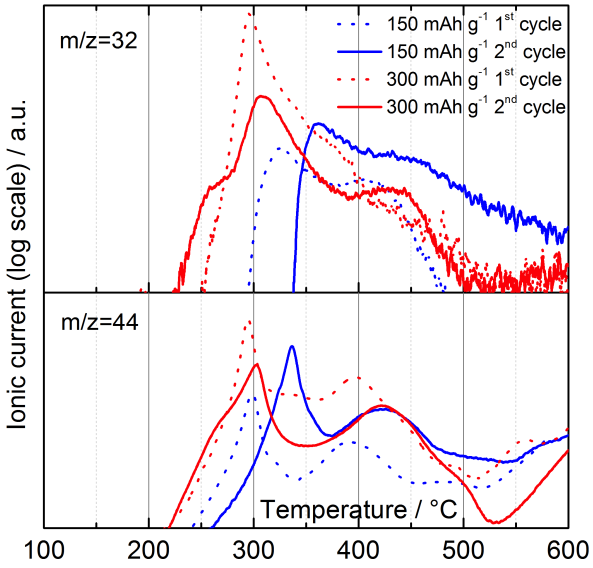

Figure 5.12: Mass spectrometry data related to evolution of O_2 and CO_2 during thermal decomposition

For cathodes charged to 150 $mAh\ g^{-1}$, higher amounts of both O_2 and CO_2 are emitted from samples charged in the second cycle. This is in line with the previously discussed idea of unstable oxygen affecting the decomposition. Cathodes charged in first cycle contain no unstable (oxidized) oxygen in the structure. Therefore, entire O_2 emission is related to oxidation of O^{2-} to gaseous O_2, offsetting the reduction of Ni^{4+} and Co^{4+} to more stable states. This is the same redox reaction mechanism one can observe in ordinary layered cathode materials, such as LCO and NCM. On the other hand, cathodes charged in the second cycle contain oxygen at higher oxidation states (O^{a-}, $-2 < a < -1$). Disproportionation of this unstable oxygen yields additional O_2 during thermal decomposition. Emission onset of CO_2 is observed at lower temperatures for the said cathodes, and is characterised by much smaller difference between first and second cycle cathodes. It is likely caused by reaction of material with carbon additive.

In case of fully charged cathodes (300 $mAh\ g^{-1}$), the m/z=32 (O_2) peak is more intense for first cycle charged cathode. Nevertheless, the peak for second cycle charged cathode has

slightly earlier onset and appears to be broader. Same observation can be made by comparing the DSC peaks (Figure 5.11, right) of the same samples. Both cathodes have undergone the LMO activation during the first charge. However, Mn is allegedly reduced to Mn^{3+} during discharge, along with some of the unstable oxygen. Subsequent oxidation to Mn^{4+} in the second charge step contributes to overall charge capacity. Therefore, less oxidised oxygen is present in the structure of second cycle cathodes at same cumulative capacity.

5.2.1.1 Analysis of decomposition products

XRD analyses were carried out before and after thermal decomposition on chosen cathodes, in order to understand the differences in extent of reaction and its products. Figure 5.13 shows XRD of different samples before (left) and after (right) thermal treatment in TGA/DSC system. Spectra of received OLOar powder, dried non-cycled cathode, cathodes charged to 55 $mAh\ g^{-1}$ (equivalent to first cycle irreversible capacity), 150 $mAh\ g^{-1}$ and 300 $mAh\ g^{-1}$ in both the first and second cycles were taken.

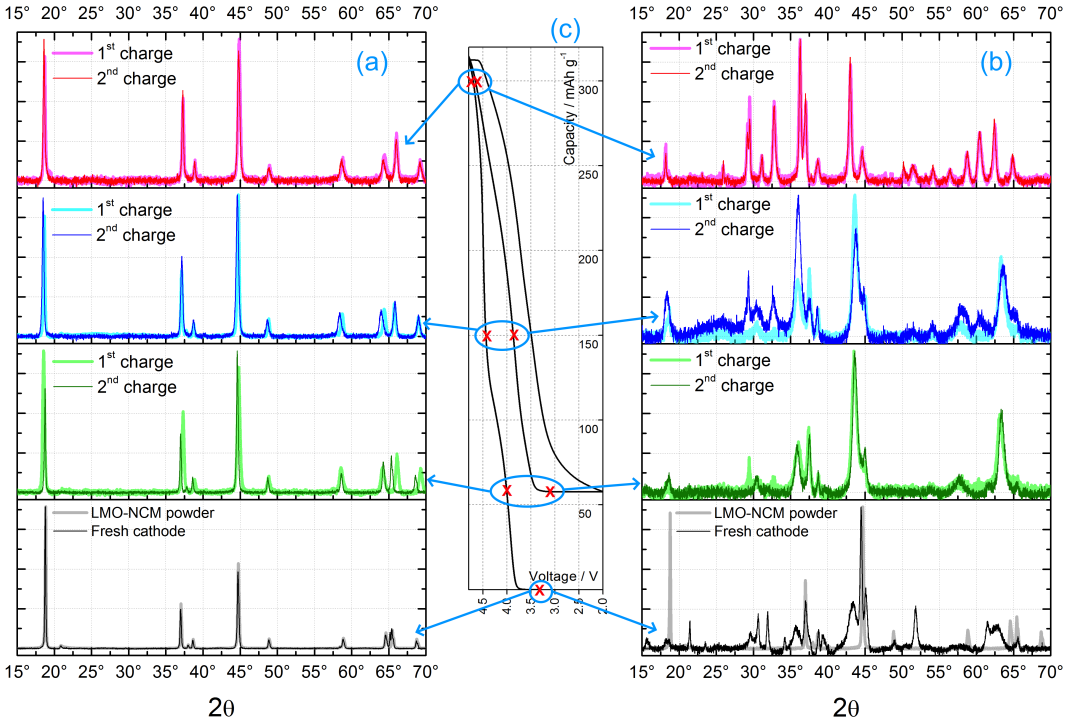

Figure 5.13: XRD of OLOar powder and cathodes before (a) and after (b) thermal decomposition in TGA/DSC at various states of charge in the first and second cycles as indicated in (c). All spectra are normalized to the highest peak intensity in the respective spectrum [72]

XRD spectra of cathodes at various states of charge before thermal decomposition (Figure 5.13, left) show changes in crystal structure during the first cycle and subsequent charge. Most notable is the decrease in relative intensity of the (003) peak between 18°and 19°during the first cycle and its consequent increase during the second charge. These changes reflect the

activation of the material, in particular its LMO component, and are extensively described in literature [69, 103].

XRD spectra of decomposed cathodes are shown on right side in Figure 5.13. The bottom plot shows the XRD profiles of the OLOar powder and the non-cycled electrode after being heated up to 600°C in inert atmosphere (TGA/DSC). While there is no significant change in the XRD pattern for the OLOar powder, the fresh electrode after thermal treatment exhibits completely different diffraction lines, due to reduction of the active material in the presence of carbon in the electrode. Most prominent phase in all spectra after thermal treatment is the Fm-3m rock salt structure in the form of oxides with characteristic peaks at approximately 37°, 43°, and 63°, which are most likely from the presence of CoO and NiO or $Li_{0.5}Mn_{0.5}O_2$ from the reduction of the transition metal. The spectra of the decomposed electrodes charged to 300 $mAh\ g^{-1}$ show additional peaks that most likely correspond to spinel Mn_3O_4 [104] and $LiMn_2O_4$.

The XRD patterns of the decomposed electrodes vary with state of charge, since the stable compounds after decomposition depend on Li content. Besides that, formation of decomposition products is also affected by oxidation states of the transition metals. This can be verified by comparing the XRD spectra of decomposed cathodes at the same state of charge in the first and second cycles. Spectra of decomposed fully charged cathodes at 300 $mAh\ g^{-1}$ show almost no difference between the first and second charges. The spectra of decomposed cathodes at the equivalent of irreversible capacity (55 $mAh\ g^{-1}$) also show almost no differences, except for the peak at 29.5° which may be related to β-MnO_2-like structure [105]. On the other hand, the spectra of decomposed cathodes at 150 $mAh\ g^{-1}$ during the first and second charges differ significantly, which is attributed to the difference in chemical environment of the two samples with the Li content is the same. The actual oxidation states of the transition metals in the materials charged to 150 $mAh\ g^{-1}$ during the first and second cycles are believed to be vastly different, based on previous studies [70]. In particular, the oxidation states of Ni, Co and Mn are expected to be close to 4+ for the electrode charged to 150 $mAh\ g^{-1}$ during the first cycle without the activation of the LMO component. For the cathode charged to 150 $mAh\ g^{-1}$ during the second cycle, the oxidation of Ni and Co are lower (probably between 2+ and 3+) whereas that of Mn is between 3+ and 4+. These lead to different reaction products after thermal decomposition. It is therefore reasonable that the onset temperature and the enthalpy of the thermal decomposition are different depending on the history of the electrode, as discussed above.

5.2.1.2 Thermal behaviour of OLO and long-term safety considerations

Electrochemical behaviour of over-lithiated oxide active materials is characterised by two-plateau voltage profile during first cycle charge as a consequence of Li_2MnO_3 (LMO) component activation. This has, as discussed within this section, certain consequences on material

thermal stability. These become apparent immediately after first charge-discharge cycle. Two phenomena are critical in distinguishing OLO from state-of-the-art layered oxides:

- Participation of oxide ions in electrochemical reaction, resulting in emission of gaseous O_2 and unstable oxidised oxygen (O^{a-}, -2 < a < -1)
- Different reaction in bulk and surface during LMO activation in first cycle charge, whereby O_2 is emitted from surface and O^{a-} is formed during bulk structure densification [69]

Overall, thermal stability of OLO in the initial cycles is affected by amount of Li (SOC), amount of unstable oxygen, and oxidation states of transition metals Ni, Co, Mn. Above findings are motivation for following next steps:

- Surface modification by polymer coating as strategy to improve thermal stability: a thin, nanoscopic coating on cell has been demonstrated previously [106] to protect the surface of NCM particle from adverse reactions with electrolyte at higher voltage.
- Synthesise OLO powders with various particle size / surface area: Different electrochemical reaction in bulk and at surface is believed to affect thermal stability even more than in case of layered oxides, such as LCO discussed in section 5.1.
- Investigate impact of cycling and related oxygen oxidation-reduction on thermal stability for all investigated materials: repeat charging-discharging of cathodes for 10 and 20 cycles

5.2.2 Polyimide coating of OLO as safety improvement strategy

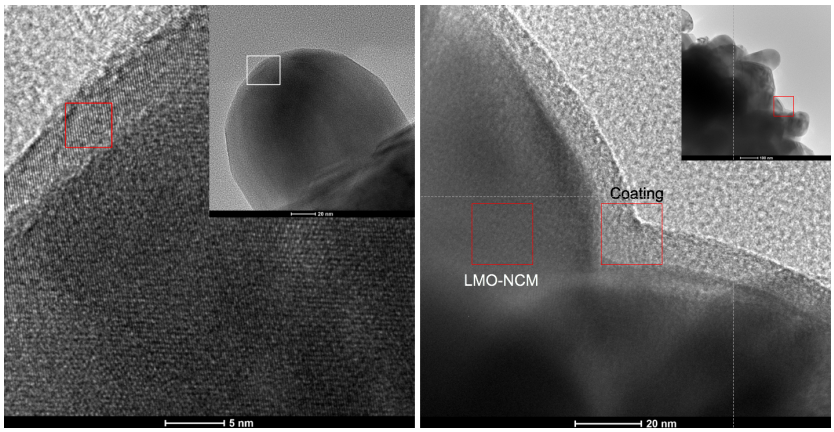

Figure 5.14: TEM images of as-received LMO-NCM (OLOar, left) and the same material coated with a polyimide layer (OLO-PI, right)

Result of coating procedure described in section 3.1.1.4 is seen on Figure 5.14. Polyimide coating is observed on surface of OLO particles. The coating is not completely uniform with its thickness ranging from 5 to 10 nm. Plane distance measurement by fast Fourier

transformation helps to distinguish amorphous coating (as seen on right side of Figure 5.14) from crystalline OLO structure. Polyimide coating increases BET surface area by almost 7% (from 3.64 to 3.89 $m^2 g^{-1}$).

Cycling profiles of cathodes with polyimide-coated OLO compared to as-received OLO are shown in Figure 5.15. In first charge cycle, a higher voltage profile is observed for polyimide-coated OLO-PI. This is likely due to increased charge transfer or polarization resistance through the coating layer. Such phenomena has been reported previously in the literature [106, 107] for non-composite polyimide coatings that do not contain conductive agent such as carbon. Consequentially, the characteristic transition between plateaus is slightly shifted towards lower SOC for polyimide-coated active material. During the first discharge, coated OLO-PI exhibits lower voltage plateau than the reference OLOar, which is also explained by increased resistance. However, both charge and discharge of the first cycle result in nearly equal capacities between OLOar and OLO-PI, indicating little to no difference in overall number of exchanged electrons. In the following 19 cycles, a visibly slower decline in capacity

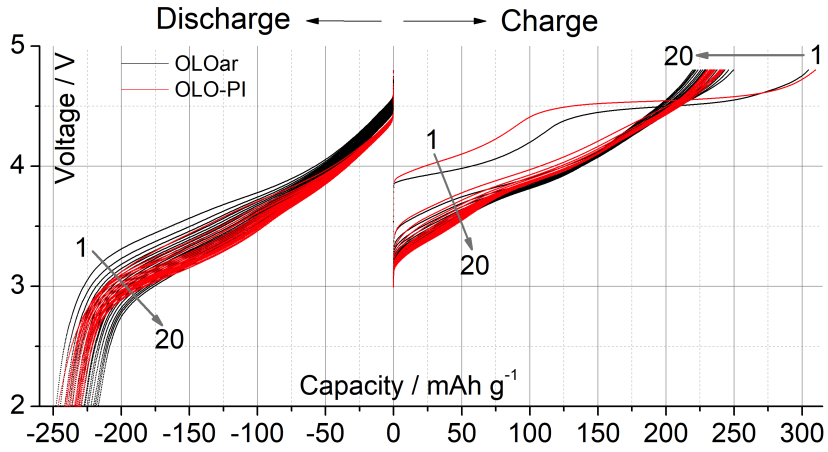

Figure 5.15: Charge and discharge voltage profiles for twenty cycles; OLOar and OLO-PI cathodes ($I = 25\ mA\ g^{-1}$)

is observed for coated OLO-PI. Deterioration of both charge and discharge voltage profiles during the course of cycling occurs for both OLOar and OLO-PI. This implies a decline of OCV as consequence of ageing. In case of discharge, it is evident that voltage declines at a slower rate for coated OLO-PI. In charge profiles, such difference is not observable in terms of voltage profile. On the other hand, the decline in charge capacity is slower in case of OLO-PI.

Figure 5.16 shows TGA and DSC curves of dried OLO-PI cathodes in first two cycles compared to OLOar curves under same conditions (cf. Figure 5.11 on page 60). Measured onset temperatures and reaction enthalpies of decomposition are summarized in Table 5.5. Coated cathodes charged to 300 $mAh\ g^{-1}$ in first and second cycle exhibit higher onset temperature and lower decomposition enthalpy compared to non-coated reference. This implies better thermal stability. However, for cathodes charged in first cycle, a narrower and taller DSC peak is observed for coated cathode. The exothermal heat flow reaches 1.4 $W\ g^{-1}$, double

compared to 0.7 $W\ g^{-1}$ for the equivalent OLOar cathode. In second cycle, peak heights for fully charged cathodes are equalized at approximately 1 $W\ g^{-1}$.

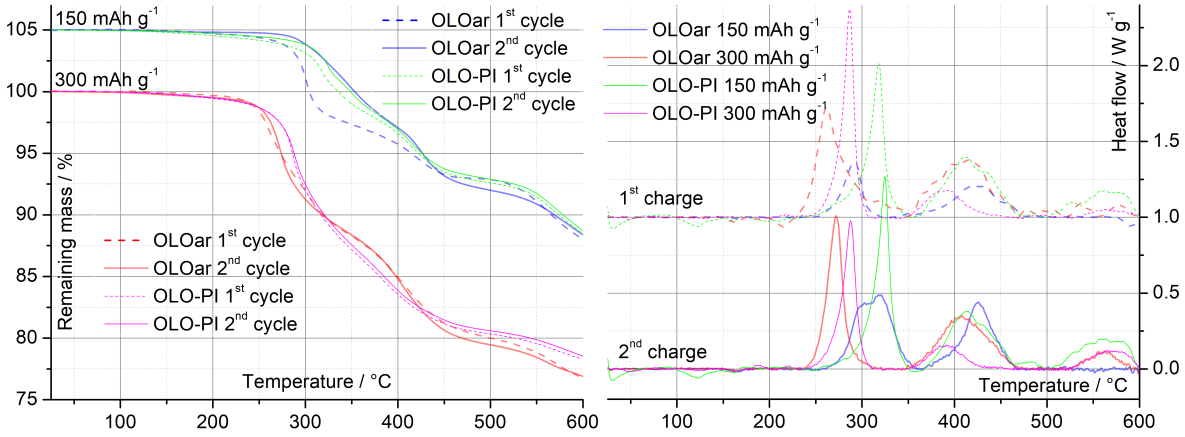

Figure 5.16: Comparison of TGA (left) and DSC (right) curves for OLOar and OLO-PI cathodes after first and second charge ($\beta = 5\ K\ min^{-1}$)

In case of cathodes charged to 150 $mAh\ g^{-1}$, the coated OLO-PI cathodes again exhibit slightly increased onset temperature. Additionally, two distinguishing features are observed in TGA-DSC curves of 150 $mAh\ g^{-1}$ cathodes:

- Decomposition enthalpies are significantly higher for OLO-PI cathodes. Also, difference between decomposition enthalpies of OLO-PI charged to 150 $mAh\ g^{-1}$ in first and in second cycle is negligible.
- The gap between TGA curves of first and second charge is reduced in case of OLO-PI, compared to OLOar. It appears that the TGA curve of first-charge 150 $mAh\ g^{-1}$ OLO-PI overlaps with both second-charge 150 $mAh\ g^{-1}$ curves.

Park et al. [108] have investigated impact of polyimide coating on thermal stability of $LiCoO_2$ by conducting DSC of the electrode-electrolyte system. They reported peak shifting towards higher temperature, which is in line with present results. On the other hand, they also report significant decrease in decomposition enthalpies for both coated samples, compared to reference LCO. In section 5.2.1, differences in thermal stability between OLOar cathodes charged to 150 $mAh\ g^{-1}$ in first and second cycle were explained by comparing oxidation states of transition metal ions. In theory, both OLOar and OLO-PI shall have their transition metals close to fully charged, i.e. 4+ oxidation state. However, the shift in charge curve transition (see Figure 5.15) indicates that the activation of the LMO component, and related oxidation of structural oxygen atoms may actually start at lower SOC. This implies an overlap of Ni, Co, and Mn oxidation with oxygen oxidation at SOC above 100 $mAh\ g^{-1}$. Confirming such phenomenon and investigating its causes goes beyond the scope of the present work. If this hypothesis is true, it means that OLO-PI at 150 $mAh\ g^{-1}$, compared to its OLOar equivalent, has:

- Transition metal atoms at comparatively lower oxidation state, leading to higher onset temperature of the decomposition.
- Some of O^{2-} in oxidized state. From the available results and reviewed literature it can not be concluded whether the polyimide coating hinders the release of gaseous O_2, or pushes the reaction towards formation of peroxide-like oxygen ions. Either species of oxidized oxygen would acts as oxidant during decomposition, which explains the increase of DSC-measured enthalpy.

It is assumed that for above stated reasons, OLO-PI charged to 150 $mAh\ g^{-1}$ in first cycle has structural similarities to readily "activated" cathodes in second cycle. Surface coating therefore affects activation process of over-lithiated oxide active materials.

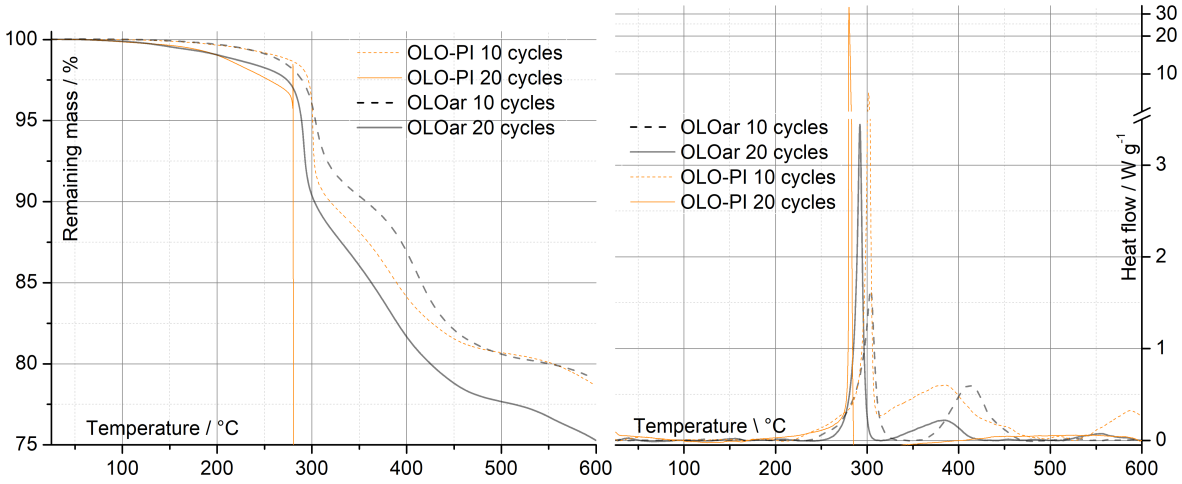

Figure 5.17: Comparison of TGA (left) and DSC (right) curves for OLOar and OLO-PI fully charged (4.8 V) cathodes after ten and twenty cycles ($\beta = 5\ K\ min^{-1}$)

Table 5.5: Comparison of TGA and DSC results for decomposition of OLOar and OLO-PI cathodes

State of charge	Onset temperature (TGA)		Enthalpy (DSC, 1st peak)	
	OLOar	OLO-PI	OLOar	OLO-PI
150 $mAh\ g^{-1}$ 1st charge	291°C	302°C	108 Jg^{-1}	320 Jg^{-1}
300 $mAh\ g^{-1}$ 1st charge	238°C	274°C	334 Jg^{-1}	273 Jg^{-1}
150 $mAh\ g^{-1}$ 2nd charge	301°C	309°C	274 Jg^{-1}	322 Jg^{-1}
300 $mAh\ g^{-1}$ 2nd charge	248°C	274°C	259 Jg^{-1}	227 Jg^{-1}
10 cycles, charged to 4.8 V	284°C	293°C	409 Jg^{-1}	622 Jg^{-1}
20 cycles, charged to 4.8 V	282°C	277°C	405 Jg^{-1}	n/a

Figure 5.17 shows TGA and DSC curves of dried fully charged (4.8 V) OLOar and OLO-PI cathodes after 10 and 20 cycles. Slow, gradual mass loss is observed in TGA curves even at lower temperatures: from 90°C for 20 cycles and from 150°C for 10 cycles cathodes. On the other hand, actual reaction onset temperatures are slightly higher than in first and second cycle. For OLOar, the onset temperature increases from 248°C at second full charge to 284°C

after 10 cycles and 282°C after 20 cycles. For OLO-PI, the onset temperature increases from 274°C at second full charge to 293°C after 10 cycles. However, after 20 cycles, the fully charged OLO-PI cathode undergoes a violent (possibly explosive) decomposition, resulting in a sudden mass loss at 277°C. This phenomenon was observed again in a repeated experiment in order to ensure reproducibility.

Continuous cycling, even at low current rate of 25 $mA\ g^{-1}$, greatly increases enthalpy of decomposition reaction, as well as peak heat flow. While the decomposition enthalpy declines from first to second full charge (from 334 to 259 $J\ g^{-1}$ in OLOar; 273 to 227 $J\ g^{-1}$ in OLO-PI), it increases significantly after ten cycles. In case of OLOar, it increases above 400 $J\ g^{-1}$ and remains in this range until 20th cycle. On the other hand, decomposition enthalpy of fully charge OLO-PI cathode after 10 cycles is more than 50% higher at 622 $J\ g^{-1}$. After the explosive decomposition of 20 cycles OLO-PI cathode, it is not feasible to calculate the enthalpy using the DSC data. Nevertheless, one may observe that after 20 cycles, DSC peaks for both types of cathode become narrower, with higher maximums, and slightly shifted toward lower temperature. This indicates faster reaction kinetics.

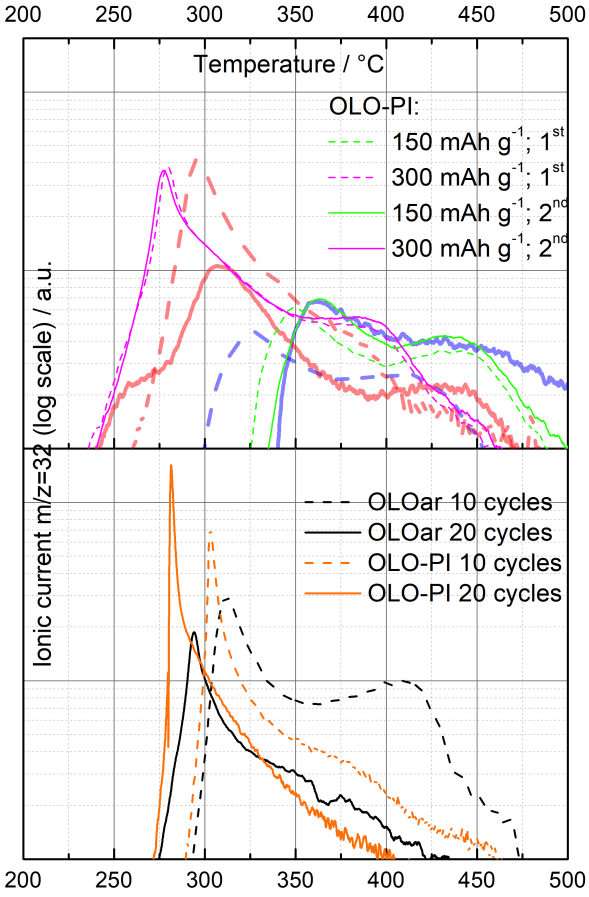

Figure 5.18: Mass spectrometry profiles related to evolution of O_2 ($m/z = 32$) during thermal decomposition of OLOar and OLO-PI cathodes. All cathodes at 10 and 20 cycles are charged to 4.8 V

Figure 5.18 shows MS profiles of evolved gas during TGA/DSC analysis for the peak at $m/z = 32$, equivalent to O_2. By comparing the profiles of cathodes charged to 150 $mAh\ g^{-1}$, following observations are made:

- OLO-PI and OLOar cathodes charged in second cycle exhibit almost identical O_2 emission profile during decomposition up to 450°C
- The O_2 emission profile of the OLO-PI cathode charged in first cycle is similar to second cycle sample, but shifted to lower temperature by about 10 K.
- In contrast to OLOar, OLO-PI exhibits more intense O_2 emission. This is in line with TGA/DSC experiments and supports the hypothesis that oxygen oxidation may occur at lower SOC during first charge due to coating.

Fully charged (300 $mAh\ g^{-1}$) OLO-PI cathodes in first and second cycle show almost overlapping $m/z = 32$ MS profiles. This is in profound contrast with fully charged OLOar cathodes. OLOar cathode charged in second cycle exhibits lower O_2 emission profile. Its peak is three times lower (note the logarithmic scale of MS signal in Figure 5.18) compared to first cycle. On the other hand, the emission profiles of both OLO-PI cathodes resemble the profile of first cycle fully charged OLOar, shifted by 20°C to lower temperature. The reduction in O_2 emission intensity in OLOar after second charge was attributed to less oxidized oxygen in the structure, due to activation of $Mn^{4+}|Mn^{3+}$ redox couple (see discussion on pages 62f.). This phenomenon seems to be absent in case of polyimide-coated OLO-PI cathodes charged in second cycle.

Onset of O_2 emission is shifted towards higher temperature for both OLOar and OLO-PI cathodes charged after 10 cycles. After 20 cycles, the onset temperature is slightly reduced again, but still remains above the onset temperatures of cathodes charged in first and second cycle. This corresponds to changes in TGA decomposition onset temperatures (Table 5.5). Differences between coated and reference cathodes are nonetheless observed when looking at the quantity of emitted O_2. OLOar cathodes exhibit lower MS profiles for the $m/z = 32$ as results of cyclic ageing, meaning that less O_2 is emitted during the decomposition of charged cathodes. The peak maximum $m/z = 32$ ionic current for OLOar cathode charged after 20 cycles is reduced by half compared to OLOar cathode charged after 10 cycles. On the other hand, the intensity of $m/z = 32$ ionic current increases significantly with increasing cycle number for OLO-PI cathodes.

Thermal behaviour of non-coated OLOar and polyimide-coated OLO-PI can be summarized in following points:

- Cycle ageing appears to stabilize the structure of LMO-NCM, which results in increased onset temperature of decomposition, both for pristine and coated samples. However, it also increases the enthalpy of decomposition reaction. This increase is considerably higher for the coated OLO-PI cathodes.

- While the polyimide coating does improve thermal stability of cathodes in first two cycles, thermal behaviour evidently deteriorates as consequence of cyclic ageing.

Following hypothesis is proposed to explain these phenomena: As observed during cycling of the investigated cathodes (cf. Figure 5.15), OLO-PI is losing its charge capacity, as well as its voltage plateau level, at considerably slower rate than OLOar. Reduced capacity loss has its causes in active material's structural changes. It implies that loss of oxygen and other structure-stabilizing phenomena occur to a decreased extent in polyimide-coated particles of the active material. This leads to formation of thermally less stable structure over several charge-discharge cycles, manifested in rapid decomposition reaction and high levels of O_2 emission.

It remains open to further investigations what role does the formation of a peroxide-like structure play. Recent research by Seo et al. [109] have found peroxide ion formation during the charge of ruthenium-containing overlithiated oxides. On the other hand, Luo et al. investigated ^{18}O-marked $Li_{1.2}[Ni_{0.13}Co_{0.13}Mn_{0.54}]O_2$ and found no true peroxide species present [110]. Instead, they propose the mechanism of localized electron holes formation on oxygen ions, coordinated by Li^+ and Mn^{4+} ions. This in turn invokes presence of thermally unstable oxidized O^{2-} species. It is reasonable to assume that either of the reversible oxygen oxidation mechanisms (peroxide or localized electron holes formation) negatively affect the thermal stability of the active material over the multiple charge-discharge cycles. Accumulated presence of such oxygen species would explain violent thermal decomposition of aged OLO-PI, accompanied by higher rate of oxygen release. On the other hand, irreversible O_2 emission during repeated charging of OLOar would lead to thermally more stable structure.

5.2.2.1 Comparison of decomposition products

XRD spectra of decomposed OLOar and OLO-PI cathodes are compared in Figure 5.19. Spectra for fully charged cathodes in first and second cycle (300 $mAh\ g^{-1}$) show only minor differences between OLOar and OLO-PI; few peaks in case of OLO-PI are shifted towards lower diffraction angle. On the other hand, two critical differences are observed in spectra of decomposed cathodes charged to 150 $mAh\ g^{-1}$:

1. The spectra of OLO-PI in first and second cycle are almost identical. This is in stark contrast with the spectra of decomposed OLOar, which differ significantly from first to second cycle (cf. Figure 5.13 on page 63). Discussion in the subsection 5.2.1.1 proposed different oxidation states of transition metals as explanation for differences in decomposition products. The activation of the LMO component by oxygen oxidation in the preceding cycle is the cause of different transition metal oxidation states.
2. Spectra of decomposed OLO-PI exhibit only three prominent peaks - those related to Fm-3m rock-salt structure (37°, 43°, 63°). Prevailing decomposition products are therefore limited to CoO, NiO, $Li_{0.5}Mn_{0.5}O_2$ and other compounds that crystallize in

Fm-3m lattice.

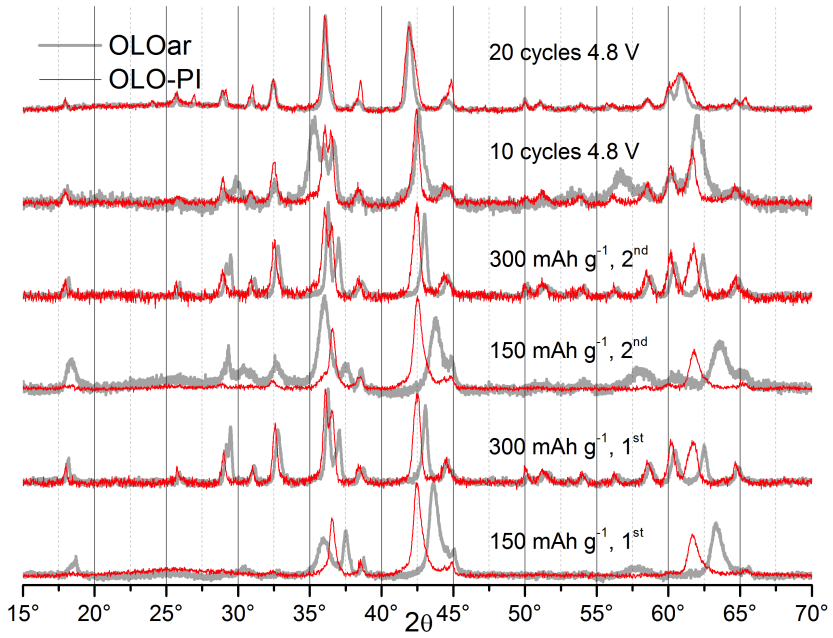

Figure 5.19: XRD spectra of decomposed OLOar and OLO-PI cathodes. All spectra are normalized to the highest peak intensity in the respective spectrum.

This implies that activation of the LMO component in the first cycle of OLO-PI cathode, and subsequent charge to 150 $mAh\ g^{-1}$, yields different structure than the same process in OLOar cathode. Hereby, it was not proven that OLO-PI cathodes at 150 $mAh\ g^{-1}$ have same structure before the thermal decomposition. However, they do decompose into nearly identical, Fm-3m crystallized phase, upon heating to 600°C under inert atmosphere. Prevalence of almost single-phase Fm-3m structure is in stark contrast with all other spectra. It indicates nearly complete reduction of nickel and cobalt to Ni^{2+} / Co^{2+}.

Spectra of both decomposed fully charged cathodes after 10 cycles are still fairly similar to those of fully charged cathodes in first two cycles, save for minor shifting of few peaks. Spectra of decomposed cathodes charged after 20 cycles boast prominent Fm-3m peaks, whereas peaks attributed to other phases (e.g. Fd-3m spinel) exhibit reduced relative intensity, compared to other spectra. This again indicates comparatively lower oxidation states of transition metals in the decomposed product. It implies that continuous cycling of both pristine and coated active material leads to structural changes that favour formation of rock salt structure during thermal decomposition. In case of OLOar, this may be caused by oxygen loss during cycling, which would lead to lower oxidation states of transition metals after 20 cycles. Coated OLO-PI on the other hand exhibits lower capacity decline - and thereby less oxygen loss - during cycling. It does however emit substantially higher amount of O_2 during thermal decomposition. This proposition still needs to be confirmed by investigating polyimide-coated cathodes using in-operando spectroscopic methods such as XRD and DEMS (differential electrochemical mass spectroscopy).

5.2.2.2 Kinetics and thermodynamics of decomposition reactions

In order to further elucidate the role of polyimide coating in thermal stability, two additional experiments were carried out on fully charged cathodes in the second cycle:

1. Determination of Arrhenius activation energy by TGA according to Friedman-Ozawa method (see subsection 3.3.1); washed and dried cathodes
2. Accelerating rate calorimetry (ARC); electrolyte-soaked cathodes

Samples from the second cycle were chosen because they have undergone the activation process in the first cycle, without being exposed to prolonged cyclic ageing. This should therefore enable sensible comparison between pristine and coated cathodes, unaffected by differences in first-cycle activation process or accumulated structural charges from extended cycling.

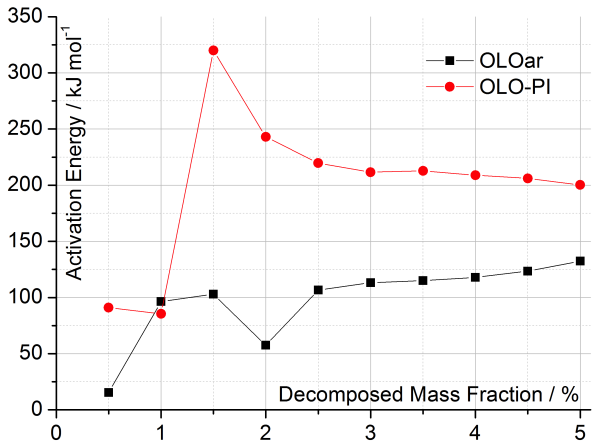

Figure 5.20: Arrhenius activation energy of thermal decomposition of fully charged OLOar and OLO-PI cathodes in second cycles

Figure 5.20 shows calculated Arrhenius activation energy over the course of decomposition reaction (represented by fraction of mass loss). Clear difference is observed between OLOar and OLO-PI cathodes above 1% mass loss: activation energy for decomposition of pristine OLOar is relatively low, starting at approximately 100 $kJ\ mol^{-1}$ and gradually increasing to 130 $kJ\ mol^{-1}$ at 5% mass loss. OLO-PI cathodes exhibit significantly higher activation energy of decomposition, peaking at 320 $kJ\ mol^{-1}$ and then asymptotically decreasing to 200 $kJ\ mol^{-1}$. Herewith it has to be noted that the first two calculated values at 0.5% and 1% mass loss are rather inaccurate, with low R^2 values of linear regression in Friedman-Ozawa plot.

Polyimide coating is therefore shown to increase activation energy of cathode decomposition. This means higher kinetic barrier to decomposition processes, particularly at lower temperature, and stronger dependence of reaction rate on temperature. Furthermore, decrease in activation energy with increasing conversion (represented by mass loss) is not usual and has not been observed in other experiments in the present work (cf. Figure 4.10 on page 44 and

Figure 5.9 on page 57). While the increasing activation energy is characteristic for competitive reactions, decreasing E_a typically implies reactions complicated by diffusion phenomena, and consecutive reactions [84]. It is reasonable to assume that presence of amorphous polyimide coating around active material particles affects diffusion of reaction products, at least in initial stages of decomposition before the coating itself disintegrates.

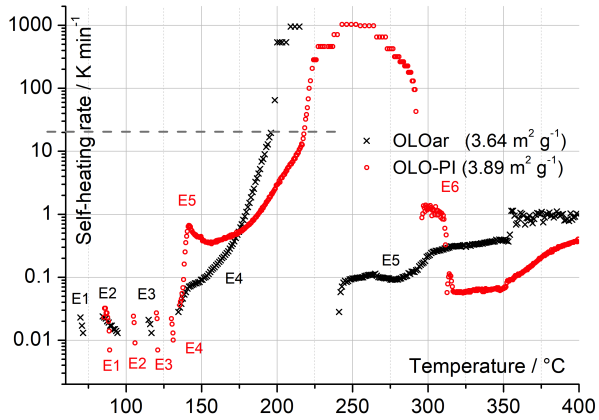

Figure 5.21: ARC exotherm profiles of fully charged OLO cathodes in second cycles. Cathode powders are soaked in electrolyte (1 M $LiPF_6$ in 1:1 FEC/DEC) in the ratio of 0.5 g of electrolyte per 1 g powder.

Figure 5.21 shows ARC exotherms for charged cathodes soaked in electrolyte. Initial reactions manifest themselves as series of low-intensity exotherms with decelerating self-heating rates. Self-sustaining reactions occur for both cathodes above 130°C. OLO-PI cathode reaction with electrolyte is initially characterized by abrupt increase in self heating rate up to 140°C. After that, SHR slightly decreases and starts increasing gradually after 155°C. SHR of OLOar reaction with electrolyte increases steadily after onset and overtakes OLO-PI at approximately 175°C. Beyond this temperature, OLOar reaction exotherm remains above that of OLO-PI until it is interrupted at 215°C. Before that, both samples have exceeded the SHR of 20 $K\ min^{-1}$, specified as tracking limit of the calorimeter.

The distinctive profile of the OLO-PI exotherm is in line with the idea of consecutive reactions discussed above. However, one has to note that unlike other experiments reported in this section, ARC was conducted on cathode-electrolyte system, which implies reaction of cathode and its decomposition products on one hand, with the electrolyte on the other. Additionally, ARC sample holder is a closed system that prevents any evolved gases from escaping. It appears that OLO-PI reacts with electrode in two stages: first one is extremely fast, and the subsequent has slower rate than that of OLOar reaction.

5.2.3 Particle size of OLO cathodes' active material and thermal stability

5.2.3.1 Properties of synthesized active materials

Six batches of OLO active material synthesized according to process described in section 3.1.1.2 (page 23) are summarized in Table 5.6. Samples annealed at lower temperatures exhibit higher surface area and therefore smaller particle size. Surface area and particle size are also dependent on lithium source used during synthesis: utilisation of LiOH leads to consistently higher surface area at same annealing temperature than Li_2CO_3. Figure 5.22 shows SEM images of the synthesized materials. Samples H800, H900, and H1000, synthesized with LiOH appear to have a broader and less homogeneous particle size distribution.

Table 5.6: Overview of synthesized OLO samples and their BET surface area

	Sample	Lithium source	Annealing temperature	Surface area / m^2g^{-1}
OLO-C	C800	Li_2CO_3	800°C	3.25
	C900	Li_2CO_3	900°C	2.25
	C1000	Li_2CO_3	1000°C	1.90
OLO-H	H800	LiOH	800°C	4.14
	H900	LiOH	900°C	3.63
	H1000	LiOH	1000°C	2.38

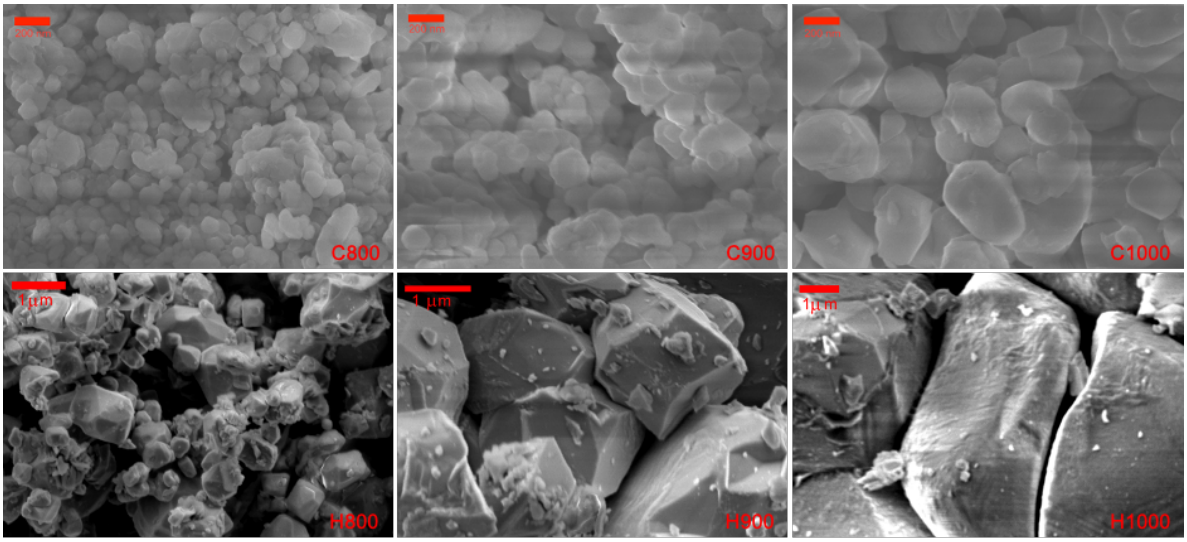

Figure 5.22: SEM images of synthesized OLO materials

Figure 5.23 shows half-cell (vs. $Li|Li^+$) electrochemical performance of the cathodes coated with the synthesized materials. First cycle charge is characterized by a typical sequence of two voltage plateaus. Both charge and discharge capacities of the first cycle appear uncorrelated to active materials' surface area. Furthermore, capacities of the cathodes are decreasing rapidly with cycling, which is comparable to cycling results of as-received OLOar material (cf. Figure 5.15 on page 66). These results differ from the findings of Tang et

al. [71], who reported increasing capacity in the first few cycles for the active material synthesized with Li_2CO_3. Nevertheless, it has to be noted that the cited work refers to the nickel-rich and low-cobalt $0.5Li_2MnO_3{-}0.5Li[Ni_{0.8}Co_{0.01}Mn_{0.19}]O_2$. In present research, $0.4Li_2MnO_3{-}0.6Li[Ni_{1/3}Co_{1/3}Mn_{1/3}]O_2$ was synthesized.

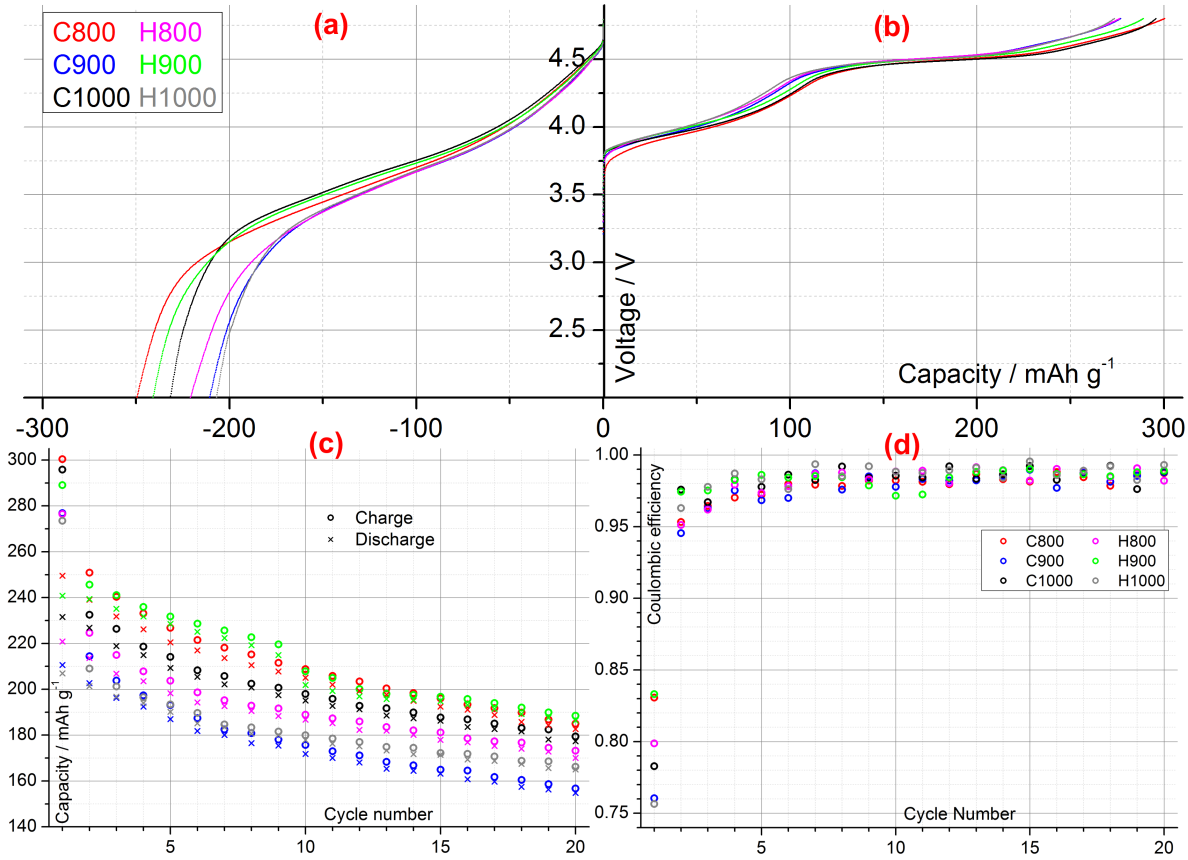

Figure 5.23: Comparison of synthesized materials' electrochemical performance: First cycle discharge (a) and charge (b) profiles, (c) charge and discharge capacities in first 20 cycles, (d) Coulombic efficiencies for first 20 cycles. $I = 25\ mA\ g^{-1}$

5.2.3.2 Thermal analysis and mass spectrometry of dried cathodes from synthesized materials

Differences in thermal behaviour between cathodes of varied surface area and different lithium source at synthesis shall be interpreted in accordance to previously cited and discussed structural findings. Koga et al. [66, 69, 70] reported different mechanisms of oxygen oxidation in over-lithiated transition metal oxides: Release of gaseous O_2 at particles' surface and a reversible redox reaction in the bulk, which may result in either peroxide-like structure or localized electron holes on oxygen anions [109, 110]. In addition, Tang et al. [71] have shown that using different lithium sources for the solid-state synthesis of OLO material leads to slightly different products in terms of phase distribution. Using Li_2CO_3 as lithium source

leads to NCM-like phase (R-3m) being more concentrated at the surface and LMO-like phase (C2/m) more concentrated in the bulk of the particles. LiOH as lithium source would lead to the opposite outcome.

As mentioned in section 5.2.3.1 above, present research deals with slightly different stoichiometry of OLO. Also, extensive TEM analyses supported by annular bright field (ABF) and high-angle annular dark field (HAADF) imaging techniques were not conducted to validate the synthesis products. Nevertheless, structural properties reported by Tang et al. in conjunction with results of Koga et al. on particle size effects do offer a fitting framework for interpretation of differences in thermal behaviour between OLO-C and OLO-H samples, reported hereinafter.

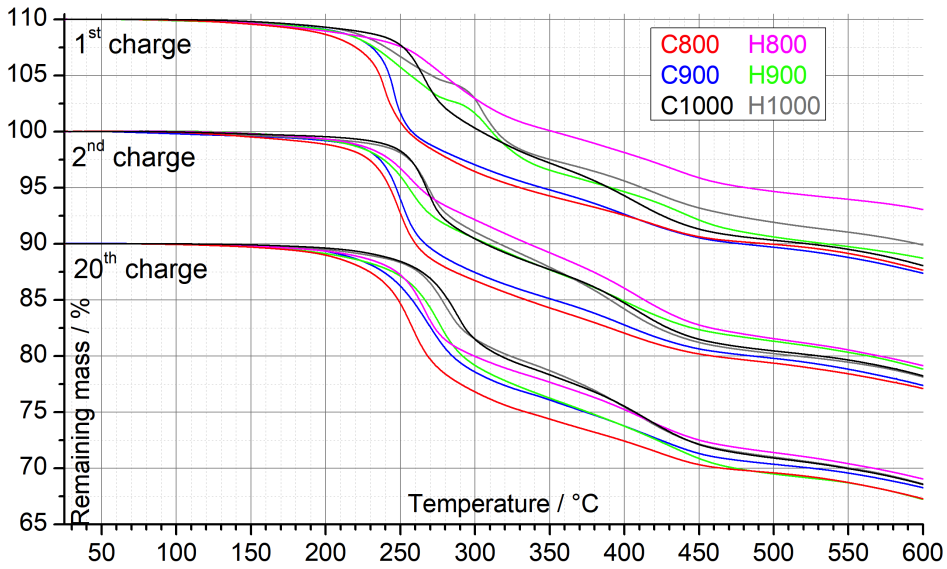

Figure 5.24: TGA curves for decomposition of cathodes charged in first, second, and twentieth cycle ($\beta = 5\ K\ min^{-1}$)

Figure 5.24 shows TGA curves of fully charged cathodes. Onset temperatures of these TGA measurements are summarized in Table 5.7. Clear trend of falling onset temperature with rising surface area can be observed for cathodes synthesized with Li_2CO_3 precursor (hereinafter: OLO-C). Onset temperature also increases with cycle number for all OLO-C samples, which is in line with observations from OLOar (Table 5.5 on page 68). Cathodes with active material synthesized from LiOH (hereinafter: OLO-H) show different decomposition behaviour in first and second charge:

- Samples H900 and H1000 exhibit a two-staged mass loss curve after first charge, with a second onset between 290°C and 295°C.
- Sample H800 exhibits a more gradual mass loss both after first and second charge. Its total mass loss after first charge stands out by being more than 3 percentage-points lower than the rest.

Cathodes charged after 20 cycles decompose in a fairly comparable manner. Onset temperature is increased for all cathodes after cycling, compared to samples charged in first two cycles. Within the OLO-C batch of samples, the difference in onset temperatures is more pronounced than in case of OLO-H. Furthermore, at nearly equal surface areas (e.g. C800 and H900 or C900 and H1000), most fully charged cathodes from OLO-H group start decomposing at higher temperatures than OLO-C cathodes. Notable exception is H1000 charged in first cycle, with aforementioned two-staged TGA profile.

Table 5.7: Summary of TGA onset temperatures in °C

	C800	C900	C1000	H800	H900	H1000
Surface area / $m^2 g^{-1}$	3.25	2.25	1.90	4.14	3.63	2.38
1st cycle 4.8 V	229.1	236.7	250.2	241.8	216.5	215.5
2nd cycle 4.8 V	234.5	237.4	255.6	237.1	236.6	254.7
20 cycles 4.8 V	239.4	242.4	268.0	253.0	255.0	263.1
1st cycle 150 mAh^{-1}	235.2	258.6	320.6	249.7	207.5	216.6
2nd cycle 150 mAh^{-1}	277.0	302.9	320.9	257.0	252.0	287.2

Decomposition of cathodes charged to 150 $mAh\ g^{-1}$ is described by TGA curves in Figure 5.25. OLO-C cathodes are characterized by the behaviour previously observed in OLOar and OLO-PI samples (cf. Figure 5.11 on page 60 and Figure 5.16 on page 67): Onset temperature is higher for cathodes charged in second cycle. The magnitude of this phenomenon is almost equal for C800 and C900. TGA profile of C1000 cathode exhibits slightly different shape in second cycle, however the shift towards increased temperature is evident. Structure stabilization behind this phenomenon has been discussed in the previous sections.

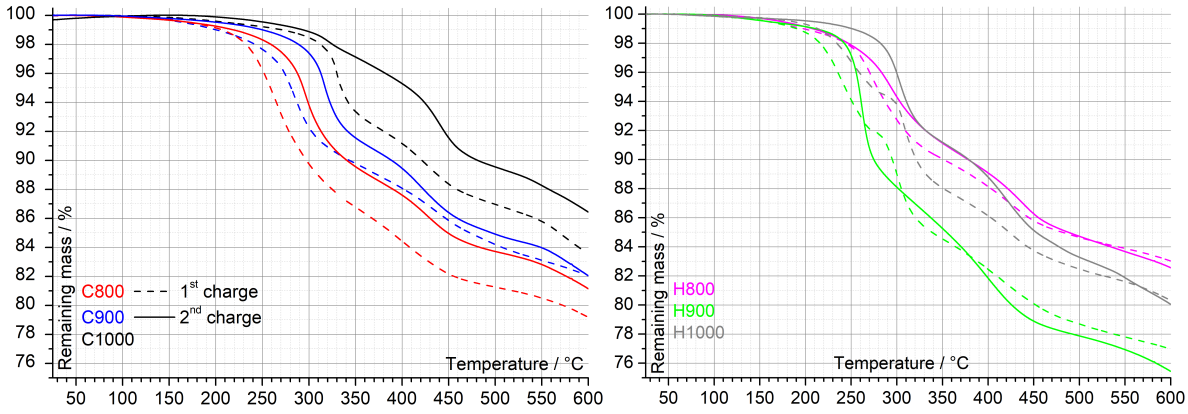

Figure 5.25: TGA curves for decomposition of cathodes charged to 150 $mAh\ g^{-1}$ in first and second cycle ($\beta = 5\ K\ min^{-1}$)

In comparison, OLO-H cathodes charged to 150 $mAh\ g^{-1}$ exhibit completely different behaviour. TGA curves of H900 and H1000 cathodes charged in first cycle indicate a two-staged decomposition with second stage onset between 290°C and 300°C. Same phenomenon has been observed in fully charged cathodes of same materials in the first cycle. H800 cathodes

at 150 $mAh\ g^{-1}$ cumulative capacity in first and second charge exhibit almost overlapping TGA curves. In general, differences in decomposition onset temperature depending on surface area or cycle number are considerably smaller for OLO-H cathodes, compared to their OLO-C counterparts.

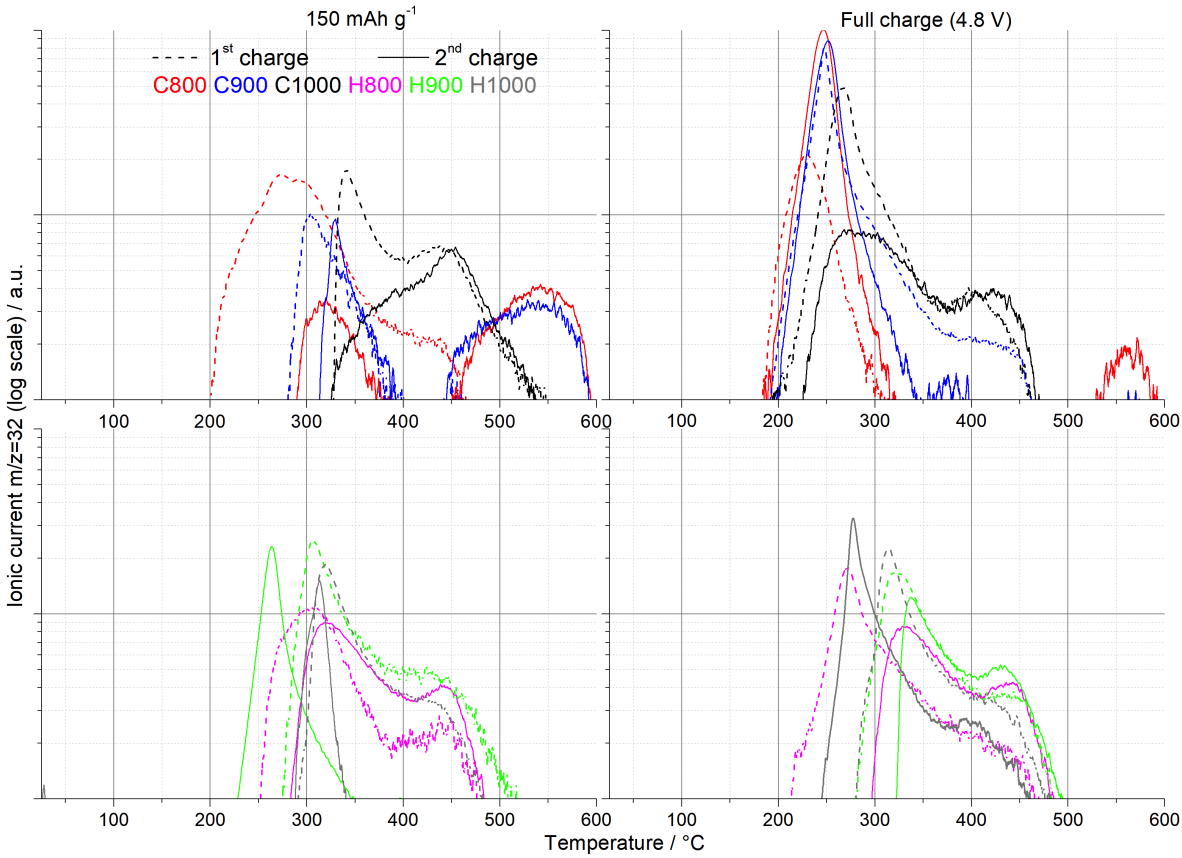

Figure 5.26: Mass spectrometry profiles related to evolution of O_2 ($m/z = 32$) during thermal decomposition of OLO-C and OLO-H cathodes charged in first two cycles

Gaseous oxygen (O_2) emission during the decomposition of cathodes was measured by mass spectrometer and is shown in Figure 5.26 for cathodes in first and second cycle. OLO-C cathodes in first two cycles show generally taller and broader $m/z = 32$ peaks, indicating that more O_2 is emitted during decomposition compared to OLO-H. Also, OLO-C cathodes emit more O_2 when they decompose at higher state of charge. At 150 $mAh\ g^{-1}$, O_2 emission is shifted towards higher temperatures, and its intensity is reduced. This is most evident for C800 sample. For OLO-H cathodes, the difference in intensity of O_2 MS profiles between fully charged (4.8 V) and "half-charged" (150 $mAh\ g^{-1}$) is almost negligible. In case of H900 and H1000 cathodes charged in first cycle, distinguished by their two-staged TGA curves, it appears that O_2 emission overlaps with the second stage of mass loss.

OLO-C cathodes are based on previously cited research implied to have their LMO phase more concentrated in the bulk of their particles. LMO activation manifests itself through O_2 emission on the surface and oxygen oxidation in the bulk. This means that after first full

charge to 4.8 V, OLO-C active material should have higher concentration of unstable oxygen, either in form of peroxide-like ions or localized electron holes around oxygen atoms, compared to OLO-H. Such structure yields higher amount of O_2 gas at elevated temperature. On the other hand, OLO-H active material of comparable surface area at equal state of charge has more of its LMO phase at particles' surface, where O_2 is readily emitted during first and subsequent charge steps. Concentration of unstable oxygen in crystal structure is therefore comparatively lower.

This phenomenon offers a hypothesis to explain why difference in surface area has more pronounced impact on thermal stability of OLO-C cathodes compared to OLO-H. Higher surface area of C800 and C900 samples implies more concentrated LMO phase in the bulk, leading to higher concentration of unstable oxygen. Conversely, OLO-H particles have their LMO phase more concentrated on the surface, where it is stabilized by O_2 release during charge. Difference in concentration of unstable oxygen between various OLO-H samples is therefore either smaller or non-existent. This hypothesis needs to be verified in the future by appropriate structural and surface characterization methods applied on charged cathodes at various stages, or preferably in-operando. OLO-C cathodes therefore exhibit thermal behaviour more similar to OLOar[1], which is discussed in section 5.2.1.

Higher incidence of LMO phase on the surface of OLO-H particle may further explain certain distinctive aspects of its thermal behaviour:

- H800 particles with highest surface area and LMO phase concentrated at the particles' surface should exhibit lowest concentration of unstable oxygen. This results in gradual slope of TGA curve during decomposition and considerably lower final mass loss.
- LMO activation in OLO-H mainly occurs at surface during upper voltage plateau of the first charge, involving irreversible process of O_2 release. This leads to more reversible redox reaction of NCM in the bulk, leading to less difference in oxidation states of transition metals in cathodes charged to 150 $mAh\ g^{-1}$ in first and second cycle. This in turn means less difference in thermal stability between cathodes charged in first and second cycle.
- Distinctive two-staged decomposition of H900 and H1000 charged to 150 $mAh\ g^{-1}$ and 4.8 V may imply formation of two different phases in material with different onset temperature.

MS profiles of cathodes charged after 20 cycles are presented in Figure 5.27 and show fewer differences between materials. Peak intensity of $m/z = 32$ ionic current is nearly equal for all samples except for C800, which is twice as high as the rest. Onset and peak temperatures for OLO-C cathodes are decreasing with surface area, whereas no such trend is observed for

[1]Samsung SDI has not disclosed which material was used as lithium source in synthesis of OLOar. Both OLOar and precursor from Samsung SDI were obtained prior to publication date of the cited article by Tang et al. [71].

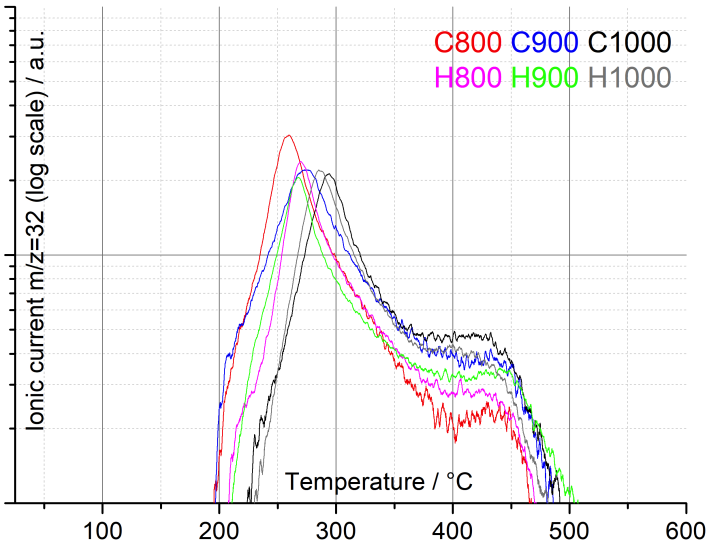

Figure 5.27: Mass spectrometry profiles related to evolution of O_2 ($m/z = 32$) during thermal decomposition of OLO-C and OLO-H cathodes charged after 20 cycles

OLO-H cathodes. Nonetheless, it appears that prolonged cycling reduces the differences in thermal behaviour of the cathodes. The reason for this convergence is likely to be continuous degradation of the active material over cycles - less than 190 $mAh\ g^{-1}$ can be charged or discharged after 20 cycles. At such low capacity, it is reasonable to assume that the role of reversible oxygen redox reaction is reduced, and the distribution of LMO and NCM domains on particle level no longer play a defining role in cathodes' thermal stability. Therefore, reported experiments must be repeated on over-lithiated oxide with improved cyclic stability to properly assess impact of prolonged cycling.

Impact of surface area or particle size of active material alone on cathodes' thermal stability is less significant than the impact of structural difference caused by using different lithium sources in synthesis. However, surface areas of synthesized materials reported in Table 5.6 are spread over a relatively narrow range of values, especially compared to $LiCoO_2$ investigated in section 5.1.

5.2.3.3 Calorimetry of cathode-electrolyte reaction

Figure 5.28 shows ARC exotherms of reactions between fully charged cathode powders (in second cycle) and the electrolyte used in OLO half cells. Onset temperature of self-sustaining exothermal reactions under adiabatic conditions is in the range between 135°C and 146°. OLO-C cathodes are distinguished by faster increase in self-heating rate. This is in line with above discussed idea of higher concentration of unstable oxygen in OLO-C cathodes, leading to faster oxidation of electrolyte. Sample C1000 exhibits slightly earlier onset of reaction, but more gradual increase in self-heating rate. The latter may be attributed to lower surface area at which the reaction between oxygen and electrolyte can occur.

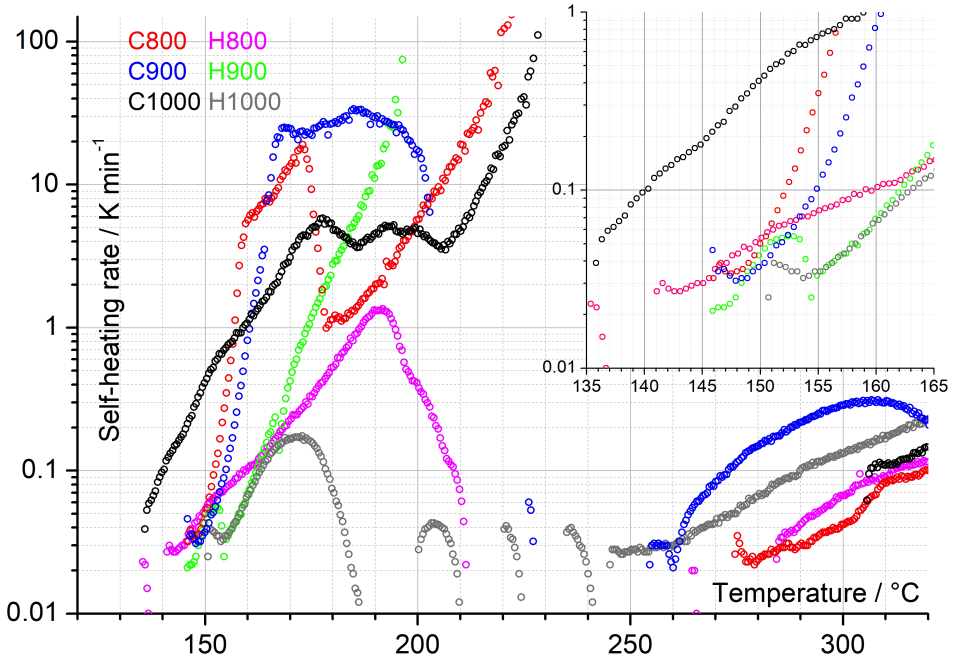

Figure 5.28: ARC exotherm profiles of fully charged cathodes in second cycles. Cathode powders are soaked in electrolyte (1 M $LiPF_6$ in 1:1 FEC/DEC) in the ratio of 0.5 g of electrolyte per 1 g powder.

OLO-H cathodes have their self-heating rate increasing with temperature in a more gradual manner. The reactions of H1000 and H800 are extinguished at 187°C and 211°C, respectively. Reaction of H900 is terminated at 196°C, at much higher self-heating rate. These three exotherms imply a simple, single-staged reaction between cathode and electrolyte. The self-heating rates of OLO-C cathodes reach a peak or plateau between 165°C and 180°C, indicating a multi-stage reaction.

6 Discussion on Applicability of Microstructural Findings on the Battery Cell Level

In the previous chapters, thermal behaviour of Li-ion cells was gradually broken down to critical components and their properties. Key parameters such as reaction onset temperatures, activation energies, and reaction enthalpies were experimentally determined. Variation of these parameters can impact the overall thermal stability of a Li-ion cells. It would take a tremendous effort to investigate this impact empirically, as cells would have to be built in which the component properties would have to be altered in a controlled manner.

As an alternative to such laborious approach, one may consider building a mathematical model in order to validate microstructural results and their impact on cell-level behaviour. Such model can enable analysing the variations in above mentioned materials' parameters and resulting changes to cell thermal behaviour.

6.1 Simplified mathematical model for battery cell thermal runaway

6.1.1 Model assumptions

The model built for purpose of the present dissertation is based on following assumptions:

1. Model is zero-dimensional (0D). This neglects the dimensions and shapes of the cell, as well as local heat transfer within the cell.
2. Model assumes adiabatic conditions. There is no heat transfer between battery cell and its surroundings. This enables a comparison of model data with ARC results.
3. Boundary condition of the model is the overall onset temperature T_{on}, at which the anode reaction is started.
4. Cell remains a closed system throughout the course of modelled thermal runaway; no rupture of housing and consequent reaction between cell inside and outside atmosphere, no volume work due to expansion.

5. Reactions occur within anode and cathode separately; each of electrodes is considered to be soaked in electrolyte.
6. No internal short circuits occur: one can assume a hypothetical ceramic layer within separator that never melts.
7. Specific heat capacity of cell and its components remains constant in the given temperature range.

Such model greatly simplifies the mathematical description of thermal runway behaviour. This enables a relatively simple assessment of how changes in individual active material properties impact the thermal stability and safety of the system. There are however several caveats to heed while analysing an input of a mathematical model describing thermal behaviour of a cell:

- Inputs to the model in this chapter are thermodynamic and kinetic parameters. These are however just a proxy for physico-chemical properties of the materials. Variation of parameters does not necessarily translate to controlled changes of material properties.
- Zero-dimensional model assumes homogeneity of the cell. Thus, there is no heat transfer within the cell. In reality, heat-generating reactions are limited to certain regions within the cell. In present model, this is not the case.
- Model neglects two very important reactions of thermal runaway: (i) anode-cathode reaction occuring as consequence of internal short circuit and (ii) ignition of electrolyte by oxygen leaked in from the atmosphere (in the inevitable event of casing rupture). This renders the model useless at higher temperatures. It is nevertheless assumed that the model sufficiently describes the earlier stages of thermal runaway.
- Onset temperature of cell self-heating is one of the initial conditions in the model. This follows to logic of ARC HWS experiment, but is rarely a realistic trigger mechanism of thermal runaway.

In consideration of all its shortcomings, the purpose of this model is to explore how the key thermodynamic and kinetic properties of anode and cathode decomposition reactions affect the course of thermal runaway. These properties are onset temperature T_{on}, activation energy E_a, and reaction enthalpy Δh. Variations in above mentioned parameters can then be linked to changes in microstructural properties, based on the experimental results from previous chapters.

6.1.2 Model battery cell type, dimensions, and composition

The model is based on a 18650-type cell described in section 3.1.3, which was used in experiments discussed in Chapter 4. Based on post-mortem analysis of a fresh cell, mass fractions of individual components were determined. They are summarised in Table 6.1. The mass

fractions of anode, cathode, and separator are assumed to account for electrolyte in which they are soaked. The mass fraction w_{other} contains inert auxiliary components such as current collector foils, stainless steel housing tube, mandrel, tabs, positive terminal cap, and gasket.

Table 6.1: Parameters of the model cell

m_{Cell}	42.35	g
$C_p(cell)$	37.5	$J\ K^{-1}$
w_{An}	0.275	
w_{Cath}	0.377	
w_{Sep}	0.042	
w_{other}	0.306	

6.1.3 Model description

6.1.3.1 Energy balance

The desired output of the model is the thermal profile (self-heating rate) of the cell over time and over temperature, which is directly proportional to exothermal heat flow, assuming that heat capacities of cell ($C_{p,cell}$) and cell holder ($C_{p,holder}$) remain constant and that the system is adiabatic:

$$\frac{dQ}{dt} = (C_{p,cell} + C_{p,holder}) \cdot \frac{dT}{dt} \tag{6.1}$$

Heat generation from chemical reactions corresponds to a sum of enthalpies and rates of all reactions:

$$\frac{dQ}{dt} = \sum_i [\Delta H_i \cdot \frac{d\alpha_i}{dt}] \tag{6.2}$$

If reactions occur separately in different components, namely anode and cathode (assumption 5 in section 6.1.1), reaction enthalpies can be expressed by specific enthalpies of individual reactions and mass fractions of the respective components:

$$\Delta H_i = \Delta h_i \cdot w_i m_{Cell} \tag{6.3}$$

Thus, one can summarize the energy balance of the model as the relationship between temperature rate and reaction rate in equation (6.4) below:

$$(C_{p,cell} + C_{p,holder}) \cdot \frac{dT}{dt} = \sum_i [\Delta h_i w_i m_{Cell} \frac{d\alpha_i}{dt}] \tag{6.4}$$

6.1.3.2 Reaction kinetics

Anode reaction encompasses a sequence of SEI decompositions followed by a lithium-electrolyte reaction, as discussed in section 4.2.1.1. Richard and Dahn [111] have developed an anode reaction model based on their own experimental results [30], which were also discussed in the section 4.2.1.1. Their proposed model describes SEI decomposition and lithium-electrolyte reaction as two simultaneous processes, following the Arrhenius approach for relationship between reaction rate and temperature.

For the model built in the scope of present work, one shall assume single first-order reaction following the Arrhenius kinetics. This simplification is justified by experimental results reported in chapter 4. Namely, anodes exhibit a nearly constant apparent activation energy over the course of decomposition (see Figure 4.8 on page 42). Reaction rate for anode decomposition is thus described by equation (6.5):

$$\frac{d\alpha_{An}}{dt} = k_{0,An} \exp\left(-\frac{E_{a,An}}{R_m \cdot T}\right) \cdot (1 - \alpha_{An}) \tag{6.5}$$

Decomposition of a lithium - transition metal oxide cathode was reported to be a mixed-order autocatalytic reaction by MacNeil et al. [112]. The equation for such process is written as:

$$\frac{d\alpha_{Cath}}{dt} = k_{0,Cath} \exp\left(-\frac{E_{a,Cath}}{R_m \cdot T}\right) \cdot (1 - \alpha_{Cath})(b + \alpha_{Cath}^{0.5}) \tag{6.6}$$

Where $b = 0.1$ is a parameter of autocatalysis. The exponent of 0.5 over the autocatalytic element in equation (6.6) has no chemical justification and merely indicates that the ability of produced catalyst is highest in the initial stages of reaction [112].

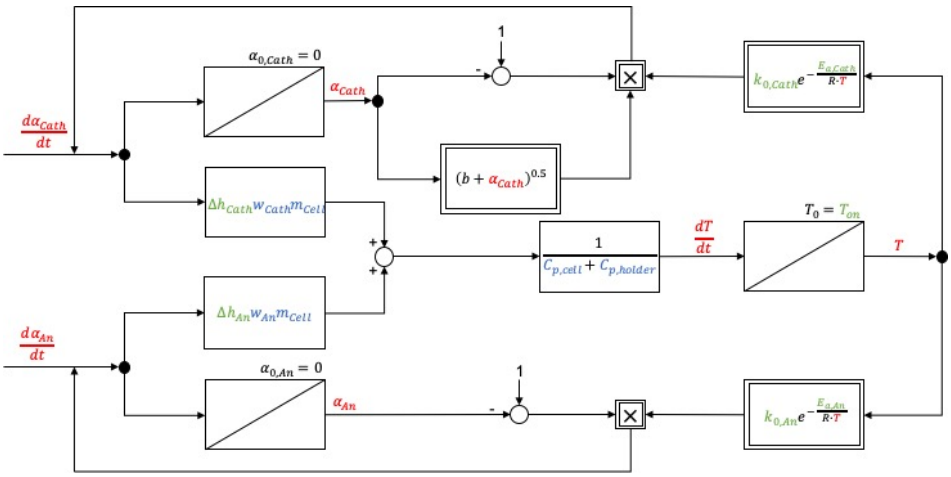

Figure 6.1: Block diagram of the proposed model

6.1.3.3 Model parameters and boundary conditions

Figure 6.1 shows block diagram of the above described mathematical model. Marked in blue colour are the cell properties summarized in Table 6.1 and the heat capacity of sample holder ($C_{p,holder} = 37\ J\ K^{-1}$). Variables temperature (T) and conversion (α_{An}, α_{Cath}), as well as their first order derivative over time, are marked red. Key thermodynamic and kinetic parameters of the decomposition reactions are marked green.

These parameters, one set for each electrode are onset temperature (T_{on}), specific reaction enthalpy (Δh), and Arrhenius equation parameters: activation energy (E_a) and frequency factor (k_0). Parameter values for initial calculation are summarized in Table 6.2.

Table 6.2: Initial parameters for model calculation

	T_{on} / °C	Δh / $J\ g^{-1}$	E_a / $kJ\ mol^{-1}$	k_0 / min^{-1}
Anode	115	300	80	$3 \cdot 10^7$
Cathode	150	410	144	$8.33 \cdot 10^{14}$

Onset temperature for anode reaction is set at 115°C, which is in line with temperature of self-sustaining reaction for the model cell, as determined experimentally by ARC (cf. Figure 4.11 on page 45). Reaction enthalpy and activation energy are taken from thermal analysis experiments on model cell anode as described in Chapter 4. Frequency factor was determined iteratively to fit the model results with experimental data. Same approach has been reported for certain anode reactions in literature [111]. It is namely not possible to calculate k_0 from TGA data using model-free kinetics approach (see section 3.3.1 on page 28).

Designation of initial parameters for cathode reaction has proven more challenging due to the fact that thermal analysis experiments in Chapter 4 were conducted on dried cathodes. This does not take into account the presence of electrolyte, which impacts the reaction significantly. Therefore, values from similar research by MacNeil et al. [112] are used.

Following boundary conditions are assumed for the model:

- Initial temperature equals onset temperature of anode reaction. Initial conversion for both reactions is zero.

$$t = 0;\ T = T_{on,An},\ \alpha_{An} = 0,\ \alpha_{Cath} = 0 \tag{6.7}$$

- Rate of cathode reaction equals zero at temperatures below onset temperature of cathode decomposition. This means that cathode reaction is only triggered after onset temperature is reached.

$$T < T_{on,Cath} \Rightarrow \frac{\alpha_{Cath}}{dt} = 0 \tag{6.8}$$

6.1.4 MatLab model and initial results

Described model was solved by *ode45* function in MatLab. The function uses Runge-Kutta numerical method [113] to solve systems of first-order differential equations of the form

$$\frac{dy}{dt} = f(t,y);\ y(t_0) = y_0 \tag{6.9}$$

The model script can be found in Appendix A.3.

Figure 6.2 shows model output compared to experimentally conducted thermal runaway of the model cell (cf. Figure 4.11 on page 45). The model fits the experimental data reasonably well in first stage at temperatures below 150°C. Reaction is assumed to be entirely on the anode side in this range. Therefore, a satisfactory overlap between experimental and model data is expected since anode parameters were either taken from results of anode experiments or, in case of k_0, fitted to experimental data. The most prominent difference is that the self-heating curve calculated by model does not exhibit the interruption caused by separator or binder melting process.

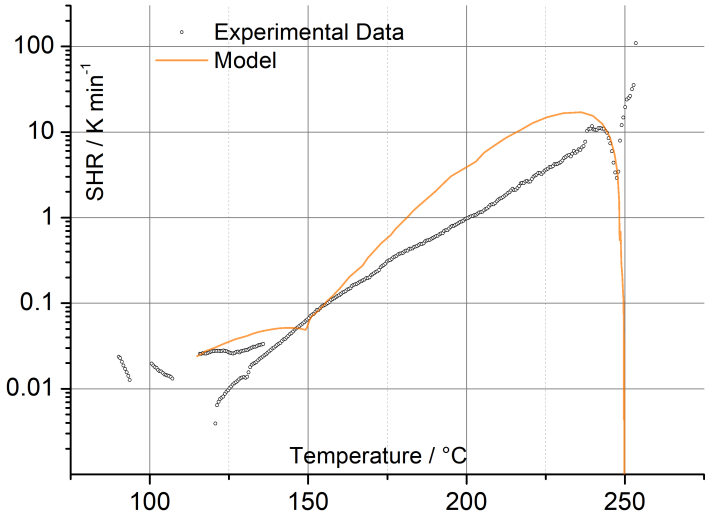

Figure 6.2: Comparison between experimental ARC results of fresh model cell and initial model calculation

At temperature above 150°C, the model assumes heat generation from cathode decomposition as well. The calculated SHR curve beyond 150°C is initially steeper than the experimental one. At approximately 230°C - 240°C, a decline is observed in both curves, related to the completion of electrode-electrolyte decomposition reactions. This is in experimental case followed by cell opening and reaction with atmospheric air, which is reflected by increase in self-heating rate in experimental data. These reactions are not accounted for in the model. The discrepancy between experimental and model data in the interval between 150°C and 250°C originates from using literature data for cathode (as explained in subsection 6.1.3.3) instead of experimental data from model cell cathode.

6.2 Sensitivity analysis of thermodynamical and kinetic parameters

6.2.1 State of no return as criterion

In order to place results of parameter analysis in a context, a concept called **state of no return** shall be defined as condition at which complete thermal runaway of the cell is inevitable. Conditions for state of no return are defined for the coordinate system of self-heating rate versus temperature in which the modelling results are presented in the form of exotherms. In present work, state of no return shall be defined by two conditions, one for temperature and one for self-heating rate:

1. **Collapse of separator:** Internal short circuit as result of separator collapse leads to a violent reaction between anode and cathode. Polypropylene is the separator component than melts at higher temperature (in contrast to easier-melting polyethylene). Melting point of commercial grade polypropylene can reach up to 171°C [114]. Nevertheless, melting alone does not immediately cause the separation layer to break down. While the actual conditions of separator collapse likely vary by cell type and depend on factors such as its thickness and pressure applied on the layers, recent research by Feng et al. [115] suggests the value of 192.4°C as temperature of separator collapse. Therefore, $T = 190°C$ shall be taken as an approximation for temperature limit in present work.

2. **Cooling ability:** Section 6.1.1 presumes adiabatic conditions around the observed battery cell. In absence of any endothermal reactions in the model, this implies that temperature can only increase or remain constant over time. Under such conditions, any self-heating rate will lead to temperature increasing until the degree of conversion of all reaction reaches 1. However, a state-of-no-return condition in terms of self-heating rate shall be defined as well. For this, a hypothetical scenario is assumed: the cell may at any time be taken out of adiabatic environment and placed under isothermal conditions with ambient temperature and forced convection cooling. The criterion for state of no return is that heat generated in the cells exceeds heat dissipation by forced convection. This can be expressed in terms of heat balance:

$$(C_{p,cell} + C_{p,holder})\frac{dT}{dt} = k_{HT}A(T - T_{amb}) \tag{6.10}$$

   Heat transfer coefficient k_{HT} between cell housing and air has been estimated to $5\ W\ m^{-2}\ K^{-1}$ by Tanaka and Bessler [116]. Ambient temperature is assumed to be $T_{amb} = 25°C$.

Above stated criteria are schematically presented in Figure 6.3. State of no return is outside of the area defined by the curves corresponding to the two conditions.

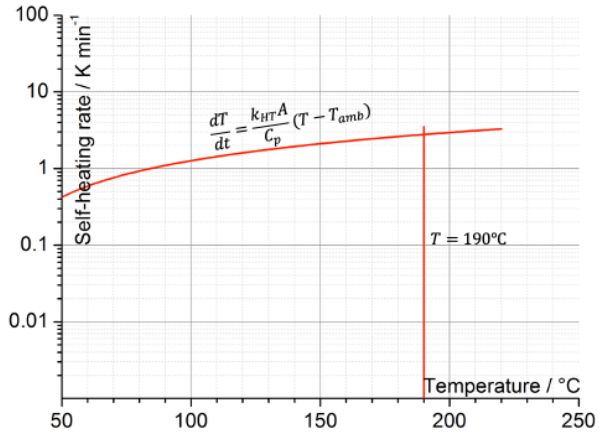

Figure 6.3: Schematic representation of the criteria for state of no return

6.2.2 Variation of parameters

6.2.2.1 Anode reaction

Reaction in a carbon-based anode typically starts at lower temperature than cathode reaction. By tuning out the latter, model simulates a case where no decomposition is occurring in the cathode as long as the separator does not break down - for example thermal runaway in a $LiFePO_4$-cell. In addition, running the anode side of the model only shows whether the anode reaction can push the system towards following critical states:

Temperature
For continuation of thermal runaway, it is crucial that temperature of cathode reaction onset is achieved. Furthermore, a collapse of the separator and consequential internal short circuit would lead to additional heat generation. It is technically possible for thermal runaway to occur even without separator collapse [117]. Nevertheless, the present work assumes the separator collapse temperature as a point of no return, particularly because polyolefin separator is used in the model cell. In the given model, the ability of system to reach either of these two temperatures depends solely on two parameters, namely anode reaction enthalpy and onset temperature. Minimum anode reaction enthalpy $\Delta h_{An}(min.)$ to reach temperature T is given by equation (6.11) below:

$$\Delta h_{An}(min.) = (C_{p,cell} + C_{p,holder})(T - T_{on})\frac{1}{w_{An} m_{Cell}} \tag{6.11}$$

With the initially assumed onset temperature $T_{on} = 115°C$, the minimum Δh_{An} would be 223.7 $J\ g^{-1}$ to reach the cathode reaction onset of 150°C, or 479.4 $J\ g^{-1}$ to reach separator collapse temperature of 190°C. In the latter case, internal short circuit would accelerate thermal runaway without any thermal contribution from cathode decomposition. A lower onset temperature would require higher reaction enthalpy to reach the target temperature according to equation (6.11). In case of previously discussed aged cells (cf. Figure 4.11 on

page 45), T_{on} was lowered to 75°C as consequence of ageing. At such low onset, Δh_{An} of 479.4 $J\ g^{-1}$ and 735.1 $J\ g^{-1}$ would be required to reach 150°C and 190°C, respectively. In fact, it was observed that in case of 2 cells (Batches C and D) stopped self heating at 108°C and 120°C. ARC profiles of their anodes (Figure 4.7 (left) on page 40) also exhibit smaller area under their respective exotherm curves, indicating lower total reaction enthalpy in comparison to other cells. Variation of Δh_{An} and T_{on} can therefore be independent from each other to some degree, albeit not completely random.

Self-heating rate

In order to predict whether the anode reaction alone can generate cell-level self-heating rate above the threshold defined in section 6.2.1, maximum SHR with given set of parameters needs to be determined. Resulting SHR at a given temperature is obtained by numerically solving differential equations of the present model. Thus, criteria for individual parameters cannot be devised in integral form, as in equation (6.11). SHR is a function of all thermodynamic (Δh_{An}, T_{on}) and kinetic (k_0, E_a) parameters. Its maximum and/or crossing of the threshold defined by equation (6.10) can only be determined numerically or by iteration.

Table 6.3: Parameter variation matrix for anode

$T_{on,An}$ / °C	75	115	135
Δh_{An} / $J\ g^{-1}$	200	300	500
$E_{a,An}$ / $kJ\ mol^{-1}$	70	80	90

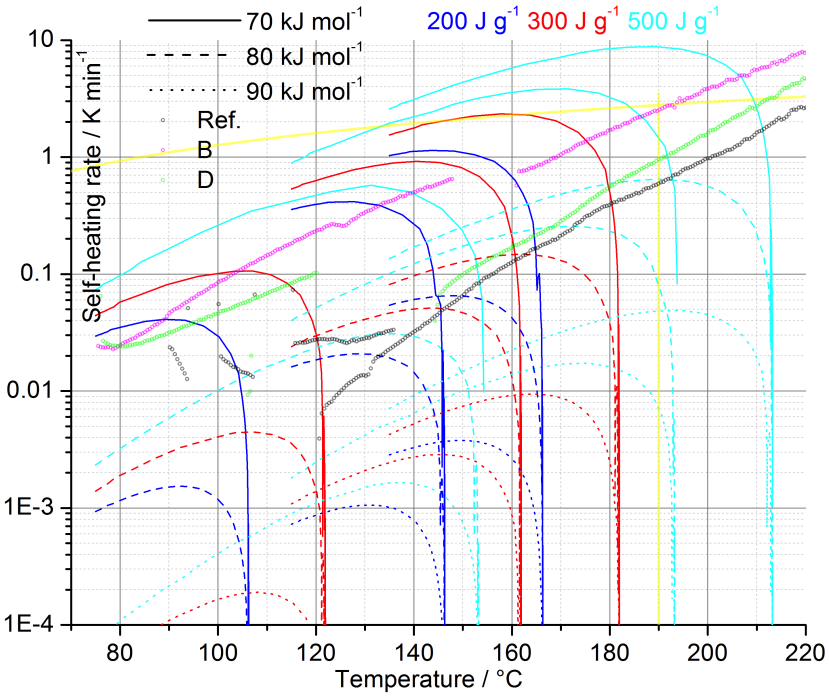

Figure 6.4: Results of model calculations for anode reaction only with parameters from Table 6.3

Table 6.3 shows the matrix of parameter variation, assuming that only anode reaction occurs.

Calculated results in form of exotherms are presented in Figure 6.4. Experimental ARC results of new (reference) and aged (batches B and D) cells are overlaid on the chart (cf. Figure 4.11 on page 45). By comparing the results with the curve calculated from the initial parameters (115°C, 300 $J\ g^{-1}$, 80 $kJ\ mol^{-1}$), following observations are noted:

- Critical self-heating rate as defined above is reached only by combination of at least two of the following parameters: high reaction enthalpy, low activation energy, and/or high onset temperature.
- Higher activation energy results in extremely low self-heating rates. Note that 0.02 $K\ min^{-1}$ is the sensitivity of the ARC calorimeter used in experiments. Most of the parameter combinations with activation energy of 90 $kJ\ mol^{-1}$ do not reach this threshold, with the exception of (135°C, 500 $J\ g^{-1}$, 90 $kJ\ mol^{-1}$). These low self-heating rates imply extremely slow reaction, so that the complete course of thermal runaway would take several days.

Kinetic parameters (E_a, k_0) are most significant factors influencing the self-heating rate at given time or temperature. However, they appear to be the key deficiency of this simplified model. On one hand, E_a is measured in a highly indirect manner, with several assumptions underpinning the calculated result. On the other hand, k_0 is determined iteratively (cf. subsection 6.1.3.3). With no experimental data behind the parameter, it is not possible to estimate in what range would it have to be varied. Initial course of aged cells' experimental exotherms implies either an entirely different reaction mechanism, due to growth of SEI as consequence of ageing; or a lower k_0.

6.2.2.2 Entire model

Additional set of parameters pertaining the cathode reaction comes into consideration for the entire model. Kinetic parameters $E_{a,Cath}$ and $k_{0,Cath}$ play a similar role as in case of anode reaction. They bear the key contribution to determining the maximum resulting self-heating rate and also at which time or temperature does system exceed the critical self-heating rate as defined by equation (6.10) on page 89. Cathode decomposition is nonetheless assumed to follow slightly different mechanism as a self-catalytic mixed order reaction, meaning that its rate declines slower over the course of conversion.

For modeled cathode reaction to occur, the cell has to reach onset temperature $T_{on,Cath}$, utilizing anode reaction enthalpy. If this condition is met, the actual value of $T_{on,Cath}$ or the difference $T_{on,Cath} - T_{on}$ do not necessarily have a significant impact on the course of the resulting exotherm, ceteris paribus. This is because activation energy of cathode decomposition is significantly higher than that of the anode. Resulting self-heating rate at given time or temperature is driven mainly by the kinetic term $exp(-\frac{E_a}{RT})$, whose value differs by more than an order of magnitude at the given difference in activation energies for anode and cathode.

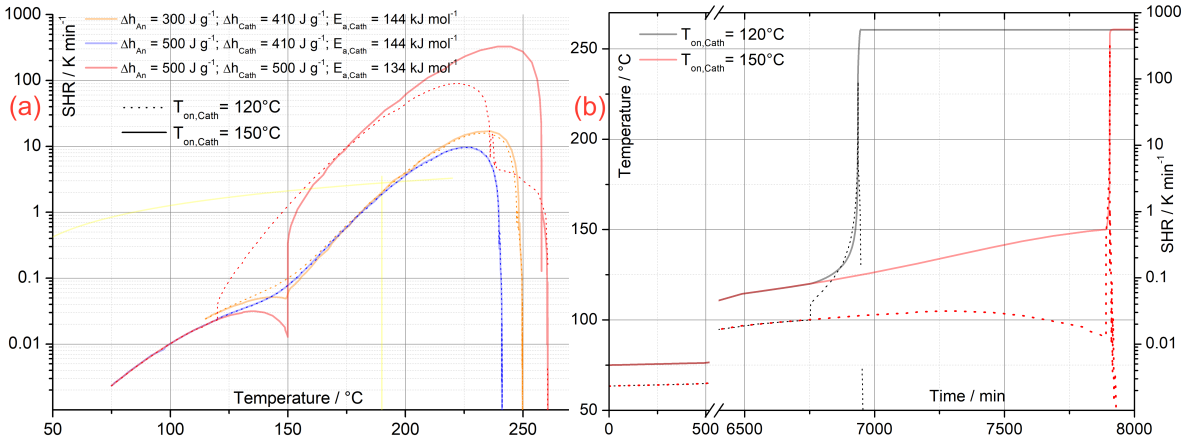

Figure 6.5: (a) Comparison of different calculated exotherms with $T_{on,Cath}$ set to 150°C or 120°C. (b) Detailed view of temperature and SHR course over time for the pair ($\Delta h_{An} = \Delta h_{Cath} = 500\ J\ g^{-1}$, $E_{a,Cath} = 134\ kJ\ mol^{-1}$). T_{on} for each exotherm is evident from the plot, and other parameters are at initial values (cf. Table 6.2)

Few examples are illustrated in Figure 6.5(a) by adjusting $T_{on,Cath}$ from 150°C to 120°C. For initial set of parameters (stated in Table 6.2 on page 87; orange curves in Figure 6.5), just a small discrepancy in exotherm curves is seen in the interval between 135°C to 160°C. The pair of exotherms with $T_{on} = 75°C$ and $\Delta h_{An} = 500\ J\ g^{-1}$ (blue curves) is perfectly overlapping. These two pairs of exotherms cross the state-of-no-return boundary at exactly same temperature and SHR values. They also reach equal maximum SHR, at same temperature. On the other hand, more pronounced differences can be observed between the third pair (red curves) of exotherms, with parameters $\Delta h_{An} = \Delta h_{Cath} = 500\ J\ g^{-1}$, $E_{a,Cath} = 134\ kJ\ mol^{-1}$. Lower activation energy and higher reaction enthalpy of cathode decomposition lead to more pronounced discrepancy (one order of magnitude) between the two exotherms in the interval 120°C - 160°C. However, both exotherms still cross the SHR state-of-no-return curve at roughly same temperature. Figure 6.5(b) elucidates the thermal runaway for latter two sets of parameters in more detail:

- Difference in temperature and SHR profiles is only seen after 6753 min (112.5 h) as the temperature of 120°C is reached.
- The overall duration of the reaction is expectedly shorter with $T_{on,Cath} = 120°C$, where final temperature is reached at 6947 min. With $T_{on} = 150°C$, final temperature is reached at 7931 min, which is 16.4 h later.
- Nevertheless, simulation with $T_{on} = 150°C$ reaches higher maximum SHR (327 $K\ min^{-1}$ vs. 90 $K\ min^{-1}$), due to the fact that cathode decomposition is occurring in the higher temperature range.

The above discussed role of the cathode decomposition temperature has important implications on understanding and quantifying the safety properties of cathode materials. Anode decomposition generally occurs at lower temperature, and is characterised by faster kinetics

that is less temperature-dependent in comparison to cathode decomposition. In present experimental work (see section 4.2), this is manifested by consistently lower activation energies for anode decomposition, as compared to cathode. Therefore, in evaluating the contribution of cathode's thermal properties to cell safety, $T_{on,Cath}$ shall not be interpreted as a single-point property defining the thermal stability. Provided that cathode reaction is expected to occur under given real-life circumstances, such as overheating, short circuit, overcharge, and mechanical abuse, it is more important to focus on enthalpy and kinetics of the cathode's decomposition reaction. As simulations illustrated by Figure 6.5(a) demonstrate, it is the combination of fast reaction kinetics and higher reaction enthalpy, and not the cathode onset temperature, that pushes the cell's self-heating rate above the certain level (herewith arbitrarily defined as state-of-no-return) at relatively low temperature, way below the point of separator collapse.

Knowing the overall onset temperature of cell's self-heating (T_{on}), determined by anode, helps defining the safe operation temperature of the cell. In case of cathode decomposition, it is however more important to understand its dynamics once the cell's thermal runaway has already started, rather than a single-point temperature threshold. This is relevant for two reasons:

- Significant variation in cathode decomposition kinetics have been observed experimentally, in terms of differences in calculated Arrhenius activation energy:

  As a consequence of ageing (Figure 4.10, p. 44)

  As a result of surface area / particle size variation (Figure 5.9, p. 57)

  Between coated and non-coated cathode particles (Figure 5.20, p. 73)

- Determination of cathode decomposition onset is not a clear-cut process, and it depends on methodology: For example, when using TGA, it may be affected by the choice of temperature ramp β. Also, presence or absence of electrolyte affects the result.

Selected calculated isotherms are compared with experimental HWS data of fresh and aged cells, summarized in Figure 6.6. This comparison shows the role of kinetic and thermodynamic parameters in the model. Reaction enthalpies $\Delta h_{Cath} + \Delta h_{An}$ and onset temperature T_{on} determine maximum temperature reached. However, kinetic parameters play the key role in determining the SHR, and thus the rate of thermal runaway. For example, the simulation with initial parameters from Table 6.2 reaches its end temperature after 18.5 hours. Black curve, denoting the simulation with high enthalpies and lower activation energies, reaches its end temperature in less than 5 hours. Blue curve, with higher activation energies and other parameters equal to black curve, implies a process lasting almost 5 months. It shall be noted that in real-life, non-adiabatic conditions, a very slow heat generation would be unlikely to lead towards completion of thermal runaway, as heat dissipation would easily compensate the generated heat.

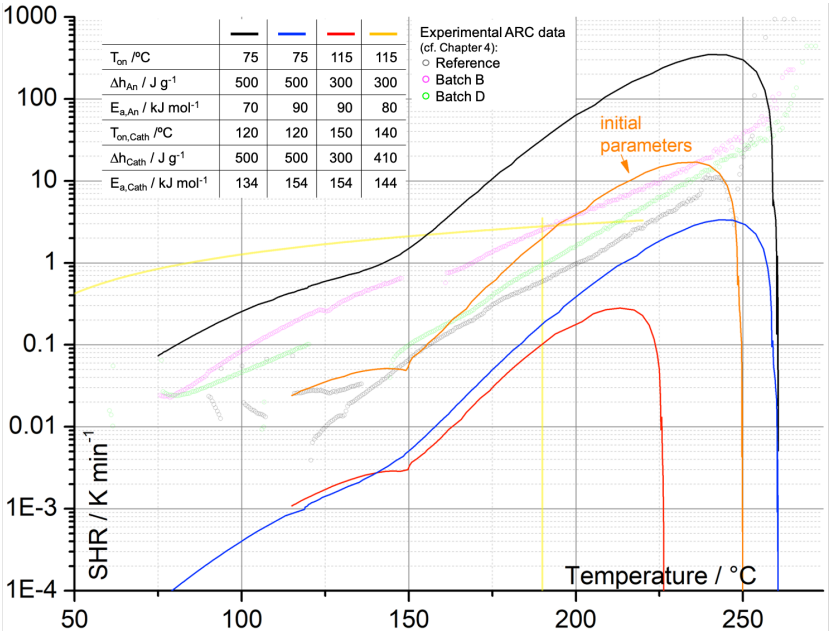

Figure 6.6: Comparison of different calculated exotherms with experimental data from section 4.2.2

As discussed in the beginning of this chapter, present simplified model does not contain anode-cathode reaction caused by internal short circuit, or ignition of electrolyte by oxygen released from the cathode. Therefore, simulated results beyond the separator collapse temperature (estimated to 190°C) are not expected to match actual cell behaviour. Reaching this temperature, or the self-heating rate as defined in section 6.2.1, is therefore considered as point of no return, and can be used to compare various experimental data sets and simulation results between each other. With initial parameters, the system would reach the separator collapse temperature 1063 min after onset. SHR at that point would amount to 2 $K\ min^{-1}$. Two sets of parameters with higher activation energies would reach separator collapse temperature after 142 days and at 0.2 $K\ min^{-1}$ (blue curve), or after 14 days and at 0.1 $K\ min^{-1}$ (red curve). On the other hand, set of parameters with low activation energies (black curve), reaches the critical self-heating rate of 2.23 $K\ min^{-1}$ after 286.5 min at 155.5°C. From there, less than six minutes are needed to reach the separator collapse temperature.

7 Summary

7.1 Conclusions

7.1.1 Ageing and safety

Cycle ageing causes not only structural changes to electrode materials, but also imbalance between the electrodes. This significantly affects cells' thermal behaviour even at normal operating conditions. While the impact on discharge capacity and cyclic efficiency may appear low, the heat generated per unit electric work during discharge of aged cell increases more than two-fold even at moderate current. Therefore, safe operation window of aged cells (e.g. those repurposed for a so-called second life application) has to be amended to reflect these changes.

Cycle ageing was shown to have ambivalent overall effect on cell safety. For cells' thermal stability, this ambivalence is manifested by two phenomena observed in aged cells compared to non-aged reference:

1. Earlier onsets of self heating reactions and thermal runaway: This is a *destabilizing* effect on cells' thermodynamic stability.
2. Slower runaway reactions and lower self-heating rates: This is a *stabilizing* effect on kinetics of decomposition reactions in aged cells.

This two phenomena are observed in two key reactions of thermal runaway:

1. Anodic SEI decomposition, which starts at lower temperature, but also reaches lower maximum rate in case of aged cells
2. Electrolyte ignition and oxidation of carbon anode by O_2 released from NCM: Severely aged cathodes decompose at roughly equal temperature, but release less O_2 compared to cathodes from fresh or mildly aged cells.

Similar ambivalence is observed in terms of mechanical safety. Aged cells would break down and burn at lesser extent of mechanical abuse, but also react less explosively and reach lower maximum temperature. This is nevertheless additionally affected by the cell type and format.

7.1.2 Surface area and thermal stability of $LiCoO_2$

Thermal stability of charged $LiCoO_2$ cathodes is highly dependent on surface area / particle size of active material. This is reflected by following observations:

- Onset temperature of cathode decomposition decreases with increasing $LiCoO_2$ surface area, which means that smaller active material particles are thermodynamically less stable
- Total mass loss during decomposition is proportional to $LiCoO_2$ surface area
- Activation energy of cathode decomposition appears to decrease with increasing $LiCoO_2$ surface area, which implies faster rate of decomposition reaction for smaller active material particles at equal temperature.

Based on characterization of decomposition products, it is hypothesized that the decomposition reaction follows different mechanisms on surface of the active material particles and in their bulk. These two mechanisms yield different decomposition products: layered (R-3m) $LiCoO_2$ in the bulk, and rock-salt (Fm-3m) $Li_yCo_{2-y}O_2$ on the particles' surface.

7.1.3 Overlithiated oxide materials and their safety

Characteristic structural and electrochemical properties of the overlithiated oxide active materials significantly affect their thermal stability. Decomposition behaviour is strongly influenced by activation of the Li_2MnO_3 component and participation of oxygen in the underlying redox reaction of charge and discharge. Therefore, OLO thermal stability is not dependent only on degree of de-lithiation (i.e. state of charge), but also on oxidation states of individual transition metals and presence of unstable oxygen in the structure. This leads to reduced thermal stability in comparison to conventional NCM.

Coating of OLO particles partly improves cyclic performance of OLO cathodes. It results in a modified activation of the LMO domain during the first charge. In initial few cycles, it also improves thermal stability by increasing the onset temperature and activation energy of thermal decomposition. However, it also further facilitates certain processes in active material's structure during cycling. This presumably leads to accumulation of additional unstable oxygen in the structure and results in a violent thermal decomposition, characterized by high reaction enthalpy and copious release of gaseous O_2 from active material particles.

Thermal stability of OLO cathodes is additionally affected by two microstructural aspects:

1. Particle size and surface area
2. Distribution of LMO and NCM structural domains between bulk and surface. This is controlled by choice of lithium source for material synthesis (Li_2CO_3 vs. LiOH).

In the investigated range of active material surface area ($1.90\ m^2\ g^{-1} \leqslant a_s \leqslant 4.14\ m^2\ g^{-1}$),

the latter aspect plays the decisive role in determining thermal stability of the OLO cathodes. Cathodes with higher concentration of LMO phase at the active material particles' surface are thermally more stable in the initial charge-discharge cycles. At comparable surface areas, they exhibit lower onset temperatures and less O_2 release during decomposition. This difference in thermal stability is however reduced after longer cycling. Sun et al. [118] have reported analogous phenomena with core-shell concentration gradient NCM particles. Targeted utilization of such concentration gradients in active material particles has a potential of combining higher energy with improved safety.

Both Li_2CO_3 and LiOH are being utilised as lithium sources for large-scale production of cathode materials [119]. It is therefore important to properly evaluate their impact on performance and safety when choosing the precursors for active material synthesis.

7.1.4 Relevance of experimentally determined parameters

Simplified mathematical model was implemented to investigate impact of varying the key thermodynamic and kinetic parameters of electrode active materials pertaining the thermal stability of a lithium-ion battery cell. Results of the conducted simulation underline higher relevance of two parameters describing materials' thermal properties:

1. Reaction kinetics, in present model described by a (fixed) reaction model and (variable) Arrhenius activation energy. It determines the rate of reactions and heating rate of the cell
2. Reaction enthalpies: Their sum indicate the amount of energy that can be released towards self-heating of the cell.

Onset temperatures of individual reactions are important indicators of active materials' thermal stability, since they enable a reasonable comparison between various active materials. However, they may play a less significant role in a holistic evaluation of cell's thermal runaway using a thermal model.

More accurate determination of key kinetic and thermodynamic data, such as reaction models and enthalpies, is therefore the key toward predicting thermal stability of the cells based on their active material combination.

7.1.5 Validation of hypotheses set in Section 2.6

Impact of ageing on cell safety is both stabilizing and de-stabilizing in terms of cells' thermal stability. Both effects are overlapping and may be affected by ageing conditions.

Ambivalence of ageing processes in terms of their impact on cells' thermal stability and mechanical safety has been proven experimentally. Ageing conditions (in present work, number of cycles and charging current) are shown to affect safety-relevant properties of aged cells in

their own different ways. For aged cells at equal SOH, longer duration of cyclic ageing leads to a greater growth of SEI. This leads to increased reaction enthalpy of SEI decomposition.

Particle size and surface area of active materials play crucial role in balancing performance and safety of a given electrochemical Li-ion system. Optimum can be find in respect of both aspects and system can be optimized within given boundary conditions.

Surface area is shown to play key role in thermal stability of LCO. There is however no compromise value of surface area found in terms of safety, since increased higher surface leads to reduced thermal stability across the entire range of investigated LCO materials. That implies a trade-off between safety and performance in the interval from minimum feasible surface area and optimum particle size in terms of performance.

Over-lithiated layered-layered oxide cathode materials posses an additional safety issue due to oxide oxidation during charge. This process follows different reaction mechanism at particles' surface and in bulk material. Variations in surface area / particle size and structural composition of active materials therefore have an impact on thermal stability. Mechanisms of surface area influences are different and more complex than in case of layered transition metal oxides such as LCO.

In case of OLO cathodes, there are structural properties that affect thermal stability more significantly than active material surface area, due to complex electrochemical properties of this cathode type.

Stability level of lithium-ion battery materials and cells, which are by their nature meta-stable systems, is reflected by kinetic and thermodynamic contribution to apparent instabilities. Scope of these contributions is strongly dependent on electrode structure and composition, and can be assessed by proper methods.

Results reported in present work distinguish between thermodynamic and kinetic aspects to thermal stability of electrodes and by extension, safety of lithium-ion cells. Particularly the results from aged 18650 cells clearly shows differences in thermodynamic and kinetic stability. It is however not always possible to separate the two phenomena. In addition, estimating kinetic parameters, such as Arrhenius activation energy, is generally less accurate than measuring reaction enthalpies and temperature profiles.

7.2 Outlook

Present work represents a modest contribution towards understanding how microstructure and composition of active materials, especially cathode materials, affect safety of lithium-ion battery cells. Driven by demand for renewable energy storage and electric mobility, the field of lithium-ion batteries develops rapidly. This means continuous implementation of improved active materials and repeated modifications of these materials. As safety remains one of the main challenges lithium-ion batteries are facing, this also requires research community continuously deepening the understanding of cells' safety properties.

Results presented and discussed in the present work offer a starting point for additional investigations to further the knowledge of active materials' safety-critical properties and understanding of their complex influence on stability of lithium-ion cells.

7.2.1 Proposed work and improvements on active material investigations

Understanding of structural changes in active material during electrode operation as well as its thermal decomposition needs to be improved. Deeper insight into these changes would help validate the hypotheses set based on the reported results, such as:

- Formation of rock-salt phase $Li_yCo_{2-y}O_2$ on the surface of smaller $Li_{1-x}CoO_2$ particles during decomposition
- Increased concentration of unstable oxygen during cycling of certain over-lithiated oxide materials:

  PI-coated OLO

  OLO with increased concentration of LMO phase in the bulk of the particles

For that purpose, structural spectroscopic analyses such as XRD, XANES, SXAS should be conducted in-operando during charge and discharge of the cathodes, and in-situ during the thermal decomposition. In addition, differential electrochemical mass spectrometry on OLO cathodes with different structure and coatings would give additional insights of oxygen redox processes affecting thermal stability.

There is also plenty of improvement potential in preparation of active material powders with modified microstructural properties:

- Narrower particle size distributions can be attempted by iteratively combining processes of annealing, ball milling, and re-annealing of milled particles.
- Improved particle coating processes may provide better performance and cyclic stability of OLO. One such process may involve polyimide / carbon black nanocomposite [107].

7.2.2 Towards better understanding of cell safety

The approach towards investigating the relationship between cell-level ageing and safety reported in present work can be extended to:

- Other cell chemistries - particularly the electrode combinations that cause the cathode to play a more significant role in thermal behaviour, such as cells with nickel-rich cathodes (NCA, NCM 811) or LTO anodes.
- Other cell formats - soft laminate pouch cells are increasing their market share across many applications. Electrodes in these cells exhibit significant thickness changes [120]. This may impact ageing processes and the way how these processes interfere with safety and thermal stability of the cell.

Mathematical model used to simulate the effect of experimentally determined parameters and their variation on cell's thermal behaviour can be refined to reflect the complexity of consecutive reactions constituting SEI decomposition, as well as electrolyte reaction at higher temperature. Validation of the model using tailored lab-scale or prototype cells with modified active materials would be an extensive effort. However, it would lend much needed credibility to the approach and to conclusions drawn from it.

The entire sensitivity analysis of kinetic and thermodynamic parameters could also be repeated on more complex and multi-dimensional thermal models that cover realistic cell abuse conditions, such as overcharge or internal short circuit.

Acronyms, Abbreviations, Subscripts

amb ..... Ambient
ch ..... Charge
ct ..... Charge transfer
disch ..... Discharge
irrev ..... Irreversible
ohm ..... Ohmic
rev ..... Reversible
a.u. ..... Arbitrary unit
ar ..... As received
ARC ..... Accelerating rate calorimetry
BET ..... Brunauer-Emmett-Teller isotherm (for adsorptive determination of surface area)
CCV ..... Closed circuit voltage
CPE ..... Constant phase element
DEC ..... Diethyl carbonate
DMC ..... Dimethyl carbonate
DOD ..... Depth of discharge (opposite of SOC)
DSC ..... Differential scanning calorimetry
DTG ..... Differential thermogravimetry - First-order derivative of TGA
EC ..... Ethylene carbonate
EIS ..... Electrochemical Impedance Spectroscopy
EOL ..... End of life
FE-SEM ..... Field emission scanning electron microscope
FEC ..... Fluoroethylene carbonate
HWS ..... Heat-Wait-Search
IRC ..... Irreversible capacity
LCO ..... Lithium cobalt oxide, $LiCoO_2$
LFP ..... Lithium iron phosphate, $LiFePO_4$
LMO-NCM ..... Lithium manganese oxide - lithium nickel cobalt manganese oxide, $aLi_2MnO_3-(1-a)Li[Ni_xCo_{1-2x}Mn_x]O_2$ (see OLO)

LMO-s ..... Lithium manganese oxide, spinel, $LiMn_2O_4$
LTO ..... Lithium titanate, $LiTi_5O_{12}$
MCMB ..... Mesocarbon microbeads
MFK ..... Model-free kinetics
MS ..... Mass Spectrometry
NCA ..... Lithium nickel cobalt aluminium oxide, $LiNi_{0.8}Co_{0.15}Al_{0.05}O_2$
NCM ..... Lithium nickel cobalt manganese oxide, $Li[Ni_kCo_lMn_m]O_2$; $k + l + m = 1$
OCV ..... Open circuit voltage
OLO ..... Overlithiated (layered-layered) oxide
PE ..... Polyethylene
PP ..... Polypropylene
PVDF ..... Polyvinylidene difluoride
Ref. ..... Reference
SEI ..... Solid-electrolyte interphase
SHR ..... Self-heating rate, $\frac{dT}{dt}$
SOC ..... State of charge
SOH ..... State of health
TEM ..... Transmission electron microscope
TGA ..... Thermogravimetric analysis
TM ..... Transition metal

Index of Symbols

α ..... Conversion [-]
$\bar{x}$ ..... Average value of x
β ..... Temperature rate (thermal analysis) [$K\ min^{-1}$]
ΔH ..... Reaction enthalpy [J]
Δh ..... Specific enthalpy of reaction [$J\ g^{-1}$]
ΔS ..... Specific entropy of reaction [$J\ mol^{-1}\ K^{-1}$]
$\dot{Q}$ ..... Heat flow [W]
η ..... Efficiency [-]
Φ ..... Phi-factor (Degree of thermal inertia)
a_s ..... Surface area [$m^2\ g^{-1}$]
C ..... Capacity [Ah]
C_p ..... Heat capacity [$J\ K^{-1}$]
c_p ..... Specific heat capacity [$kJ\ kg^{-1}\ K^{-1}$]
E ..... Electric energy [Wh]
E_a ..... Activation energy [$kJ\ mol^{-1}$]
F ..... Faraday constant [96485 $As\ mol^{-1}$]
$f(\alpha)$ ..... Reaction model [-]
I ..... Current [A]
k_0 ..... Pre-exponential factor [s^{-1}]
k_{HT} ..... Heat transfer coefficient [$W\ m^{-2}\ K^{-1}$]
m ..... Mass [kg]
m/z ..... Mass number (mass spectrometry): molar mass of ionic fragment in $g\ mol^{-1}$ divided by ionisation state [-]
P ..... Electric power [W]
p ..... Pressure [bar]
Q ..... Heat [J]
R ..... Resistance [Ω]
R_m ..... Gas constant [8.314 $J\ mol^{-1}\ K^{-1}$]
T ..... Temperature [$^\circ C$]
t ..... Time [s]

T_{on} ..... Onset temperature of thermal runaway [$^{\circ}C$]
U ..... Voltage [V]
w ..... Mass fraction [-]
z ..... Number of exchanged electrons ($z = 1$ for Li-ion systems) [$-$]

List of Figures

1.1 Comparison of energy storage capacity and combustion energy of a 2.5 Ah 18650 Li-ion cell. Estimation based on [15]. 4
1.2 Scheme of the working concept for the research in the present thesis 6

2.1 Microscopical representation of a segment in a typical Li-ion cell 8
2.2 Typical thermal runaway profile of a lithium-ion cell with carbon-based anode and layered lithium - transition metal cathode. 11
2.3 Schematic representation of ageing phenomena in a lithium-ion cell. Components not to scale 15
2.4 Crystal structure of lithium-rich cathode materials. Image copied from [66]. . . 18
2.5 Characteristic first cycle voltage profile of an OLO cathode vs. $Li|Li^+$ 18

3.1 Scheme of a self-made pouch cell 25
3.2 Diagram of the equivalent circuit model for fitting of EIS data [76] 27
3.3 Scheme of the ARC experimental setup (above), illustration of heat-wait-search (HWS) analysis (below) 30
3.4 Schematic representation of ARC test setups for (a) charging/discharging the cell and (b) heat capacity determination 31
3.5 Experimental setup for blunt nail indentation test 33

4.1 SEM images of anode from reference and aged (Batch C) cell (30000x magnified) 36
4.2 SEM images of cathode from reference and aged (Batch C) cell (magnification above: 5000x, below: 50000x) 36
4.3 Impedances of cells at various SOC, as measured by EIS [79] 37
4.4 Calculated change of entropy for new and aged 18650 cells [79] 38
4.5 Temperature increase and total heat flow as function of discharge capacity during discharge at adiabatic conditions (ARC). The reversible heat flow below is estimative calculation based on equations (3.1) and (4.1) [79] 39
4.6 Cumulative heat released by cells during adiabatic discharge and discharge efficiency. Share of reversible heat is an estimative calculation based on equations (3.1) and (4.1) [79] 40
4.7 ARC thermal runaway profiles of electrolyte-soaked anodes (left). DSC curves of electrolyte-soaked anodes (right, $\beta = 10$ K min^{-1}) 40

4.8 TGA of electrolyte-soaked anodes and MS of evolved gases (left, $\beta = 5$ K min^{-1}). Arrhenius activation energy of anode decomposition reaction (see section 3.3.1) 42
4.9 ARC thermal runaway profiles of electrolyte-soaked cathodes (left). DSC curves of washed and dried cathodes (right, $\beta = 10$ K min^{-1}) 44
4.10 TGA of washed and dried cathodes and MS of evolved gases (left, $\beta = 5\ K\ min^{-1}$). Arrhenius activation energy of cathode decomposition reaction (see section 3.3.1) 44
4.11 Thermal runaway profiles of fully charged cells in ARC 45
4.12 Results of blunt nail indentation test. In lower graph, full line represents nail temperature, and dashed line cell surface temperature. 47

5.1 As-received (a) and subsequently milled $LiCoO_2$ (b - LCOm3, c - LCOm5, d - LCOm7 [67] 50
5.2 Sol-gel synthesized $LiCoO_2$: SEM images (left) and Raman spectra (right, [98]) 50
5.3 TGA profiles of $Li_{0.5}CoO_2$ charged electrodes under heating rate of 5 K min^{-1} . 51
5.4 Decomposed mass fraction at 400°C for charged cathodes and chemically de-lithiated $Li_{0.5}CoO_2$ [67] 51
5.5 DSC curves of $Li_{0.5}CoO_2$ charged electrodes under heating rate of 10 K min^{-1} . 52
5.6 Evolved gases analysis (MS) during TGA of charged LCO cathodes 53
5.7 Left: TGA curves of chemically de-lithiated $Li_{0.5}CoO_2$: alone (thin lines), with acetylene black (dashed lines), with PVDF (dotted lines). Thick lines represent charged cathodes [67]. Right: First-order derivative (DTG) of TGA curves for pure $Li_{0.5}CoO_2$, and MS signal (m/z=32) related to same analysis 54
5.8 XRD spectra of decomposed cathodes (heated up to 600°C) compared to standards for $LiCoO_2$ (layered, spinel and rock salt), Co_3O_4 and CoO. Absence of R-3m $LiCoO_2$-related peaks is obvious for the two cathodes with higher surface area. 55
5.9 Calculated Arrhenius activation energy at different values of conversion for decomposition of charged LCO cathodes 57
5.10 Left: Cycling profile of OLOar cathode vs. Li|Li$^+$ ($I = 25\ mA\ g^{-1}$). Squares and crosses indicate points at which washed and dried cathodes were analysed. Right: SEM images of OLOar under different magnifications. 59
5.11 TGA (left) and DSC (right) curves of OLOar cathodes [72], $\beta = 5\ K\ min^{-1}$ . . 60
5.12 Mass spectrometry data related to evolution of O_2 and CO_2 during thermal decomposition 62
5.13 XRD of OLOar powder and cathodes before (a) and after (b) thermal decomposition in TGA/DSC at various states of charge in the first and second cycles as indicated in (c). All spectra are normalized to the highest peak intensity in the respective spectrum [72] 63
5.14 TEM images of as-received LMO-NCM (OLOar, left) and the same material coated with a polyimide layer (OLO-PI, right) 65

5.15 Charge and discharge voltage profiles for twenty cycles; OLOar and OLO-PI cathodes ($I = 25\ mA\ g^{-1}$) 66
5.16 Comparison of TGA (left) and DSC (right) curves for OLOar and OLO-PI cathodes after first and second charge ($\beta = 5\ K\ min^{-1}$) 67
5.17 Comparison of TGA (left) and DSC (right) curves for OLOar and OLO-PI fully charged (4.8 V) cathodes after ten and twenty cycles ($\beta = 5\ K\ min^{-1}$) 68
5.18 Mass spectrometry profiles related to evolution of O_2 ($m/z = 32$) during thermal decomposition of OLOar and OLO-PI cathodes. All cathodes at 10 and 20 cycles are charged to 4.8 V 69
5.19 XRD spectra of decomposed OLOar and OLO-PI cathodes. All spectra are normalized to the highest peak intensity in the respective spectrum. 72
5.20 Arrhenius activation energy of thermal decomposition of fully charged OLOar and OLO-PI cathodes in second cycles 73
5.21 ARC exotherm profiles of fully charged OLO cathodes in second cycles. Cathode powders are soaked in electrolyte (1 M $LiPF_6$ in 1:1 FEC/DEC) in the ratio of 0.5 g of electrolyte per 1 g powder. 74
5.22 SEM images of synthesized OLO materials 75
5.23 Comparison of synthesized materials' electrochemical performance: First cycle discharge (a) and charge (b) profiles, (c) charge and discharge capacities in first 20 cycles, (d) Coulombic efficiencies for first 20 cycles. $I = 25\ mA\ g^{-1}$ 76
5.24 TGA curves for decomposition of cathodes charged in first, second, and twentieth cycle ($\beta = 5\ K\ min^{-1}$) 77
5.25 TGA curves for decomposition of cathodes charged to 150 $mAh\ g^{-1}$ in first and second cycle ($\beta = 5\ K\ min^{-1}$) 78
5.26 Mass spectrometry profiles related to evolution of O_2 ($m/z = 32$) during thermal decomposition of OLO-C and OLO-H cathodes charged in first two cycles . 79
5.27 Mass spectrometry profiles related to evolution of O_2 ($m/z = 32$) during thermal decomposition of OLO-C and OLO-H cathodes charged after 20 cycles . . 81
5.28 ARC exotherm profiles of fully charged cathodes in second cycles. Cathode powders are soaked in electrolyte (1 M $LiPF_6$ in 1:1 FEC/DEC) in the ratio of 0.5 g of electrolyte per 1 g powder. 82

6.1 Block diagram of the proposed model 86
6.2 Comparison between experimental ARC results of fresh model cell and initial model calculation 88
6.3 Schematic representation of the criteria for state of no return 90
6.4 Results of model calculations for anode reaction only with parameters from Table 6.3 91

6.5 (a) Comparison of different calculated exotherms with $T_{on,Cath}$ set to 150°C or 120°C. (b) Detailed view of temperature and SHR course over time for the pair ($\Delta h_{An} = \Delta h_{Cath} = 500\ J\ g^{-1}$, $E_{a,Cath} = 134\ kJ\ mol^{-1}$). T_{on} for each exotherm is evident from the plot, and other parameters are at initial values (cf. Table 6.2) 93
6.6 Comparison of different calculated exotherms with experimental data from section 4.2.2 95

List of Tables

2.1 Hypothetical evaluation of ageing effects with regards to their presumed impact on thermal stability . . . 16
2.2 Overview of experiments on aged and new cells . . . 19

3.1 Input materials for sol-gel synthesis of $LiCoO_2$ . . . 22
3.2 Milling parameters and resulting surface area of milled $LiCoO_2$ . . . 24
3.3 Overview of electrolytes used in self-made pouch cells . . . 25

4.1 Cycle ageing results of 18650 cells ($U_{disch} = \frac{E_{disch}}{C_{disch}}$) . . . 35

5.1 Overview of available $LiCoO_2$ materials. . . . 49
5.2 First peak area of DSC curves for synthesised LCO from Figure 5.5, [$J\ g^{-1}$] . . 52
5.3 Mass losses (normalised to mass of LCO in respective samples) at 600°C [67] . 54
5.4 Summarised TGA and DSC key data for decomposition of OLOar-based cathodes 61
5.5 Comparison of TGA and DSC results for decomposition of OLOar and OLO-PI cathodes . . . 68
5.6 Overview of synthesized OLO samples and their BET surface area . . . 75
5.7 Summary of TGA onset temperatures in °C . . . 78

6.1 Parameters of the model cell . . . 85
6.2 Initial parameters for model calculation . . . 87
6.3 Parameter variation matrix for anode . . . 91

Bibliography

[1] J. B. Goodenough, "Electrochemical energy storage in a sustainable modern society," *Energy & Environmental Science*, vol. 7, no. 1, pp. 14–18, 2014.

[2] World Bank, *World Development Indicators 2015*. International Capital and Economic Development; World Development Indicators, The World Bank, Apr. 2015.

[3] International Energy Agency Statistics, "Renewables information 2014." IEA Statistics, International Energy Agency.

[4] F. Beck and E. Martinot, "Renewable Energy Policies and Barriers," in *Encyclopedia of Energy*, pp. 365–383, 2004.

[5] R. Banos, F. Manzano-Agugliaro, and F. G. Montoya, "Optimization methods applied to renewable and sustainable energy: A review," *Renewable and Sustainable Energy Reviews*, vol. 15, pp. 1753–1766, 2011.

[6] Z. Yang, J. Zhang, M. Kintner-Meyer, X. Lu, D. Choi, J. P. Lemmon, and J. Liu, "Electrochemical energy storage for green grid," *Chemical Reviews*, vol. 111, pp. 3577–3613, 2011.

[7] A. Gil, M. Medrano, I. Martorell, A. Lázaro, P. Dolado, B. Zalba, and L. F. Cabeza, "State of the art on high temperature thermal energy storage for power generation. Part 1—Concepts, materials and modellization," *Renewable and Sustainable Energy Reviews*, vol. 14, pp. 31–55, Jan. 2010.

[8] M. Winter and R. J. Brodd, "What Are Batteries, Fuel Cells, and Supercapacitors?," *Chemical Reviews*, vol. 104, pp. 4245–4270, Oct. 2004.

[9] K. V. Kordesch and J. C. T. de Oliveira, "Fuel Cells," in *Ullmanns Encyclopedia of Industrial Chemistry*, pp. 55–82, 1985.

[10] D. Linden, "Basic Concepts," in *Handbook of batteries*, McGraw-Hill, 2002.

[11] R. J. Brodd, "Synopsis of the Lithium-Ion Battery Markets," in *Lithium-Ion Batteries* (M. Yoshio, R. J. Brodd, and A. Kozawa, eds.), pp. 1–7, New York, NY: Springer, 2009.

[12] D. W. Green, *Perry's Chemical Engineers' Handbook*. New York: McGraw Hill Professional, 8th edition ed., Oct. 2007.

[13] B. Nykvist and M. Nilsson, "Rapidly falling costs of battery packs for electric vehicles," *Nature Climate Change*, vol. 5, pp. 329–332, Mar. 2015.

[14] A. Barré, B. Deguilhem, S. Grolleau, M. Gérard, F. Suard, and D. Riu, "A review on lithium-ion battery ageing mechanisms and estimations for automotive applications," *Journal of Power Sources*, vol. 241, pp. 680–689, Nov. 2013.

[15] C. Mikolajczak, M. Kahn, K. White, and R. T. Long, *Lithium-ion batteries hazard and use assessment*. Quincy, MA: Springer Science & Business Media, 2012.

[16] R. Stringfellow, D. Ofer, S. Sriramulu, and B. Barnett, "Lithium-ion battery safety field-failure mechanisms," in *218th ECS Meeting*, (Las Vegas), Oct. 2010.

[17] Q. Wang, P. Ping, X. Zhao, G. Chu, J. Sun, and C. Chen, "Thermal runaway caused fire and explosion of lithium ion battery," *Journal of Power Sources*, vol. 208, pp. 210–224, June 2012.

[18] F. Meutzner and M. U. de Vivanco, "Electrolytes - Technology review," in *REVIEW ON ELECTROCHEMICAL STORAGE MATERIALS AND TECHNOLOGY: Proceedings of the 1st International Freiberg Conference on Electrochemical Storage Materials*, pp. 185–195, AIP Publishing LLC, Nov. 2014.

[19] M. Petzl and M. A. Danzer, "Nondestructive detection, characterization, and quantification of lithium plating in commercial lithium-ion batteries," *Journal of Power Sources*, vol. 254, pp. 80–87, May 2014.

[20] K. Kleiner, P. Jakes, S. Scharner, V. Liebau, and H. Ehrenberg, "Changes of the balancing between anode and cathode due to fatigue in commercial lithium-ion cells," *Journal of Power Sources*, vol. 317, pp. 25–34, June 2016.

[21] C.-S. Kim, K. M. Jeong, K. Kim, and C.-W. Yi, "Effects of Capacity Ratios between Anode and Cathode on Electrochemical Properties for Lithium Polymer Batteries," *Electrochimica Acta*, vol. 155, pp. 431–436, Feb. 2015.

[22] B. Scrosati and J. Garche, "Lithium batteries: Status, prospects and future," *Journal of Power Sources*, vol. 195, pp. 2419–2430, May 2010.

[23] D. Aurbach, A. Zaban, Y. Ein-Eli, and I. Weissman, "Recent studies on the correlation between surface chemistry, morphology, three-dimensional structures and performance of Li and Li-C intercalation anodes in several important electrolyte systems," *Journal of Power Sources*, vol. 68, pp. 91–98, 1997.

[24] F. M. Stowell and L. Murnane, *Essentials of Fire Fighting and Fire Department Operations*. Pearson Education, 2013.

[25] Y. Furushima, C. Yanagisawa, T. Nakagawa, Y. Aoki, and N. Muraki, "Thermal stability and kinetics of delithiated LiCoO2," *Journal of Power Sources*, vol. 196, pp. 2260–2263, Feb. 2011.

[26] A. Veluchamy, C.-H. Doh, D.-H. Kim, J.-H. Lee, H.-M. Shin, B.-S. Jin, H.-S. Kim, and S.-I. Moon, "Thermal analysis of Li_xCoO_2 cathode material of lithium ion battery," *Journal of Power Sources*, vol. 189, pp. 855–858, Apr. 2009.

[27] J. Garche and K. Brandt, eds., *Electrochemical Power Sources: Fundamentals, Systems, and Applications*. Li-Battery Safety, Oxford: Elsevier, 1st ed., 2018.

[28] R. Spotnitz and J. Franklin, "Abuse behavior of high-power, lithium-ion cells," *Journal of Power Sources*, vol. 113, pp. 81–100, 2003.

[29] H. H. Lee, C. C. Wan, and Y. Y. Wang, "Thermal Stability of the Solid Electrolyte Interface on Carbon Electrodes of Lithium Batteries," *Journal of The Electrochemical Society*, vol. 151, no. 4, pp. A542–6, 2004.

[30] M. N. Richard and J. R. Dahn, "Accelerating Rate Calorimetry Study on the Thermal Stability of Lithium Intercalated Graphite in Electrolyte. I. Experimental," *Journal of The Electrochemical Society*, vol. 146, pp. 2068–2077, June 1999.

[31] P. Biensan, B. Simon, J. P. Peres, A. De Guibert, M. Broussely, J. M. Bodet, and F. Perton, "On safety of lithium-ion cells," *Journal of Energy Storage*, vol. 81-82, pp. 906–912, Sept. 1999.

[32] G. G. Botte, R. E. White, Z. Z. J. o. P. Sources, Z. Zhang, and 2001, "Thermal stability of LiPF6–EC: EMC electrolyte for lithium ion batteries," *Journal of Energy Storage*, vol. 97-98, pp. 570–575, July 2001.

[33] H. Arai, M. Tsuda, K. Saito, M. Hayashi, and Y. Sakurai, "Thermal Reactions Between Delithiated Lithium Nickelate and Electrolyte Solutions," *Journal of The Electrochemical Society*, vol. 149, no. 4, pp. A401–6, 2002.

[34] I. Belharouak, G. M. Koenig Jr, and K. Amine, "Electrochemistry and safety of Li4Ti5O12 and graphite anodes paired with LiMn2O4 for hybrid electric vehicle Li-ion battery applications," *Journal of Power Sources*, vol. 196, pp. 10344–10350, Dec. 2011.

[35] K. Chen, Z. Yu, S. Deng, Q. Wu, J. Zou, and X. Zeng, "Evaluation of the low temperature performance of lithium manganese oxide/lithium titanate lithium-ion batteries for start/stop applications," *Journal of Power Sources*, vol. 278, pp. 411–419, Mar. 2015.

[36] R. Bernhard, S. Meini, and H. A. Gasteiger, "On-Line Electrochemical Mass Spectrometry Investigations on the Gassing Behavior of Li4Ti5O12 Electrodes and Its Origins," *Journal of The Electrochemical Society*, vol. 161, pp. A497–A505, Jan. 2014.

[37] M. Yoshio, H. Wang, K. Fukuda, T. Umeno, N. Dimov, and Z. Ogumi, "Carbon-Coated Si as a Lithium-Ion Battery Anode Material," *Journal of The Electrochemical Society*, vol. 149, no. 12, pp. A1598–7, 2002.

[38] Y. Li, K. Yan, H.-W. Lee, Z. Lu, N. Liu, and Y. Cui, "Growth of conformal graphene cages on micrometre-sized silicon particles as stable battery anodes," *Nature Energy*, vol. 1, pp. 366–9, Jan. 2016.

[39] M. S. Whittingham, "Lithium Batteries and Cathode Materials," *Chemical Reviews*, vol. 104, pp. 4271–4302, Oct. 2004.

[40] P. Kurzweil and J. Garche, "Overview of batteries for future automobiles," in *Lead-Acid Batteries for Future Automobiles* (J. Garche, E. Karden, P. T. Moseley, and D. A. J. Rand, eds.), Oxford: Elsevier B.V., 2017.

[41] H. Awano, "Development of LiCoO2 Used for Rechargeable Lithium-Ion Battery," in *Lithium-Ion Batteries* (M. Yoshio, R. J. Brodd, and A. Kozawa, eds.), pp. 299–313, Springer Science and Business Media LLC, 2009.

[42] B. L. Ellis, K. T. Lee, and L. F. Nazar, "Positive Electrode Materials for Li-Ion and Li-Batteries," *Chemistry of Materials*, vol. 22, pp. 691–714, Feb. 2010.

[43] G. Hu, W. Liu, Z. Peng, K. Du, and Y. Cao, "Synthesis and electrochemical properties of LiNi0.8Co0.15Al0.05O2 prepared from the precursor Ni0.8Co0.15Al0.05OOH," *Journal of Power Sources*, vol. 198, pp. 258–263, Jan. 2012.

[44] T. Ohzuku and Y. Makimura, "Layered Lithium Insertion Material of LiCo1/3Ni1/3Mn1/3O2 for Lithium-Ion Batteries ," *Chemistry Letters*, vol. 30, no. 7, pp. 642–643, 2001.

[45] H.-J. Noh, S. Youn, C. S. Yoon, and Y.-K. Sun, "Comparison of the structural and electrochemical properties of layered Li[NixCoyMnz]O2 (x = 1/3, 0.5, 0.6, 0.7, 0.8 and 0.85) cathode material for lithium-ion batteries," *Journal of Power Sources*, vol. 233, pp. 121–130, July 2013.

[46] L. de Biasi, A. O. Kondrakov, H. Geßwein, T. Brezesinski, P. Hartmann, and J. Janek, "Between Scylla and Charybdis: Balancing Among Structural Stability and Energy Density of Layered NCM Cathode Materials for Advanced Lithium-Ion Batteries," *The Journal of Physical Chemistry C*, vol. 121, pp. 26163–26171, Nov. 2017.

[47] J. Zheng, T. Liu, Z. Hu, Y. Wei, X. Song, Y. Ren, W. Wang, M. Rao, Y. Lin, Z. Chen, J. Lu, C. Wang, K. Amine, and F. Pan, "Tuning of Thermal Stability in Layered Li(NixMnyCoz)O2," *Journal of the American Chemical Society*, vol. 138, pp. 13326–13334, Oct. 2016.

[48] G. Amatucci and J.-M. Tarascon, "Optimization of Insertion Compounds Such as LiMn2O4 for Li-Ion Batteries," *Journal of The Electrochemical Society*, vol. 149, no. 12, pp. K31–17, 2002.

[49] Y.-S. Duh, Y.-L. Chen, and C.-S. Kao, "Thermal stability of ethylene carbonate reacted with delithiated cathode materials in lithium-ion batteries," *Journal of Thermal Analysis and Calorimetry*, vol. 127, pp. 995–1007, May 2017.

[50] J. Vetter, P. Novák, M. R. Wagner, C. Veit, K. C. Möller, J. O. Besenhard, M. Winter, M. Wohlfahrt-Mehrens, C. Vogler, and A. Hammouche, "Ageing mechanisms in lithium-ion batteries," *Journal of Power Sources*, vol. 147, pp. 269–281, Sept. 2005.

[51] M. Broussely, P. Biensan, F. Bonhomme, P. Blanchard, S. Herreyre, K. Nechev, and R. J. Staniewicz, "Main aging mechanisms in Li ion batteries," *Journal of Power Sources*, vol. 146, pp. 90–96, Aug. 2005.

[52] M. Fleischhammer, T. Waldmann, G. Bisle, and B. I. Hogg, "Interaction of cyclic ageing at high-rate and low temperatures and safety in lithium-ion batteries," *Journal of Power Sources*, vol. 274, pp. 432–439, 2015.

[53] A. Friesen, F. Horsthemke, and X. Mönnighoff, "Impact of cycling at low temperatures on the safety behavior of 18650-type lithium ion cells: Combined study of mechanical and thermal abuse testing accompanied by post-mortem analysis," *Journal of Power Sources*, vol. 334, pp. 1–11, 2016.

[54] M. Börner, A. Friesen, M. Grützke, Y. P. Stenzel, G. Brunklaus, J. Haetge, S. Nowak, F. M. Schappacher, and M. Winter, "Correlation of aging and thermal stability of commercial 18650-type lithium ion batteries," *Journal of Power Sources*, vol. 342, pp. 382–392, Feb. 2017.

[55] M. S. Wu, P. Chiang, J. C. Lin, and Y.-S. Jan, "Correlation between electrochemical characteristics and thermal stability of advanced lithium-ion batteries in abuse tests—short-circuit tests," *Electrochimica Acta*, 2004.

[56] E. P. Roth and D. H. Doughty, "Thermal abuse performance of high-power 18650 Li-ion cells," *Journal of Power Sources*, vol. 128, pp. 308–318, Apr. 2004.

[57] P. Röder, B. Stiaszny, J. C. Ziegler, and N. Baba, "The impact of calendar aging on the thermal stability of a LiMn2O4 – Li(Ni1/3Mn1/3Co1/3)O2 / graphite lithium-ion cell," *Journal of Power Sources*, vol. 268, pp. 315–325, 2014.

[58] N. N. Sinha and N. Munichandraiah, "The effect of particle size on performance of cathode materials of Li-ion batteries," *Journal of the Indian Institute of Science*, vol. 89, no. 4, pp. 381–392, 2009.

[59] M. Jo, Y.-S. Hong, J. Choo, and J. Cho, "Effect of LiCoO2 Cathode Nanoparticle Size on High Rate Performance for Li-Ion Batteries," *Journal of The Electrochemical Society*, vol. 156, no. 6, pp. A430–5, 2009.

[60] M. Jo, S. Jeong, and J. Cho, "High power LiCoO2 cathode materials with ultra energy density for Li-ion cells," *Electrochemistry Communications*, vol. 12, pp. 992–995, July 2010.

[61] Y.-S. Park and S.-M. Lee, "Effects of particle size on the thermal stability of lithiated graphite anode," *Electrochimica Acta*, vol. 54, pp. 3339–3343, Apr. 2009.

[62] J. Jiang and J. R. Dahn, "Effects of particle size and electrolyte salt on the thermal stability of Li0.5CoO2," *Electrochimica Acta*, vol. 49, pp. 2661–2666, July 2004.

[63] H. Yu, H. Kim, Y. Wang, P. He, and D. Asakura, "High-energy 'composite'layered manganese-rich cathode materials via controlling Li2MnO3 phase activation for lithium-ion batteries," *Physical Chemistry Chemical Physics*, vol. 14, pp. 6584–6595, 2012.

[64] A. Ito, Y. Sato, T. Sanada, M. Hatano, H. Horie, and Y. Ohsawa, "In situ X-ray absorption spectroscopic study of Li-rich layered cathode material Li[Ni0.17Li0.2Co0.07Mn0.56]O2," *Journal of Power Sources*, vol. 196, pp. 6828–6834, Aug. 2011.

[65] C. Delmas, "Battery materials: Operating through oxygen," *Nature Chemistry*, vol. 8, pp. 641–643, July 2016.

[66] H. Koga, L. Croguennec, P. Mannessiez, M. Menetrier, F. Weill, L. Bourgeois, M. Duttine, E. Suard, and C. Delmas, "Li1.20Mn0.54Co0.13Ni0.13O2 with Different Particle Sizes as Attractive Positive Electrode Materials for Lithium-Ion Batteries: Insights into Their Structure," *The Journal of Physical Chemistry C*, vol. 116, pp. 13497–13506, June 2012.

[67] J. Geder, H. E. Hoster, A. Jossen, J. Garche, and D. Y. W. Yu, "Impact of active material surface area on thermal stability of LiCoO2 cathode," *Journal of Power Sources*, vol. 257, pp. 286–292, July 2014.

[68] P. Lanz, H. Sommer, M. Schulz-Dobrick, and P. Novák, "Oxygen release from high-energy xLi2MnO3 · (1−x)LiMO2 (M=Mn, Ni, Co): Electrochemical, differential electrochemical mass spectrometric, in situ pressure, and in situ temperature characterization," *Electrochimica Acta*, vol. 93, pp. 114–119, Mar. 2013.

[69] H. Koga, L. Croguennec, M. Menetrier, P. Mannessiez, F. Weill, and C. Delmas, "Different oxygen redox participation for bulk and surface: A possible global explanation for the cycling mechanism of Li1.20Mn0.54Co0.13Ni0.13O2," *Journal of Power Sources*, vol. 236, pp. 250–258, Aug. 2013.

[70] H. Koga, L. Croguennec, M. Menetrier, K. Douhil, S. Belin, L. Bourgeois, L. Bourgeois, E. Suard, F. Weill, and C. Delmas, "Reversible Oxygen Participation to the Redox Processes Revealed for Li1.20Mn0.54Co0.13Ni0.13O2," *Journal of The Electrochemical Society*, vol. 160, pp. A786–A792, Mar. 2013.

[71] D. Tang, D. Liu, Y. Liu, Z. Yang, and L. Chen, "Investigation on the electrochemical activation process of Li1.20Ni0.32Co0.004Mn0.476O2," *Progress in Natural Science: Materials International*, vol. 24, pp. 388–396, Aug. 2014.

[72] J. Geder, J. H. Song, S.-H. Kang, and D. Y. W. Yu, "Thermal stability of lithium-rich manganese-based cathode," *Solid State Ionics*, vol. 268, pp. 242–246, Dec. 2014.

[73] S.-H. Wu, H.-C. Chou, R.-N. Pan, Y.-H. Huang, J.-J. Horng, J.-H. Chi, and C.-M. Shu, "Thermal hazard analyses of organic peroxides and inorganic peroxides by calorimetric approaches," *Journal of Thermal Analysis and Calorimetry*, vol. 109, pp. 355–364, June 2011.

[74] J. Choi and a. Manthiram, "Investigation of the Irreversible Capacity Loss in the Layered LiNi1/3Mn1/3Co1/3O2 Cathodes," *Electrochemical and Solid-State Letters*, vol. 8, no. 8, pp. C102–C105, 2005.

[75] K. Nakamura, H. Hirano, D. Nishioka, Y. Michihiro, and T. Moriga, "Lithium ionic diffusion in lithium cobalt oxides prepared by mechanical milling," *Solid State Ionics*, vol. 179, pp. 1806–1809, Sept. 2008.

[76] Y. Zhang and C.-Y. Wang, "Cycle-Life Characterization of Automotive Lithium-Ion Batteries with LiNiO2 Cathode," *Journal of The Electrochemical Society*, vol. 156, pp. A527–A535, July 2009.

[77] J. C. Lagrasias, J. A. Reeds, M. H. Wright, and P. E. Wright, "Convergence properties of the Nedler-Mead Simplex method in low dimensions," *SIAM Journal on Optimization*, vol. 9, pp. 112–147, Dec. 1998.

[78] Y. Reynier, J. Graetz, T. Swan-Wood, P. Rez, and R. Yazami, "Entropy of Li intercalation in LixCoO2," *Physical Review B*, vol. 70, p. 174304, 2004.

[79] J. Geder, R. Arunachala, S. Jairam, and A. Jossen, "Thermal behavior of aged lithium-ion batteries: calorimetric observations," *2015 IEEE Green Energy and Systems Conference (IGESC)*, pp. 24–29, 2015.

[80] M. E. Brown, *Introduction to Thermal Analysis.* Techniques and Applications, Springer Science & Business Media, Dec. 2001.

[81] T. Ozawa, "Thermal analysis—review and prospect," *Thermochimica Acta*, vol. 355, pp. 35–42, 2000.

[82] T. Ozawa, "A new method of analyzing thermogravimetric data," *Bulletin of the chemical society of Japan*, vol. 38, pp. 1881–1886, 1965.

[83] H. L. Friedman, "Kinetics of thermal degradation of char-forming plastics from thermogravimetry. Application to a phenolic plastic," *Journal of Polymer Science: Polymer Symposia*, vol. 6, pp. 183–195, 1964.

[84] S. Vyazovkin, "A unified approach to kinetic processing of nonisothermal data," *International Journal of Chemical Kinetics*, vol. 28, pp. 95–101, 1996.

[85] Z. B. Alfassi, "On the normalization of a mass spectrum for comparison of two spectra," *Journal of the American Society for Mass Spectrometry*, vol. 15, pp. 385–387, Mar. 2004.

[86] G. T. Rasmussen and T. L. Isenhour, "The Evaluation of Mass Spectral Search Algorithms," *Journal of Chemical Information and Modeling*, vol. 19, pp. 179–186, Aug. 1979.

[87] V. V. Viswanathan, D. Choi, D. Wang, W. Xu, S. Towne, R. E. Williford, J.-G. Zhang, J. Liu, and Z. Yang, "Effect of entropy change of lithium intercalation in cathodes and anodes on Li-ion battery thermal management," *Journal of Power Sources*, vol. 195, pp. 3720–3729, June 2010.

[88] G. Höhne, W. Hemminger, and H. J. Flammersheim, *Differential Scanning Calorimetry. An introduction for practitioners*, Springer Science & Business Media, 2013.

[89] H. Yang, H. Bang, K. Amine, and J. Prakash, "Investigations of the Exothermic Reactions of Natural Graphite Anode for Li-Ion Batteries during Thermal Runaway," *Journal of The Electrochemical Society*, vol. 152, no. 1, pp. A73–A79, 2005.

[90] Z. Zhang, D. Fouchard, and J. R. Rea, "Differential scanning calorimetry material studies: implications for the safety of lithium-ion cells," *Journal of Power Sources*, vol. 70, pp. 16–20, 1998.

[91] A. M. Andersson and K. Edström, "Chemical Composition and Morphology of the Elevated Temperature SEI on Graphite," *Journal of The Electrochemical Society*, vol. 148, no. 10, pp. A1100–10, 2001.

[92] J. Yamaki, H. Takatsuji, T. Kawamura, and M. Egashira, "Thermal stability of graphite anode with electrolyte in lithium-ion cells," *Solid State Ionics*, vol. 148, pp. 241–245, 2002.

[93] T. Inoue and K. Mukai, "Roles of positive or negative electrodes in the thermal runaway of lithium-ion batteries: Accelerating rate calorimetry analyses with an all-inclusive microcell," *Electrochemistry Communications*, vol. 77, pp. 28–31, Apr. 2017.

[94] D. Doughty and E. P. Roth, "A General Discussion of Li Ion Battery Safety," *The Electrochemical Society Interface*, pp. 37–44, Aug. 2012.

[95] Z. Wu, L. Cao, J. Hartig, and S. Santhanagopalan, "Effect of Aging on Mechanical Properties of Lithium Ion Cell Components," *ECS Transactions*, vol. 77, pp. 199–208, Aug. 2017.

[96] J. Fu, Y. Bai, C. Liu, H. Yu, and Y. Mo, "Physical characteristic study of LiCoO2 prepared by molten salt synthesis method in 550–800°C," *Materials Chemistry and Physics*, vol. 115, pp. 105–109, May 2009.

[97] H. Porthault, R. Baddour-Hadjean, F. Le Cras, C. Bourbon, and S. Franger, "Raman study of the spinel-to-layered phase transformation in sol–gel LiCoO2 cathode powders as a function of the post-annealing temperature," *Vibrational Spectroscopy*, vol. 62, pp. 152–158, Sept. 2012.

[98] W. Zhang, "Influence of Surface Area on Thermal Stability of Cathode in Lithium-ion Battery," Master's thesis, München, 2013.

[99] M. Antaya, K. Cearns, and J. S. Preston, "In situ growth of layered, spinel, and rock-salt LiCoO2 by laser ablation deposition," *Journal of Applied Physics*, vol. 76, no. 5, pp. 2779–2806, 1994.

[100] M. N. Obrovac, O. Mao, and J. R. Dahn, "Structure and electrochemistry of LiMO2 (M= Ti, Mn, Fe, Co, Ni) prepared by mechanochemical synthesis," *Solid State Ionics*, vol. 112, pp. 9–19, 1998.

[101] L. Wang, T. Maxisch, and G. Ceder, "A First-Principles Approach to Studying the Thermal Stability of Oxide Cathode Materials," *Chemistry of Materials*, vol. 19, pp. 543–552, Feb. 2007.

[102] W. D. Johnston, R. R. Heikes, and D. Sestrich, "The Preparation, Crystallography, and Magnetic Properties of the Li-Co-O System," *Journal of Physics and Chemistry of Solids*, vol. 7, pp. 1–13, 1958.

[103] N. Yabuuchi, K. Yoshii, S.-T. Myung, I. Nakai, and S. Komaba, "Detailed studies of a high-capacity electrode material for rechargeable batteries, Li2MnO3-LiCo1/3Ni1/3Mn1/3O2," *Journal of the American Chemical Society*, vol. 133, pp. 4404–4419, Mar. 2011.

[104] V. Baron, J. Gutzmer, H. Rundlöf, and R. Tellgren, "The influence of iron substitution on the magnetic properties of hausmannite, Mn2+ (Fe,Mn)2 3+ O4," *American Mineralogist*, vol. 83, pp. 786–793, 1998.

[105] J. Haines, J. M. Léger, and S. Hoyau, "Second-order rutile-type to CaCl2-type phase transition in β-MnO2 at high pressure," *Journal of Physics and Chemistry of Solids*, vol. 56, pp. 965–973, July 1995.

[106] J.-H. Park, J.-H. Cho, S.-B. Kim, W.-S. Kim, S.-Y. Lee, and S.-Y. Lee, "A novel ion-conductive protection skin based on polyimide gel polymer electrolyte: application to nanoscale coating layer of high voltage LiNi1/3Co1/3Mn1/3O2 cathode materials for lithium-ion batteries," *Journal of Materials Chemistry*, vol. 22, no. 25, pp. 12574–8, 2012.

[107] J.-H. Park, J.-M. Kim, J.-S. Kim, E.-G. Shim, and S.-Y. Lee, "Polyimide/carbon black composite nanocoating layers as a facile surface modification strategy for high-voltage lithium ion cathode materials," *Journal of Materials Chemistry A*, vol. 1, no. 40, pp. 12441–8, 2013.

[108] J.-H. Park, J.-M. Kim, C. K. Lee, and S.-Y. Lee, "Mixed ion/electron-conductive protective soft nanomatter-based conformal surface modification of lithium-ion battery cathode materials," *Journal of Power Sources*, vol. 263, pp. 209–216, Oct. 2014.

[109] D.-H. Seo, J. Lee, A. Urban, R. Malik, S. Kang, and G. Ceder, "The structural and chemical origin of the oxygen redox activity in layered and cation-disordered Li-excess cathode materials," *Nature Chemistry*, vol. 8, pp. 692 –697, May 2016.

[110] K. Luo, M. R. Roberts, R. Hao, N. Guerrini, D. M. Pickup, Y.-S. Liu, K. Edström, J. Guo, A. V. Chadwick, L. C. Duda, and P. G. Bruce, "Charge-compensation in 3d-transition-metal-oxide intercalation cathodes through the generation of localized electron holes on oxygen," *Nature Chemistry*, vol. 8, pp. 684 –691, Mar. 2016.

[111] M. N. Richard and J. R. Dahn, "Accelerating Rate Calorimetry Study on the Thermal Stability of Lithium Intercalated Graphite in Electrolyte. II. Modeling the Results and Predicting Differential Scanning Calorimeter Curves," *Journal of The Electrochemical Society*, vol. 146, pp. 2078–2084, June 1999.

[112] D. D. MacNeil, L. Christensen, J. Landucci, J. M. Paulsen, and J. R. Dahn, "An Autocatalytic Mechanism for the Reaction of LixCoO2 in Electrolyte at Elevated Temperature," *Journal of The Electrochemical Society*, vol. 147, no. 3, pp. 970–11, 2000.

[113] R. Ashino, M. Nagase, and R. Vaillancourt, "Behind and beyond the MATLAB ODE suite," *Computers & Mathematics with Applications*, vol. 40, pp. 491–512, 2000.

[114] M. Gahleitner and C. Paulik, "Polypropylene," in *Ullmanns Encyclopedia of Industrial Chemistry*, pp. 1–44, Weinheim, Germany: VCH, Mar. 2014.

[115] X. Feng, S. Zheng, D. Ren, X. He, L. Wang, X. Liu, M. Li, and M. Ouyang, "Key Characteristics for Thermal Runaway of Li-ion Batteries," *Energy Procedia*, vol. 158, pp. 4684–4689, Feb. 2019.

[116] N. Tanaka and W. G. Bessler, "Numerical investigation of kinetic mechanism for runaway thermo-electrochemistry in lithium-ion cells," *Solid State Ionics*, vol. 262, pp. 70–73, Sept. 2014.

[117] X. Liu, D. Ren, H. Hsu, X. Feng, G.-L. Xu, M. Zhuang, H. Gao, L. Lu, X. Han, Z. Chu, J. Li, X. He, K. Amine, and M. Ouyang, "Thermal Runaway of Lithium-Ion Batteries without Internal Short Circuit," *Joule*, vol. 2, pp. 2047–2064, Oct. 2018.

[118] Y.-K. Sun, S.-T. Myung, B.-C. Park, J. Prakash, I. Belharouak, and K. Amine, "High-energy cathode material for long-life and safe lithium batteries," *Nature Materials*, vol. 8, pp. 320–324, Mar. 2009.

[119] M. Azevedo, N. Campagnol, T. Hagenbruch, K. Hoffman, A. Lala, and O. Ramsbottom, "Lithium and cobalt – a tale of two commodities," tech. rep., June 2018.

[120] B. Rieger, S. Schlueter, S. V. Erhard, J. Schmalz, G. Reinhart, and A. Jossen, "Multi-scale investigation of thickness changes in a commercial pouch type lithium-ion battery," *Journal of Energy Storage*, vol. 6, pp. 213–221, May 2016.

Appendices

A.1 SEM images of electrodes from new and aged 18650 cells

A.1.1 Anode

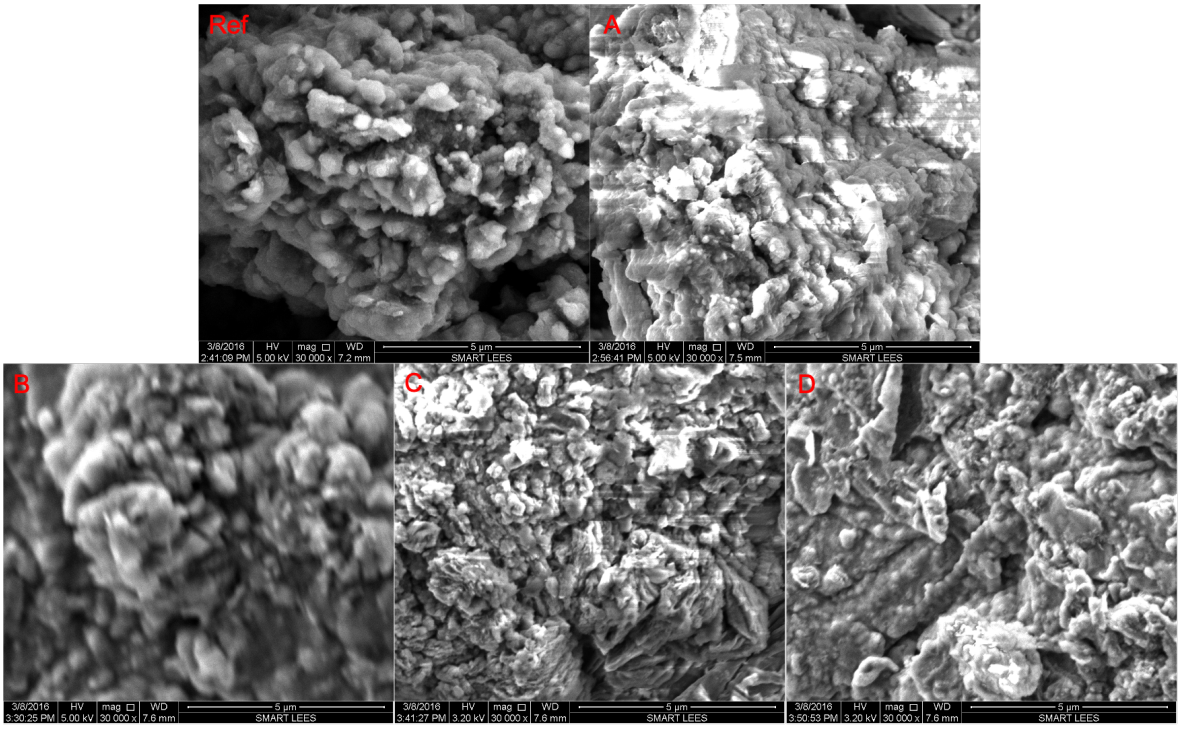

A.1.2 Cathode

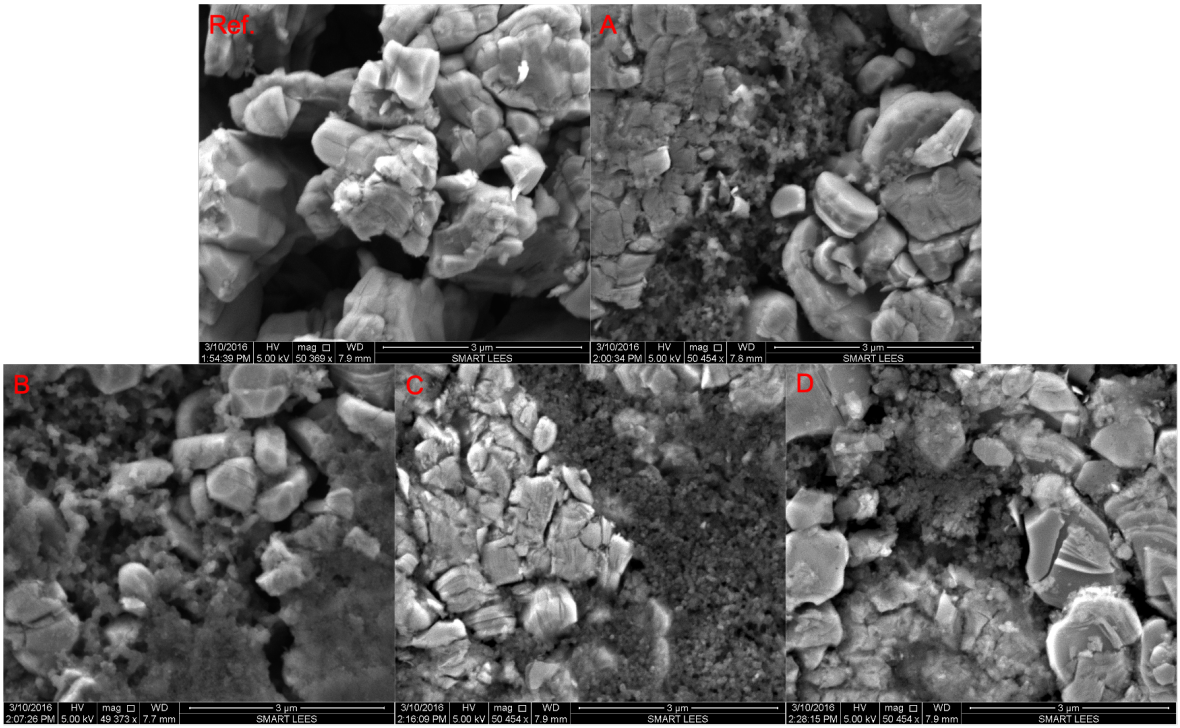

A.2 XRD of decomposed NCM cathodes from new and aged 18650 cells

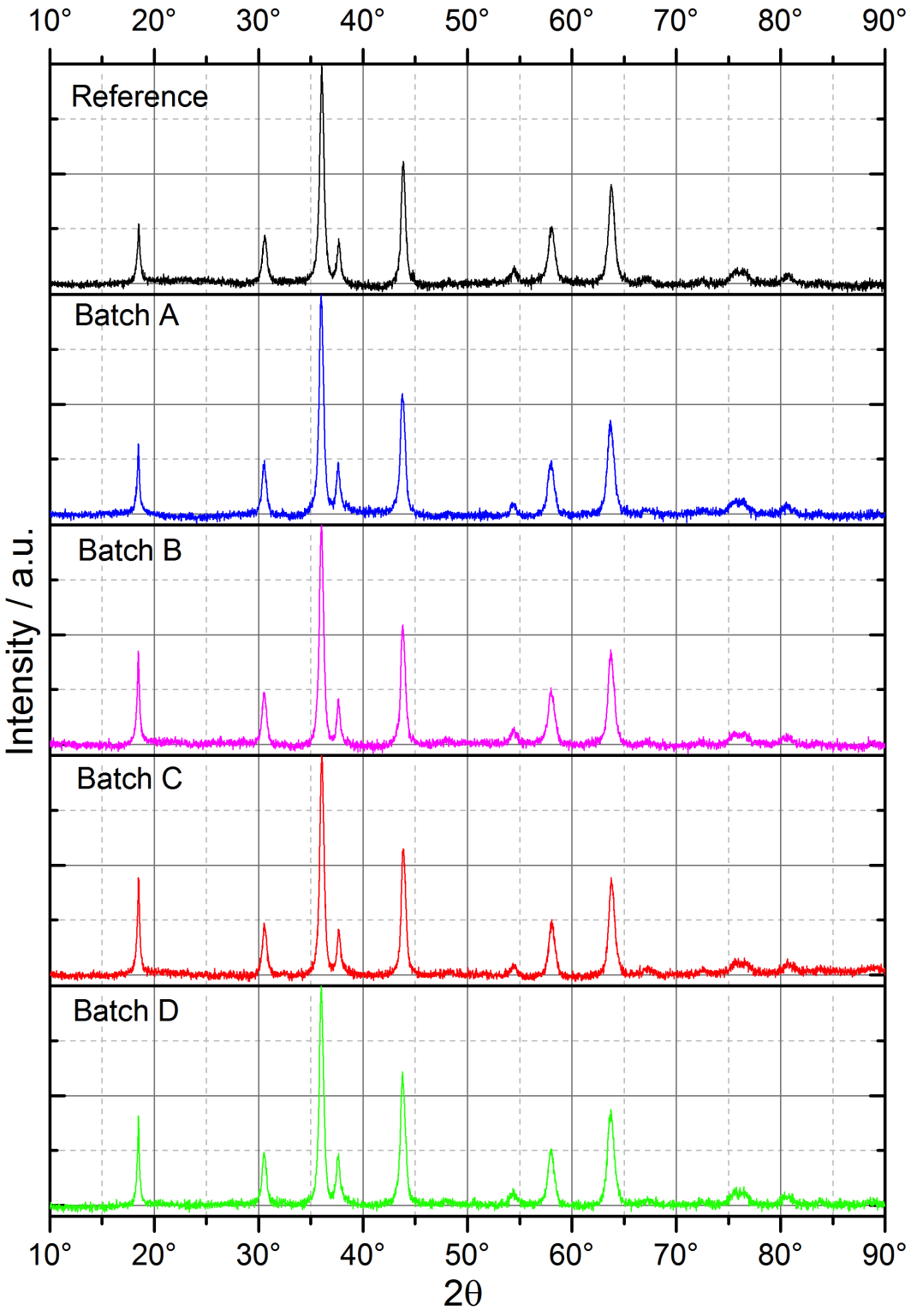

A.3 MatLab model

A.3.1 Main script

```
clear
clc

%Battery composition

m_Batt=                        42.38; %g

w_Cath=                  0.377;
w_An=                    0.275;
w_Sep=                   0.042;
w_oth=                   0.306;

m_Cath = w_Cath*m_Batt;
m_An = w_An*m_Batt;
m_Sep = w_Sep*m_Batt;
m_oth = w_oth*m_Batt;

% heat capacity (C)    J/K

C_h=37;                  %sample holder
C_batt=37.5;             %battery
C_tot=C_batt+C_h;        %total

% Initial conditions

T0=388.15;         %K  Onset temperature

x_An=0.0001;        %Initial extent of reaction: Anode
x_Cath=0.0001;      %Initial extent of reaction: Cathode

t0= 0;

%Parameters: Enthalpy h [J/g]; Activation Energy Ea [kJ/mol]; Frequency factor k [1/min]

h_An=      300;
h_Cath=    410;
```

```
Ea_An=     80;
Ea_Cath=   144;

k_An=      3E7;
k_Cath=    8.33E14;

%Summarized parameters and initial values

R=8.314E-3;      %kJ/mol-1/K-1       Gas constant

Pk1=-Ea_An/R;
Pk2=-Ea_Cath/R;

Pt1=h_An*m_An/C_tot;
Pt2=h_Cath*m_Cath/C_tot;

V1=[t0 x_An x_Cath T0];

%Calculations (see equations file)

[Time,results]=ode45(@(t,V) eqn_cell(t,V,k_An,k_Cath,Pk1,Pk2,Pt1,Pt2),[0 5000],V1);

%Derivation dT/dt

i = 1;

while(i <= length(results(:,2)))
heat1(i) = Pt1*k_An*exp(Pk1/results(i,4))*(1-(results(i,2)));

if heat1(i)<= 0;
heat1(i)=0;
end
i = i + 1;

end

j = 1;

while(j <= length(results(:,3)))
```

```
heat2(j) = Pt2*k_Cath*exp(Pk2/results(j,4))*(1-(results(j,3)))*(0.1+(results(j,3))^0.5);

if heat2(j)<= 0;
heat2(j)=0;
end
if results(j,4)<= 423.15;
heat2(j)=0;
end
j = j + 1;

end

heat = heat1+heat2;
```

A.3.2 Differential functions

```
function x = eqn_cell(t,V,k_An,k_Cath,Pk1,Pk2,Pt1,Pt2)

x=zeros(4,numel(t));

x(1)=1;

x(2) = k_An*exp(Pk1/V(4))*(1-(V(2)));          %Conversion Anode
if V(2) >= 1;
x(2) = 0;
end

x(3) = k_Cath*exp(Pk2/V(4))*(1-(V(3)))*(0.1+(V(3))^0.5);        %Conversion Cathode
if V(3) >= 1;
x(3) = 0;
end
if V(4) <= 423.15;
x(3) = 0;
end

x(4) =  Pt1*x(2)+Pt2*x(3);

disp(['time = ', num2str(t)])
end
```